



# Fabrication and Physics of CdTe Devices by Sputtering

**Final Report**  
**1 March 2005 – 30 November 2008**

A. Compaan, R. Collins, V. Karpov, and  
D. Giolando  
*University of Toledo*  
*Toledo, Ohio*

**Subcontract Report**  
**NREL/SR-520-45398**  
**April 2009**

NREL is operated for DOE by the Alliance for Sustainable Energy, LLC

Contract No. DE-AC36-08-GO28308



# Fabrication and Physics of CdTe Devices by Sputtering

**Final Report**  
**1 March 2005 – 30 November 2008**

A. Compaan, R. Collins, V. Karpov, and  
D. Giolando

*University of Toledo*  
*Toledo, Ohio*

NREL Technical Monitor: Bolko von Roedern

Prepared under Subcontract No(s). ZXL-5-44205-01

*Subcontract Report*

**NREL/SR-520-45398**

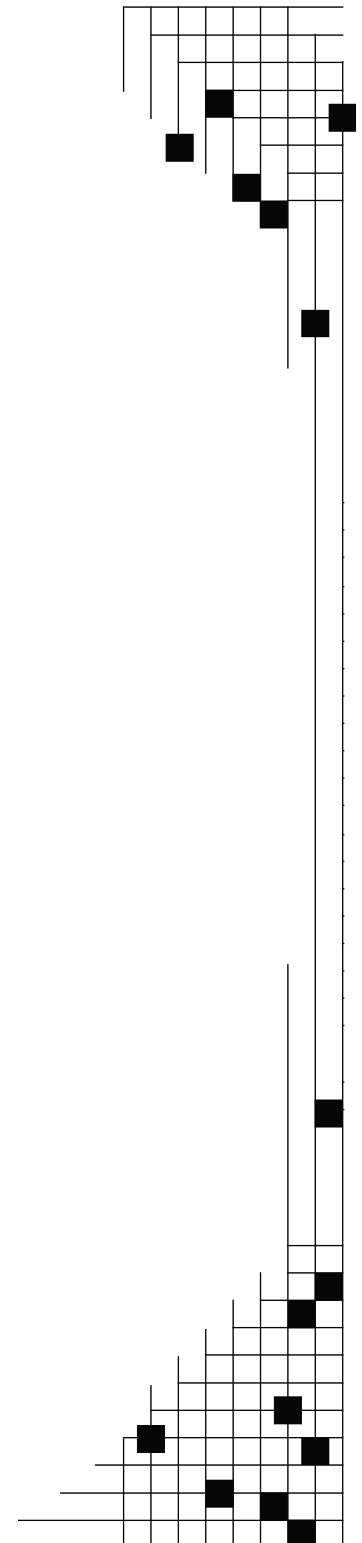
**April 2009**

## **National Renewable Energy Laboratory**

**1617 Cole Boulevard, Golden, Colorado 80401-3393**  
**303-275-3000 • [www.nrel.gov](http://www.nrel.gov)**

NREL is a national laboratory of the U.S. Department of Energy  
Office of Energy Efficiency and Renewable Energy  
Operated by the Alliance for Sustainable Energy, LLC

Contract No. DE-AC36-08-GO28308



**This publication was reproduced from the best available copy  
Submitted by the subcontractor and received no editorial review at NREL**

### **NOTICE**

This report was prepared as an account of work sponsored by an agency of the United States government. Neither the United States government nor any agency thereof, nor any of their employees, makes any warranty, express or implied, or assumes any legal liability or responsibility for the accuracy, completeness, or usefulness of any information, apparatus, product, or process disclosed, or represents that its use would not infringe privately owned rights. Reference herein to any specific commercial product, process, or service by trade name, trademark, manufacturer, or otherwise does not necessarily constitute or imply its endorsement, recommendation, or favoring by the United States government or any agency thereof. The views and opinions of authors expressed herein do not necessarily state or reflect those of the United States government or any agency thereof.

Available electronically at <http://www.osti.gov/bridge>

Available for a processing fee to U.S. Department of Energy  
and its contractors, in paper, from:

U.S. Department of Energy  
Office of Scientific and Technical Information  
P.O. Box 62  
Oak Ridge, TN 37831-0062  
phone: 865.576.8401  
fax: 865.576.5728  
email: <mailto:reports@adonis.osti.gov>

Available for sale to the public, in paper, from:

U.S. Department of Commerce  
National Technical Information Service  
5285 Port Royal Road  
Springfield, VA 22161  
phone: 800.553.6847  
fax: 703.605.6900  
email: [orders@ntis.fedworld.gov](mailto:orders@ntis.fedworld.gov)  
online ordering: <http://www.ntis.gov/ordering.htm>



Printed on paper containing at least 50% wastepaper, including 20% postconsumer waste

## Table of Contents

<b>Table of Contents</b> .....	iii
<b>List of Figures</b> .....	v
<b>List of Tables</b> .....	vii
<b>1. Introduction and Executive Summary</b> .....	1
<b>2. Ex Situ Spectroscopic Ellipsometry</b> .....	4
2.1 Etch back studies of CdTe materials and solar cells .....	5
2.1.1 Verification of the etching procedure .....	5
2.1.2 Etch back studies of CdTe materials .....	6
2.1.3 Etch back studies of CdTe solar cells .....	7
2.2 Ex situ SE measurements of CdTe solar cells .....	8
2.2.1 TEC-15 optical properties .....	8
2.2.2 Optical modeling of etch-smoothened CdTe solar cells .....	9
2.2.3 Through-the-glass measurements of the CdTe solar cell .....	10
2.3 Future directions .....	12
<b>3. Real Time Spectroscopic Ellipsometry: Dielectric Functions and Structural Evolution</b> .....	14
3.1 Overview of CdTe and CdS dielectric functions .....	15
3.2 CdTe and CdS structural evolution on Si substrates as measured by RTSE .....	16
3.2.1 Role of substrate temperature for CdTe and CdS .....	16
3.2.2 Role of Ar pressure for CdTe .....	19
3.3 Future directions .....	20
<b>4. In-depth Analysis of the Dielectric Functions of CdTe and CdS</b> .....	22
4.1 Analysis methodology .....	23
4.2 Critical point broadening parameters and grain structure .....	24
4.3 Critical Point Energies and Strain .....	25
4.4 Summary: Effects of temperature, grain size, and stress on the critical points of CdTe and CdS .....	27
4.5 Ternary alloys between CdS and CdTe .....	28
4.5.1 Dielectric functions of ternary alloys .....	28
4.5.2 Analysis of alloy formation at CdS/CdTe and CdTe/CdS interfaces .....	29
4.6 Future directions .....	29
<b>5. HREM, EXAFS and XES Studies of CdTe cells</b> .....	31
5.1 Introduction .....	31
5.2 Sample Preparation .....	31
5.3 Voids in CdTe and CdTe/CdS Interface .....	32
5.4 Cu Distribution and Local Structure in CdTe cells .....	33
5.4.1 EDS mapping .....	33
5.4.2 X-ray Fluorescence .....	33
5.4.3 High Resolution TEM and Fine-probe EDS .....	34
5.4.4 EXAFS .....	36
5.5 S at CdTe Back Contact .....	37
5.6 Conclusions .....	38

<b>6. Potential Distribution During Magnetron Sputtering Deposition</b>	39
6.1 Introduction	39
6.2 Cathode DC Bias	40
6.3 Substrate Self-Bias	40
6.4 Plasma Potential	41
6.5 Conclusions	41
<b>7. Ultra Thin Devices</b>	43
7.1 Presence of an HRT layer	43
7.2 CdS thickness	43
7.3 CdTe thickness	43
7.4 CdCl <sub>2</sub> treatment	43
7.5 Thickness of the as-deposited Cu layer	47
7.6 Cu diffusion time	48
7.7 Cell performance statistics for optimized cells	48
7.8 Conclusions	55
<b>8. Shunt Passivation - Electrochemical Polymerization Treatment of CdTe Solar Cell Devices</b>	56
8.1 Introduction	56
8.2 Characterizing the new insulating thin film (conducting polymer)	56
8.3 Effect of electrochemical treatment on copper diffusion	59
<b>9. A theory of Admittance Spectroscopy for Thin Films Photovoltaics</b>	62
9.1 Introduction	62
9.2 Theory	63
9.3 Practical Implications	64
9.4 Conclusions	65
<b>10. References (from section 1 through 9)</b>	66
<b>11. Publications</b>	67
11.1 Refereed papers published or in press	67
11.2 Poster or Oral Presentations	69
11.3 Publications and presentations at DOE Program Reviews	70
<b>12. Project Personnel</b>	71
12.1 Postdoctoral Associates / Research Assistant Professors	71
12.2 Graduate Students (with Principal Advisor)	71
12.3 Undergraduate Students	71
12.4 Technical Assistants	71

## List of Figures

Figure 2.1	The void volume fraction of CdTe during a low temperature deposition (130°C). ...	5
Figure 2.2	$E_1$ (upper panel) and width $\Gamma_{E1}$ (lower panel) of CdTe bulk layer. ....	6
Figure 2.3	$E_1$ transition of CdTe bulk layer for a sputtered CdTe solar cell. ....	7
Figure 2.4	Broadening parameter $\Gamma_{E1}$ of CdTe bulk layer for a sputtered CdTe solar cell .....	7
Figure 2.5	Dielectric function of TEC-15 glass.....	8
Figure 2.6	Dielectric functions of SnO <sub>2</sub> :F.....	9
Figure 2.7	Structural model for the CdTe solar cell after the 15th Br <sub>2</sub> +methanol etch. ....	9
Figure 2.8	Ex situ SE spectra in ( $\psi, \Delta$ ) from the CdTe surface and from the prism/glass side..	10
Figure 2.9	The structural parameters deduced from fig 2.8.....	11
Figure 2.10	CdS and CdTe/CdS interface layer thicknesses deduced from fig 2.8.....	11
Figure 2.11	Ellipsometric spectra for a CdTe solar cell obtained after CdCl <sub>2</sub> treatment. ....	12
Figure 3.1	Complex dielectric functions $\epsilon$ of typical polycrystalline CdTe and CdS films. ....	15
Figure 3.2	Surface roughness thickness ( $d_s$ ) for CdTe films on c-Si wafer at different $T_d$ . ....	16
Figure 3.3	$d_s$ vs. $d_b$ evolution for CdS films sputtered on c-Si wafer at different $T_d$ .....	16
Figure 3.4	Void volume fraction ( $f_v$ ) for CdTe films sputtered on c-Si wafer held at different $T_d$ . ....	17
Figure 3.5	$f_v$ evolutions for CdS films sputtered on c-Si wafer held at different $T_d$ . ....	18
Figure 3.6	Effective rate of material growth (excluding voids) as a function of $T_d$ .....	18
Figure 3.7	Surface roughness evolution for CdTe sputtering with different Ar pressures .....	19
Figure 3.8	Stepwise void evolution for the CdTe films of Fig. 3.7. ....	19
Figure 3.9	Effective CdTe growth rate for the films of Fig. 3.7.....	20
Figure 4.1	The 2nd derivative spectra of dielectric functions $\epsilon$ of polycrystalline CdTe and CdS.....	23
Figure 4.2	The broadening parameters for the $E_0$ , $E_1$ -A, and $E_1$ -B CP <sub>s</sub> for CdS films deposited at different temperatures.....	24
Figure 4.3	Grain size for the CdS films of Fig. 3.3. ....	24
Figure 4.4	The CdS $E_1$ -A and $E_1$ -B broadening parameters plotted vs. the reciprocal of grain radius in Fig. 20. ....	25
Figure 4.5	The 2nd derivative spectra of room temperature $\epsilon$ for c-CdTe and the CdTe films	26
Figure 4.6	15°C $E_0$ CP energies for CdTe films sputtered at different $T_d$ . ....	27
Figure 4.7	Dielectric functions of co-sputtered CdS <sub>x</sub> Te <sub>1-x</sub> alloy films at 190°C.....	28
Figure 4.8	Composition profiles $x(d_b)$ in CdS <sub>x</sub> Te <sub>1-x</sub> .....	29
Figure 5.1	Cross-sectional HAADF and STEM-BF images of standard CdTe device. ....	32
Figure 5.2	HAADF image and EDS mapping of Cd, Te, S, Cu and Au on the same area.....	33
Figure 5.3	The schematic structures of the samples and X-ray fluorescence spectra.....	34
Figure 5.4	High resolution TEM image at the CdTe/Au interface. ....	35
Figure 5.5	Phase-uncorrected $\chi(R)$ functions of semi-cell structure sample and theoretical fitting compared with Cu <sub>2</sub> O reference; .....	36
Figure 5.6	Sulfur L <sub>2,3</sub> XES spectra of as-grown CdS reference, as-grown and CdCl <sub>2</sub> treated CdTe/CdS, and a CdSO <sub>4</sub> (sulfate) reference.....	38
Figure 6.1	Experimental setup for potential distribution and the Langmuir probe measurements.....	39
Figure 6.2	Cathode DC bias as a function of pressure and RF power. ....	40
Figure 6.3	Substrate self-bias bias as a function of pressure and RF power. ....	40

Figure 6.4	Plasma potential as a function of pressure and RF power.....	41
Figure 7.1	CdCl <sub>2</sub> treatment temperature profiles for nominal 3 and 30 minute treatments.....	44
Figure 7.2	A schematic representation of “nominal” vs. “actual” treatment time.....	44
Figure 7.3	Arrhenius plots of diffusion coefficients for Cl and Cd in bulk CdTe and Cd diffusion along grain boundaries in CdTe. ....	45
Figure 7.4	Relative contribution of the ramp-up and ramp-down time for a 30-minute treatment at 387 °C.....	45
Figure 7.5	Relative contribution of the ramp-up plus ramp-down time for t a three-minute treatment at 387 °C.....	45
Figure 7.6	CdCl <sub>2</sub> treatment time vs. CdTe thickness and the linear fit for the “corrected” time. .....	46
Figure 7.7	Treatment time chosen for samples of different thickness. ....	47
Figure 7.8	A typical sample used in this study. ....	48
Figure 7.9	A sketch of a sample with individual dot cells.....	50
Figure 7.10	Box-and-whiskers plot of the efficiency of the 10 best cells from each sample ....	50
Figure 7.11	Short-circuit current of the 10 best cells from each sample .....	51
Figure 7.12	Quantum efficiency at zero bias conditions .....	51
Figure 7.13	J-V characteristics of the cells from the Figure 7.11.....	52
Figure 7.14	Open-circuit voltage of the 10 best cells from each sample.....	52
Figure 7.15	Fill factor of the 10 best cells from each sample.....	53
Figure 7.16	Quantum efficiency at variable bias. Thicker cells. ....	54
Figure 7.17	Quantum efficiency at variable bias. Thinner cells. ....	55
Figure 8.1	The base (i.e., neutral) polyaniline .....	56
Figure 8.2	XPS spectrum of a TEC-15 glass substrate used as a control .....	57
Figure 8.3	XPS spectrum of a TEC-15 glass substrate coated with the conducting polymer. ..	58
Figure 8.4	ESI-MS spectra of the newly formed thin film after rinsing.....	59
Figure 8.5	Top surface view of the CdTe solar cell sample.....	60
Figure 8.6	Voc and Jsc of 2 hour copper diffusion of an electrochemically treated and untreated cells. ....	60
Figure 8.7	FF and efficiencies of a 2 hr copper diffusion of an electrochemically treated and untreated cells.....	61
Figure 9.1	Equivalent circuit of a device .....	62
Figure 9.2	Examples of four possible 1D device scenarios. ....	63
Figure 9.3	Prediction of capacitance as a function of frequency for a small 2D substrate cell.....	64

## List of Tables

Table 4.1	Single crystal CP Energies and Widths, Temperature Coefficients of CP Energies and Widths, Electron Group Speeds, and Stress Coefficients of CP Energies for Major CPs for CdTe and CdS.....	27
Table 5.1	Comparison of Cu $K_{\alpha}$ and Mo $K_{\alpha}$ intensities.....	35
Table 5.2	Theoretical fitting parameters of EXAFS spectra of partial cell structure and Cu <sub>2</sub> O reference.....	36
Table 7.1	Benchmarks for CdCl <sub>2</sub> treatment time of different CdTe thickness and corresponding best cell efficiency .....	46
Table 7.2	Sample fabrication details.....	49



## 1. Introduction and Executive Summary

There were three overall emphases in this subcontract: 1) improving our understanding of key aspects of the CdS/CdTe solar cell device physics, 2) improving our understanding of magnetron sputtering and increasing the sputter deposition rate while maintaining high device quality, and 3) reducing the thickness of CdTe layers in the CdS/CdTe cell below 0.5  $\mu\text{m}$  while maintaining voltage and fill factor.

In Phase III of this subcontract, we have completed our characterization of the optical and morphological properties of CdS, CdTe, and the alloy CdSTe films using spectroscopic ellipsometry (Sections 2, 3 and 4). We have performed high resolution energy dispersive x-ray spectroscopy (EDS), x-ray absorption fine structure spectroscopy (XAFS) and x-ray emission spectroscopy (XES) to study the location and chemical bonding of Cu and oxygen in completed CdTe cells (Section 5). We have studied the properties of the sputtering plasma with the goal, *inter alia*, of understanding the origin of and controlling the formation of dust on and in the deposited film (Section 6). A particular emphasis was placed on studies of ultra-thin CdS/CdTe devices with CdTe layers less than 1  $\mu\text{m}$  thick (Section 7). We have developed an electrochemical approach to shunt passivation (Section 8). And finally, we have developed a theory of admittance spectroscopy that is applicable to thin-film PV with resistive electrodes (Section 9).

Highlights of accomplishments during Phase III include:

- A new through-the-glass optical approach has been developed for on-line measurements of CdTe solar modules by spectroscopic ellipsometry (SE). This approach consists of blocking the top surface reflection from the glass and only measuring the beam that is reflected from the TEC-15/solar cell interface. The analysis provides information on the TEC-15 layers, the interface roughness between the CdS and the TEC-15  $\text{SnO}_2\text{:F}$  layers, as well as the thickness of the CdS, the combined roughness-interaction thickness between the CdS and CdTe, and the thickness of the CdTe.
- Real time SE performed on CdTe prepared by magnetron sputtering as a function of Ar pressure demonstrates that the lowest attainable Ar pressure leads to the most dense and uniform films throughout deposition to a 1  $\mu\text{m}$  thickness; increasing Ar pressure from this minimum leads to more rapid void development with film thickness. The surface roughness evolution also depends strongly on the Ar pressure. The lowest Ar pressure leads to a smooth stable surface throughout film growth; increasing Ar pressure leads to much faster roughness development, possibly due to reduced surface diffusion, a mechanism that can lead to smoothening of the surface.
- The critical point (CP) widths and energies in the dielectric functions of CdS and CdTe have been parameterized in terms of key film properties, including temperature, stress, and grain size:

$$\begin{aligned}\Gamma &= \Gamma_b(T_0) + C_{\Gamma} * (T_m - T_0) + (h\nu_g/R) \\ E &= E_b(T_0) + C_{TE} * (T_m - T_0) + C_P P\end{aligned}$$

where  $\Gamma_b$  and  $E_b$  are the width and CP energy of the single crystal;  $T_0$  is a reference measurement temperature, normally room temperature;  $C_{\Gamma}$  and  $C_{TE}$  are the temperature coefficients of the CP width and CP energy, respectively;  $h$  is Planck's constant,  $\nu_g$  is the

excitation group velocity, and  $R$  is the grain size. This parameterization has applications in monitoring and spatially mapping systems that deduce film properties on a solar cell production line.

- Consistency in the analysis of the CdS and CdTe dielectric function CPs in terms of measurement temperature  $T_m$ , grain size  $R$ , and stress  $P$ , has been achieved. The following consistencies are possible: (i) for a given solar cell,  $T_m$  for CdTe and CdS are the same; (ii) for a series of cells of the same component materials (CdTe and CdS) but with different characteristics, the single crystal CP values,  $\Gamma_b$  and  $E_b$ , the CP coefficients,  $C_{TT}$  and  $C_{TE}$ , and the electron group speeds  $v_g$ , are all constants. As a result, this parameterization reflects not only important fundamental information on the electronic structure, but also provides a useful “interlocking” mechanism that can significantly reduce correlation and instrumentation-related drift when determining properties on a production line.
- High-angle annular dark field and STEM bright field images reveal the presence of a modest number of macroscopic voids having typical dimensions of  $\sim 0.15 \mu\text{m}$ , with a void fraction estimated at  $\sim 1\%$ , in the CdTe. This macroscopic void fraction observed by microscopy is less than the overall void fraction of  $\sim 4\%$  revealed in the ellipsometry studies of CdTe films grown on c-Si under similar conditions.
- EDS mapping of TEM cross sections, done in collaboration with the University of Michigan, show that, after back-contact diffusion, the 3.5 nm of Cu used in the back contact mostly remains at the CdTe/Au interface or alloys with the Au layer. Much smaller amounts of Cu appear in the CdTe layer with some higher accumulation in the CdS layer. The higher amount of Cu in the CdS layer compared with CdTe is consistent with SIMS studies of CdS/CdTe cells reported by others. Little evidence was found for Cu accumulation at grain boundaries.
- Synchrotron-based studies (at the Argonne APS) of Cu  $k_\alpha$  x-ray fluorescence and XAFS at the k-absorption edge of Cu indicate that most of the Cu in completed CdS/CdTe cell structures is oxidized in the form of  $\text{Cu}_2\text{O}$ . However, if the structure has not received a prior  $\text{CdCl}_2$  treatment, the Cu is not oxidized. Although the XAFS signal is not spatially selective, the data are consistent with the EDS signal that arises from the CdTe/Au interfacial layer.
- X-ray and ultraviolet photoemission spectroscopy done on completed cells in collaboration with the University of Nevada Las Vegas, show the presence of S at the back contact. Much of this S has been oxidized to the form of  $\text{SO}_4$  in completed cells. This S diffusion and oxidation apparently occurs during the  $\text{CdCl}_2$  treatment.
- Using Langmuir probe studies of the sputter plasma we find that the substrate self-bias potential is depends on the condition of the sputter cathode ground shroud. A bare metal shroud leads to negative substrate self-bias of a few volts, whereas a CdTe-coated shroud yields a positive substrate self-bias of a few volts. This shift in substrate self-bias and corresponding shifts in the plasma potential are correlated with the density of pinhole formation in the deposited film.

- We studied the dependence of dot cell efficiency on CdTe thickness ranging from a maximum of 2.5  $\mu\text{m}$  to a minimum of 0.3  $\mu\text{m}$ . Cell performance was optimized to first order in  $\text{CdCl}_2$  treatment as well as Cu back contact thickness and diffusion time.
- A systematic comparison was made between very thin CdTe cells on standard Pilkington TEC15 glass as well as TEC15 glass with a high resistivity transparent (HRT) coating.
- We have achieved, on HRT-coated TEC15 glass, best cells with efficiencies of
  - 12% @ 0.97  $\mu\text{m}$  of CdTe,
  - 10% @ 0.5  $\mu\text{m}$  of CdTe, and
  - 6% @ 0.3  $\mu\text{m}$  of CdTe.
- We have developed an electrochemical polymerization of a polyaniline-based solution that yields promising results for shunt passivation of thin-film CdTe cells. The characteristics of the polymerized film were determined by XPS and by Electron Spray Ionization Mass Spectroscopy.
- We have developed a theory of admittance spectroscopy that applies to devices with resistive electrodes as is often the case for thin-film PV. (Electrodes need not be equipotentials as is usually assumed.) The model uses the previously introduced concept of a decay length,  $L_0$ , for electric perturbations in the lateral direction and also includes two new decay lengths that describe the spatial dependence for *ac* perturbations of the distributed shunt resistance,  $L_R$ , and capacitance,  $L_C$ .

## 2. Ex Situ Spectroscopic Ellipsometry

This section describes the techniques of ex situ spectroscopic ellipsometry (SE) that have been developed and applied to materials and solar cell devices over the subcontract period. Two measurements methodologies have been developed to study solar cells: reflection from the back, i.e., from the free CdTe surface before back contact formation, and reflection from the front, i.e., through the glass, which is possible at any stage of the processing.

The challenge of back-side measurement is the significant roughness that exists on the free CdTe surface, which can be up to 10% or more of the total thickness. As a result, thick CdTe films ( $> 1 \mu\text{m}$ ) may show only a weak specularly reflected beam with dominant non-specular scattering component. To overcome this problem and to exploit the full power of SE as a sensitive probe of specularly reflecting interfaces, a step-by-step  $\text{Br}_2$ -methanol etching method has been developed for both smoothening and optical depth profiling of the optical structure of CdTe materials and solar cells. In this procedure, a single step consists of immersing the CdTe thin film or device briefly (5 s) in a  $\text{Br}_2$ -methanol solution, cleaning the etched surface in pure methanol, drying it by  $\text{N}_2$  gas, mounting the sample on the ellipsometer stage, and finally measuring it by SE at a single angle of incidence. The use of a multichannel ellipsometer with a measurement time of a few seconds enables multiple steps to be performed in a matter of minutes.

In this section, the validity of the step-by-step etching method has been demonstrated through its application to a CdTe film on a crystalline Si wafer whose void profile was previously determined in a real time SE measurement. The void profiles observed during growth and during the step-by-step etch back process were found to be in good agreement. This result indicates that step-by-step etching can be considered as time-reversed real time SE, whose capability is limited only by the patience of the user in performing the number of etch steps required for suitable depth resolution. The layer thickness removed in each step can be controlled by the concentration of  $\text{Br}_2$  in methanol. The step-by-step etching process has been applied to CdTe thin films on Si wafers before and after different treatments in order to compare the structure of the films. CdTe films subjected to annealing in Ar were compared with those subjected to  $\text{CdCl}_2$  treatment using comparable temperature profiles in both cases. The process has also been applied to  $\text{CdCl}_2$  treated solar cells before back contact formation. The extracted information on the CdTe includes void profiles from the dielectric function amplitudes, strain profiles from the critical point energies, and grain size profiles from the critical point widths. Information on the underlying structure of solar cells has also been obtained with confidence, for example, the thickness and void fraction of the CdS and the thickness and nature of the CdS/CdTe interface -- which are expected to be unchanging as the step-by-step etching proceeds.

The front-side approach is desirable as it can be applied to CdTe modules in any stage of the production process and can be implemented on-line, whereas the disadvantage of the back-side approach is that it is destructive, much more time consuming, and thus not applicable for on-line analysis. The challenge of the front side approach is to minimize controllably or to eliminate the top surface reflection from the glass. In these studies, two methods have been developed for this purpose. In the first method, a  $60^\circ$  prism is contacted to the top glass surface with index matching fluid, and in the second method, the beam from the top surface is spatially isolated and blocked. The first method was exploited most extensively in this research effort whereas the second method was developed in the last phase of the subcontract and is only now being more fully developed. Measurements of the solar cell from the glass-side using a prism coupler, and

from the CdTe side using the step-by-step etch process have been yielded information in good agreement.

Details of these studies are provided in the highlights of the following sub-sections. A significant component of the research on ex situ SE involves developing a database of dielectric functions. Three different sources can be used, depending on the situation. (i) Dielectric functions can be drawn from the literature; (ii) dielectric functions can be deduced from data collected in our laboratory based on in situ real time measurements during film growth; and (iii) dielectric functions can be extracted from data collected in our laboratory based on ex situ measurements. In this section, the dielectric functions of the components of TEC-15 glass are reported as an example of source (iii) above; the section following this one provides examples of the determination of CdS and CdTe dielectric functions from source (ii).

## 2.1 Etch Back Studies of CdTe Materials and Solar Cells

### 2.1.1 Verification of the etching procedure

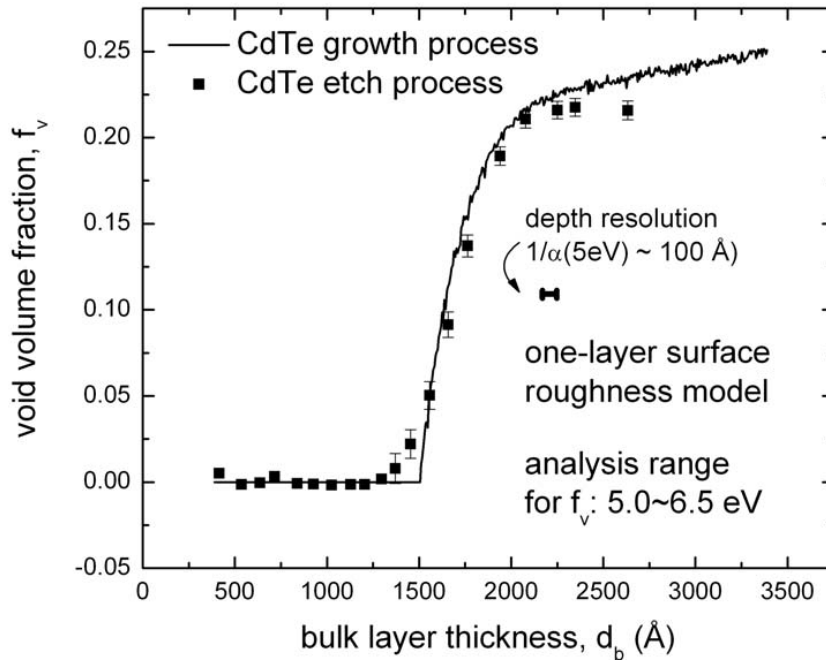


**Figure 2.1** The void volume fraction as a function of CdTe bulk thickness obtained from RTSE data collected during a low temperature deposition process (130°C) on native oxide covered crystalline silicon substrates and during a post-deposition etching process of the same sample. The rf power to the CdTe target was 50 Watt and the Ar pressure was 18 mTorr.

- The discrete points in Figure 2.1 were collected after each Br<sub>2</sub>+methanol etching step, and match deposition results (solid line) very well (within the confidence limits in the analysis). The RTSE results were obtained for a film deposited at low temperature that showed a clear structural transition to high void fraction at a bulk thickness of 1500 Å, believed to be induced by stress. This served as an excellent test sample since the void fraction and structure spanned a wide range.
- This result demonstrates that the etching process is the reverse of the deposition process,

and that etching does not modify the underlying film structure. Thus, a capability of etch-back in conjunction with SE measurements has been demonstrated for post-deposition depth-profiling.

- In the above analysis, the restriction to the high photon energy spectral range (5.0-6.5 eV) implies a higher sensitivity to the surface region of the film. When the surface roughness thickness becomes a significant fraction of the penetration depth, the optical model may be interpreting the minima in the surface profile as bulk material and this may account in part for the high void volume fractions.

### 2.1.2 Etch back studies of CdTe materials

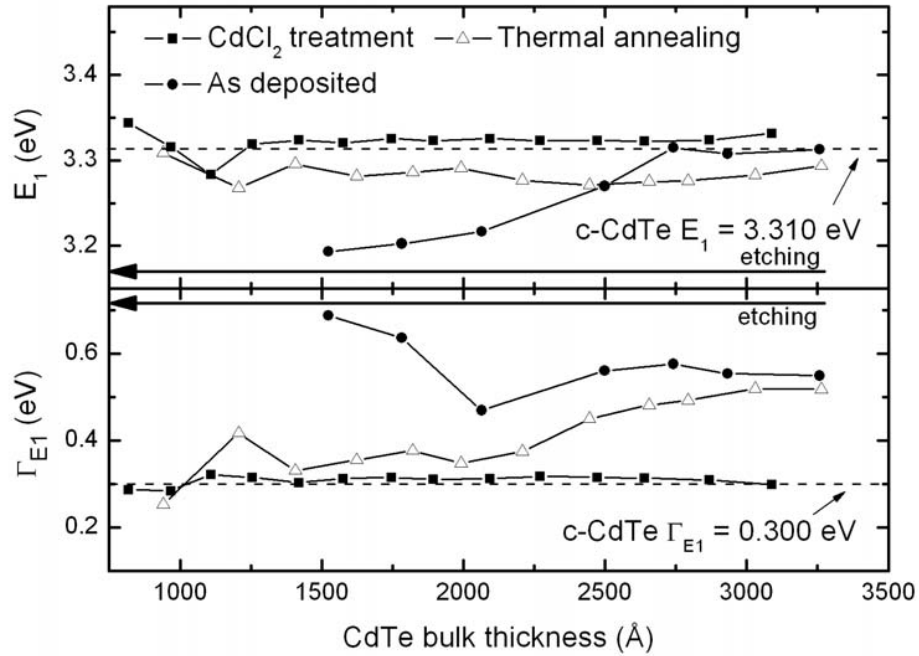


**Figure 2.2** Critical point energy  $E_1$  (upper panel) and width  $\Gamma_{E1}$  (lower panel) as functions of CdTe bulk layer thickness during etching by Br<sub>2</sub>+methanol for CdTe films deposited on crystal Si substrates all deposited under the same conditions (temperature: 188°C, rf power: 60 Watt, and Ar pressure: 18 mTorr) and then processed in three different ways: (i) as-deposited, (ii) annealed at 387°C in Ar for 30 min, and (iii) CdCl<sub>2</sub> treated at 387°C in dry air for 5 min (not including ramp time). The deviations at low thickness are due to the onset of semi-transparency for the  $E_1$  critical point energy.

- For the as-deposited film, the red-shift of  $E_1$  relative to the single crystal value suggests significant strain in the film over the studied depth range of 1500-2000 Å; The maximum  $E_1$  energy shift of  $-0.12$  eV at a depth of 1500 Å converts to a stress level of 0.6 GPa which is also consistent with the energy shifts in the  $E_0$  band gap. The lower panel shows that the as-deposited film has a very large broadening parameter  $\Gamma_{E1} \sim 0.6 \pm 0.15$  eV, indicative of a very small grain size ( $\sim 10$  nm).
- Upon Ar annealing of the film, the strain nearest the substrate is significantly reduced as the grain size increases (reduced  $\Gamma_{E1}$ ). Even after 30 min of annealing in Ar, however, there is no significant reduction in the grain size within 500 Å of the surface, and the strain in this region increases somewhat relative to the as-deposited film (as indicated by

- the lower  $E_1$  energy).
- A 5 min  $\text{CdCl}_2$  treatment leads to an  $E_1$  energy within 10 meV of the single crystal value throughout the thickness, suggesting a fully strain-relaxed film. In addition,  $\Gamma_{E1}$  has been reduced significantly to a constant value of  $\Gamma_{E1} \sim 0.30 \pm 0.02$  eV throughout the bulk of the film, indicating a significant increase in grain size.

### 2.1.3 Etch back studies of CdTe solar cells ( $\text{CdCl}_2$ treated TEC-15/CdS/CdTe, Sample # asc34)

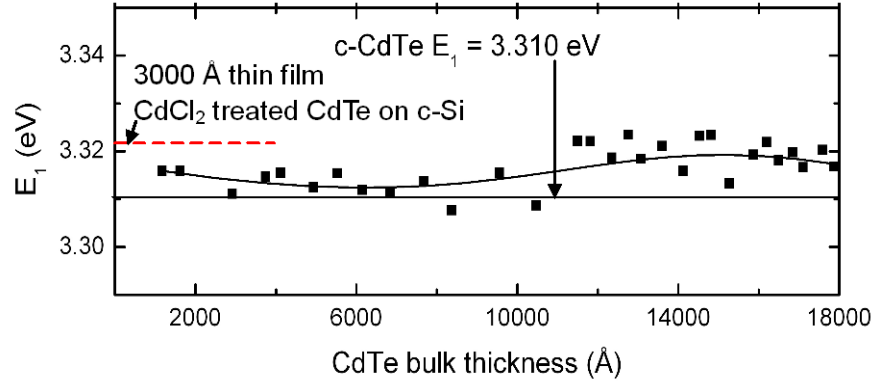


**Figure 2.3** Energy of the  $E_1$  transition as a function of CdTe bulk layer thickness in successive  $\text{Br}_2$ -methanol etching steps for a sputtered CdTe solar cell. Also shown is the constant energy of the  $E_1$  transition of thin film CdTe (3300 Å thick) fabricated on a c-Si wafer substrate after 5 minutes  $\text{CdCl}_2$  treatment (sample (iii) of fig 2.2).

The  $E_1$  energy of the CdTe layer remains close to the single crystal value [1] from 1000 Å to 1.8  $\mu\text{m}$ , indicating stress relaxation throughout the thickness of the solar cell.

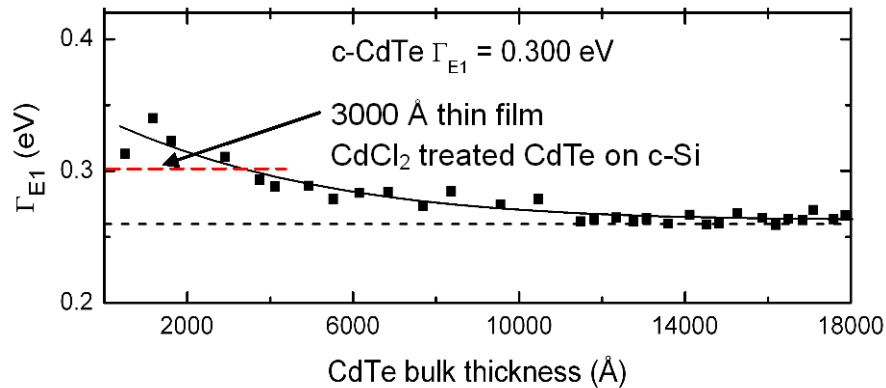


**Figure 2.4** Broadening parameter  $\Gamma_{E1}$  as a function of CdTe bulk layer thickness in successive  $\text{Br}_2$ -methanol etching steps for a sputtered CdTe solar cell. Also shown is the constant width of the  $E_1$  transition of thin film CdTe (3300 Å thick) fabricated on a c-Si wafer substrate.

- Because the value  $\Gamma_{E1} \sim 0.26 \pm 0.01$  eV at the film surface side is less than that of single crystal CdTe, it suggests more careful measurements of the single crystal are needed. It is likely that surface scattering in the epitaxially grown single crystal [1] is the origin of the larger  $\Gamma_{E1}$  value.

- The gradual increase in  $\Gamma_{E1}$  as the interface to the CdS is approached indicates that the electron mean free path is decreasing toward this interface. There may be two causes of this behavior:  
 (i) a reduction in grain size toward the CdS interface; or (ii) S diffusion into the CdTe.

## 2.2 Ex situ SE Measurements of CdTe Solar Cells

### 2.2.1 TEC-15 optical properties

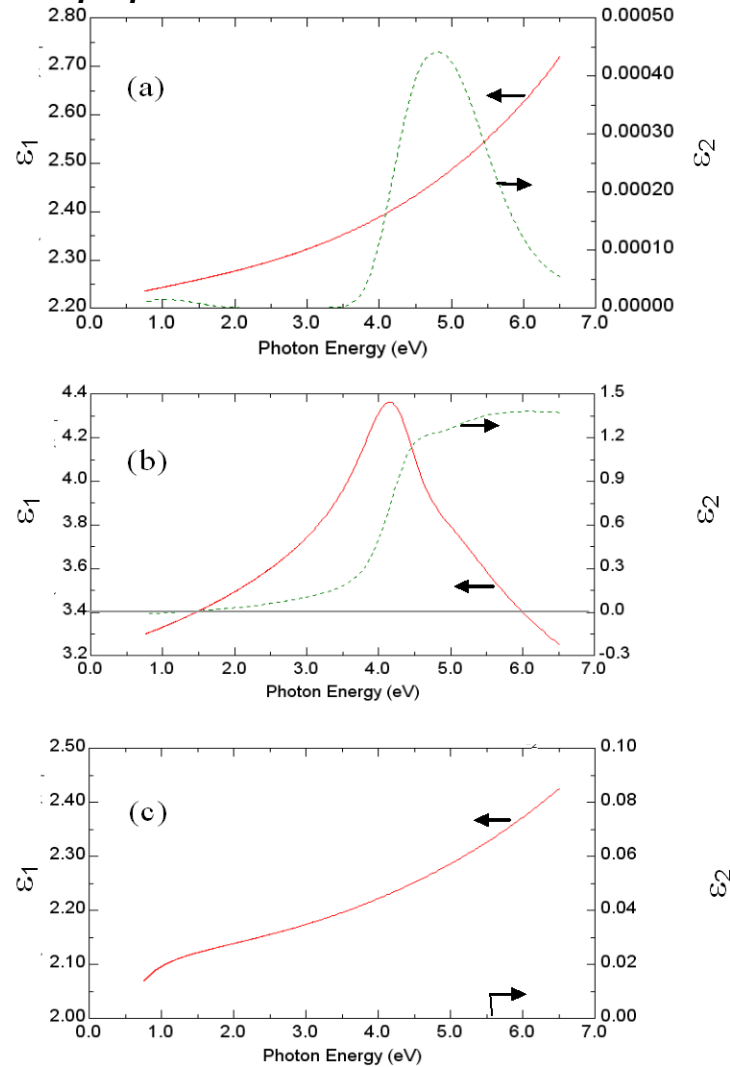


**Figure 2.5** Optical properties expressed in terms of the dielectric function for three of the four components of TEC-15 glass including (a) the soda lime glass substrate, (b) the near-substrate undoped  $\text{SnO}_2$ , and (c) the  $\text{SiO}_2$  interlayer.

- Dielectric functions of the components of TEC-15 glass have been determined including (a) the soda lime glass substrate, (b) the near-substrate undoped  $\text{SnO}_2$ , and (c) the  $\text{SiO}_2$  interlayer. These can be used in modeling the structure of the CdTe solar cell on the TEC-15 glass substrate.



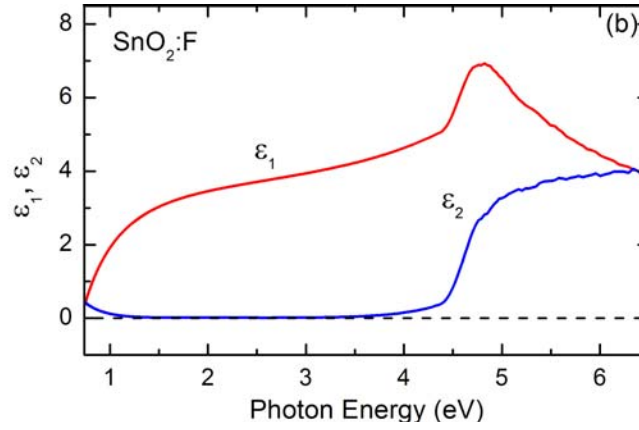


**Figure 2.6** Dielectric functions of  $\text{SnO}_2\text{:F}$ , the top-most thickest layer of the TEC-15 glass. For photon energies above 5 eV, the  $\text{SnO}_2\text{:F}$  is opaque, and the optical properties are extracted from  $(\Psi, \Delta)$  via inversion, correcting for surface roughness.

The dielectric function of  $\text{SnO}_2\text{:F}$ , the top-most thickest layer of the TEC-15 substrate, has been determined for use in modeling the structure of CdTe solar cells on TEC-15 glass substrates.

### 2.2.2. Optical modeling of etch-smoothened CdTe solar cells [2] ( $\text{CdCl}_2$ treated TEC-15/CdS/CdTe, Sample # asc34).

CdTe surface roughness	CdTe/void = 0.5/0.5	$35 \pm 0.4 \text{ \AA}$	TEC15 structure
CdTe bulk	CdTe/void = $0.96 \pm 0.002 / 0.04 \pm 0.002$	$14529 \pm 32 \text{ \AA}$	
CdTe/CdS interface	CdTe/CdS = $0.5 \pm 0.02 / 0.49 \pm 0.02$	$935 \pm 10 \text{ \AA}$	
CdS bulk	CdS/void = $0.93 \pm 0.001 / 0.07 \pm 0.001$	$1247 \pm 25 \text{ \AA}$	
CdS/ $\text{SnO}_2\text{:F}$ interface	CdS/ $\text{SnO}_2\text{:F}$ = 0.5/0.5	296 Å	
$\text{SnO}_2\text{:F}$	$\text{SnO}_2\text{:F}$ = 1.00	3178 Å	
$\text{SiO}_2$	$\text{SiO}_2$ = 1.00	215 Å	
$\text{SnO}_2$	$\text{SnO}_2$ = 1.00	267 Å	Soda lime glass
Soda lime glass	glass = 1.00	semi-inf.	

**Figure 2.7** Structural model for the CdTe solar cell after the 15<sup>th</sup>  $\text{Br}_2$ +methanol etch step used for surface smoothening. This model provides the best fit to ex situ SE data collected from the free CdTe surface.

- A multilayer stack has been established that successfully simulates SE data for determination of the structure and composition of the individual layers of the etched CdTe solar cell on TEC-15 glass substrates.
- It incorporates (i) an optical structure for TEC-15 consisting of  $\text{SnO}_2$  (267 Å);  $\text{SiO}_2$  (215 Å); and  $\text{SnO}_2\text{:F}$  (3178 Å); (ii) an interfacial roughness layer between the TEC-15 and the CdS whose thickness is chosen to match the surface roughness thickness measured from

the uncoated TEC-15 and whose composition is a fixed 0.5/0.5 effective medium mixture of the overlying and underlying materials.

- A single effective medium layer of CdS+CdTe of variable composition satisfactorily represents the complex layer at the CdS/CdTe interface; (see discussion of Fig. 2.10). The CdS/SnO<sub>2</sub>:F interface layer in this model is assumed to be the result of the surface roughness on TEC-15.
- A wide photon energy spectral range (1.0 ~ 6.0 eV) is used in this analysis in order to determine the complete film structure including the TCO coatings on TEC glass. Thus, the 0.04 void fraction in the CdTe layer is an optical average throughout the layer thickness.

### 2.2.3. Through-the-glass measurements of the CdTe solar cell

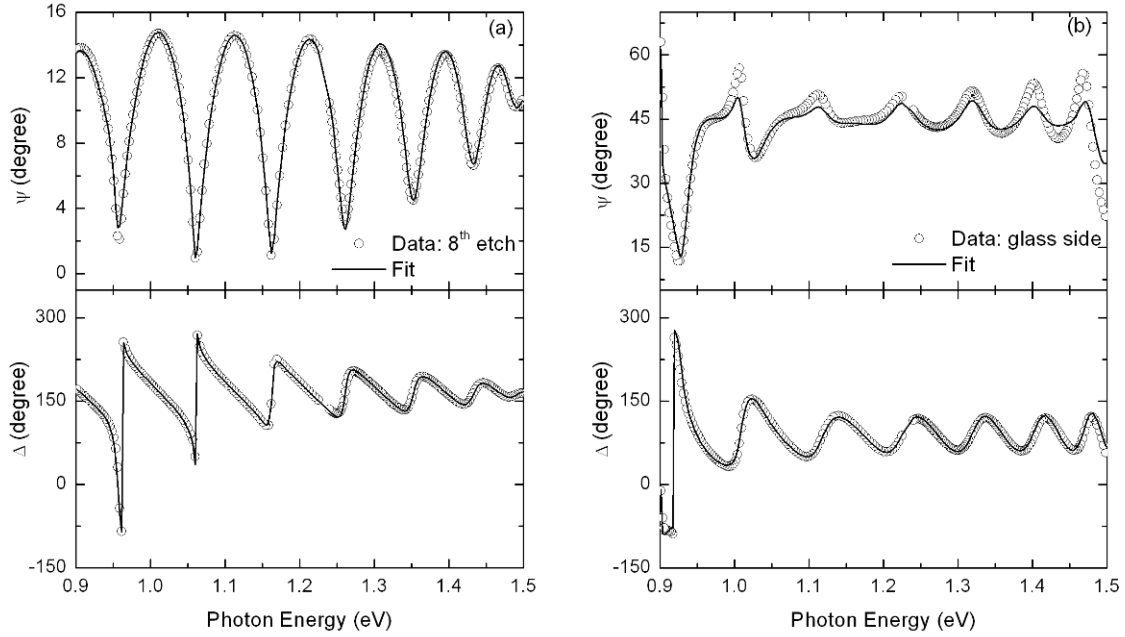


**Figure 2.8** Ex situ SE spectra in ( $\Psi$ ,  $\Delta$ ) (symbols) (a) from the free CdTe surface after 8 Br<sub>2</sub>+methanol etching steps and (b) from the prism/glass side without etching. The best fit results are given as the solid lines. In (b), a prism was affixed to the TEC-15 substrate with index-matching fluid to eliminate the top surface reflection from the top side (i.e., sun side) of the glass.

- In both studies, the best fit results (solid lines) yield the solar cell structural parameters, including the thicknesses of the CdTe roughness, CdTe bulk, CdTe/CdS interface, and CdS bulk layers, as well as the volume fractions of CdS/CdTe in the interface layer and void in the CdS layer.

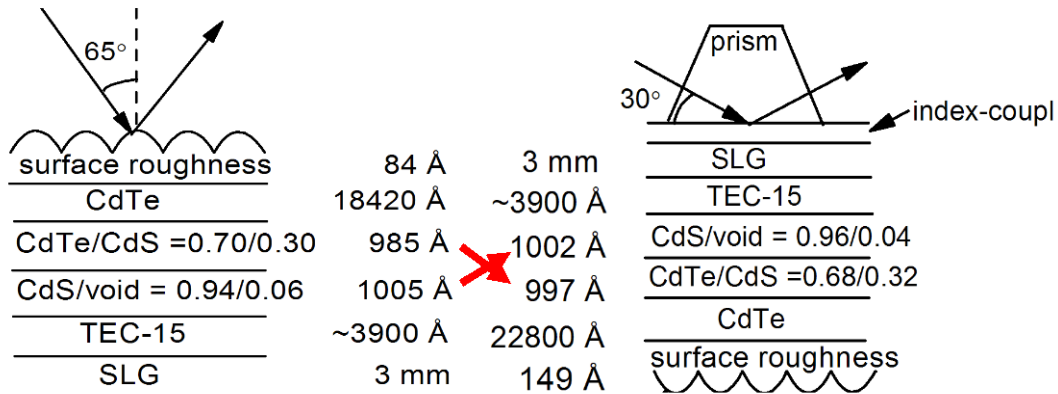


**Figure 2.9** A comparison of the structural parameters deduced from spectra collected from the CdTe surface after eight etching steps (left) and from spectra collected through the prism/glass (right).

- Excellent agreement in the critical CdS and CdTe/CdS interface layer thicknesses and compositional parameters are obtained. Agreement in the CdTe bulk and roughness layer thicknesses is not expected, however, since the CdTe film has been etched for the back side measurements (left).

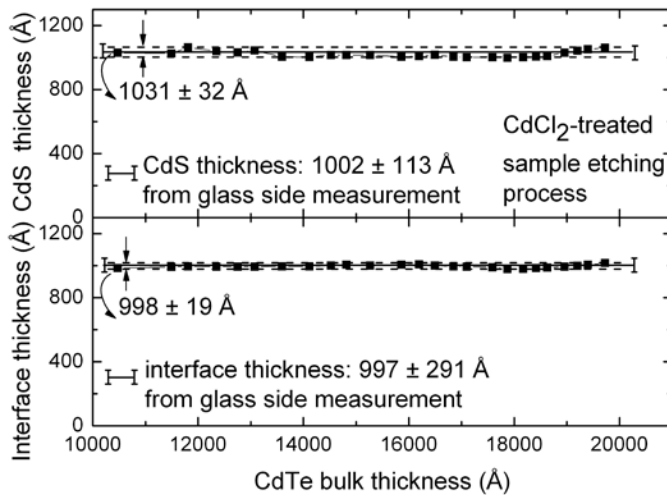


**Figure 2.10** CdS and CdTe/CdS interface layer thicknesses deduced from spectra collected through the prism/glass (solid line) and from spectra collected from the CdTe surface in successive etches (points, dotted line extreme).

- The CdS layer and CdTe/CdS interface thicknesses have been deduced from spectra collected at the CdTe free surface in 24 successive etches.
- These independent values for CdS/CdTe interface layer thickness and CdS bulk layer thickness should be constant since the etching does not affect the sub-surface material, and any variations provide a measure of the uncertainty in these values.
- Maximum deviations of  $\pm 2\text{-}3\%$  from the average values are obtained and the average values lie within the confidence limits of the analyses performed on spectra collected through the prism/glass
- The (CdS+CdTe) interface layer is modeled as a vol. fraction mixture of CdS/CdTe; however, this mixture merely provides a dielectric function that approximates that of the interface region and should not be interpreted physically. In fact, this layer requires a more complex model that includes interdiffusion using  $\text{CdTe}_{1-x}\text{S}_x$  and  $\text{CdS}_{1-x}\text{Te}_x$  alloy

dielectric functions. Further study of the dielectric function of an alloy series is reported in Sec. 4.

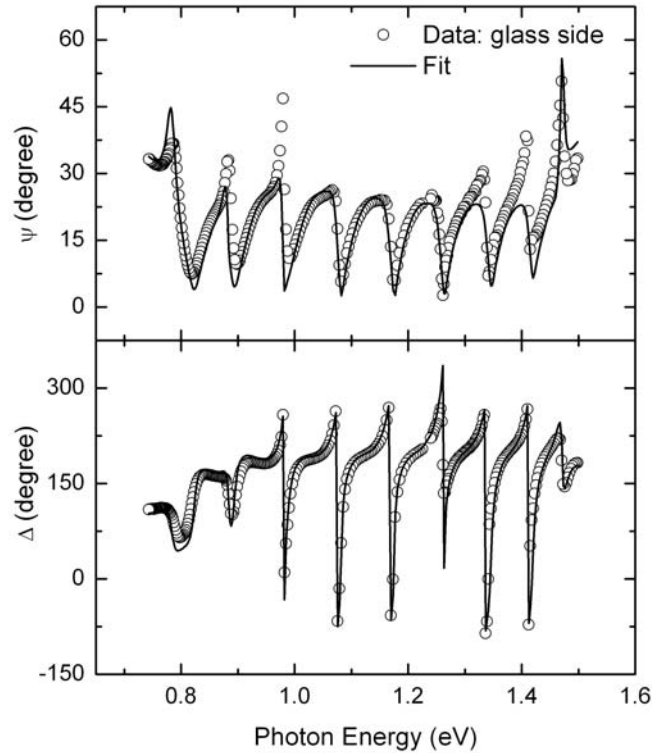


**Figure 2.11** Ellipsometric spectra (symbols) as measured through the glass without a prism for a CdTe solar cell obtained after CdCl<sub>2</sub> treatment and before back contact formation. Also shown is a best fit (solid lines).

- An new through-the-glass optical approach has been developed for on-line measurement of CdTe solar modules. This approach consists of blocking the top surface reflection from the glass and only measuring the beam reflected from the TEC-15/solar cell interface.
- These more expanded results provide information on the starting TEC-15, namely, the thickness of the undoped SnO<sub>2</sub> at the glass interface, the thickness of the SiO<sub>2</sub> layer, and the thickness of the doped conducting SnO<sub>2</sub>:F layer. In terms of the solar cell properties, the analysis provides information on the interface roughness between the CdS and the SnO<sub>2</sub>:F, as well as the thickness of the CdS, the combined roughness-interaction thickness between the CdS and CdTe, and the thickness of the CdTe.

### 2.3 Future Directions

We are currently seeking improvements in the above approaches while simultaneously applying them to assist research and development efforts at University of Toledo and production efforts in collaboration with Toledo area glass and CdTe module manufacturers. This represents a continuing research program and the following directions are currently being pursued.

- Improvements in the etch-back process are being sought using improved etching chemistries that minimize the thickness of the residual amorphous Te layer on the surface. Single-crystal CdTe provides a convenient test surface for evaluating the a-Te layer thickness in etch-back procedures. For the current etch-back analysis and any future ones to be developed, it is important to incorporate the a-Te layer in the data analysis. Although the layer is very thin, accurate modeling of the layer may improve the ability to extract other details of the overall sample structure.
- Improvements in the dielectric function database used in ex situ measurements are continually being sought. This includes an improved set of dielectric functions of TEC-15 components achieved through recent advances in modeling, as well as additional parameterization of CdS and CdTe dielectric functions versus temperature, strain, grain size, alloying, and defects. New and ongoing studies of ion-implanted CdTe as well as CdTe and CdS with low levels of S and Te alloying, respectively, are motivated by the need to develop new databases.
- Module scanners having the capability of off-line and on-line mapping are being developed for use by local manufacturers with the assistance of a U.S. optical instrumentation company. The ex situ measurement technology developed in this subcontract is to be exploited in this application.

### 3. Real Time Spectroscopic Ellipsometry: Dielectric Functions and Structural Evolution

In this section, the application of real time SE to understand better the growth mechanisms of sputtered CdTe and CdS films is described. The focus is on the use of smooth, native-oxide covered crystal Si wafer substrates. The thin SiO<sub>2</sub> layer simulates a disordered glass surface whereas the very smooth, abrupt interface between the native oxide and underlying silicon makes it possible to explore the monolayer level interactions during the nucleation and coalescence of the overlying film. Once coalescence occurs, then it is expected that the film growth on Si wafers more closely reflects the deposition of actual solar cell layers on TCO-coated glass, albeit with a much smoother surface. The studies during the subcontract period focused on technique development, and an in-depth analysis of three series of depositions, a temperature series for CdTe, a temperature series for CdS, and a pressure series of CdTe.

In terms of technique development, a number of capabilities have been established for in-depth analysis of growth:

- separation of the film into bulk and surface roughness layer components whose thicknesses can be tracked versus time;
- determination of deposition rates including the instantaneous bulk layer rate and the total effective rate, the latter including the contribution from both roughness and bulk layer components; and
- determination of step-wise void profiles to simulate the continuous variation in film density during growth.

Using these capabilities various interesting features have been observed as a function of deposition temperature and pressure. For example, the initial stages of growth of both CdTe and CdS show features consistent with a transition from a Vollmer-Weber type growth mechanism at low temperatures, with dominant initial clustering, to Stranski-Krastinov growth at high temperatures, with dominant initial layer-by-layer growth -- followed by clustering.

After nucleation and coalescence for CdTe, the resulting void fraction depends sensitively on substrate temperature and Ar pressure with the higher temperature and pressure films showing a higher void volume fraction. Thus, the densest CdTe films are obtained at the lowest temperatures and pressures. Films prepared at 180°C are extremely dense but undergo a microstructural transition to high void density after a thickness of ~1500 Å, apparently induced by significant compressive strain in the dense films. This effect in conjunction with the general increase in void volume fraction with increasing substrate temperature leads to a minimum in the void volume fraction for 3000 Å thick CdTe films deposited at the intermediate temperature of ~230°C. The results as a function of pressure are surprising in that at the lowest attainable deposition pressure, the highest densities and smoothest films are obtained throughout the deposition process. In fact 1 µm thick films can be prepared at 2.5 mTorr Ar pressure with void fractions no greater than 0.03 and with surface roughness thicknesses no greater than 20 Å throughout the entire deposition process. For CdS, the observed variations in the void fraction with temperature are much weaker than those for CdTe.

In addition to providing structural information, the real time SE measurements can be applied to extract the dielectric functions of the depositing layers. The dielectric functions are most accurately obtained in the thin layer regime (500 - 1000 Å) before the development of extensive surface roughness and void structures that generate non-uniformity with depth. Typically the depositions are suspended at a thickness in this regime for stepwise cool-down, enabling the

dielectric function to be obtained versus temperature, starting from the deposition temperature and ending down at room temperature. Then the room temperature dielectric functions of films prepared under different deposition conditions can be compared based on SE measurements performed under fixed environmental conditions (at room temperature and under vacuum). This also enables greater averaging times for higher precision spectra.

Dielectric functions obtained under these conditions tend to be more accurate than those by any other method because: (i) they are obtained in situ which avoids native oxides; (ii) they employ the substrate optical properties and characteristics (e.g., native oxide thickness) in the optical model that were obtained from measurements made prior to film growth on the substrate, and (iii) they employ surface roughness thicknesses in the optical model that were obtained in situ during film growth. As a result, these dielectric functions are superior for use as reference data in ex situ analysis of solar cell structures as described in the previous section. Furthermore, such dielectric functions can then be analyzed carefully to develop databases that enable one to extract information on grain size, defect density, strain, and temperature. The results of this latter effort are presented in Section 4.

### 3.1 Overview of CdTe and CdS Dielectric Functions

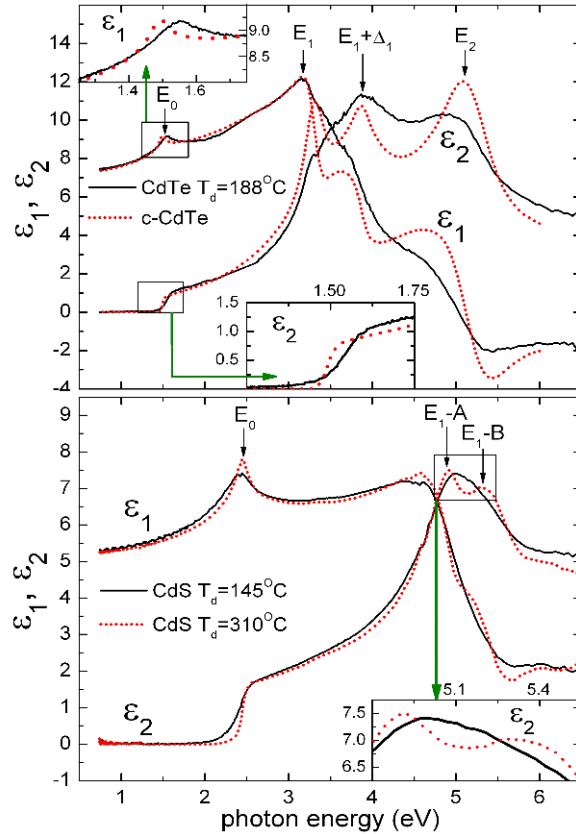


**Figure 3.1** 15°C complex dielectric functions  $\epsilon$  of typical polycrystalline CdTe (upper) and CdS (lower) films magnetron sputtered using the indicated deposition temperatures ( $T_d$ ). Additional parameters are as follows -- CdTe: rf power of 60 W and Ar pressure of 18 mTorr; CdS: rf power of 50 W and Ar pressure of 10 mTorr. Also plotted in the upper panel is the room temperature  $\epsilon$  of single crystal CdTe [1].

- The film dielectric functions are determined from in situ spectroscopic ellipsometry (SE) data taken after cooling the film down to 15°C from  $T_d$  and from film structural parameters

(thickness, roughness, ...etc.) deduced from real time SE (RTSE) data taken during deposition. The critical points (CPs) are marked.

- The differences in CP features (resonance energy, broadening,...etc.) are associated with important material properties (temperature, stress, grain size, ...etc.) that depend on preparation conditions as explained in Sec. 4.

### 3.2. CdTe and CdS Structural Evolution on Si Substrates as Measured by RTSE

#### 3.2.1. Role of substrate temperature for CdTe and CdS

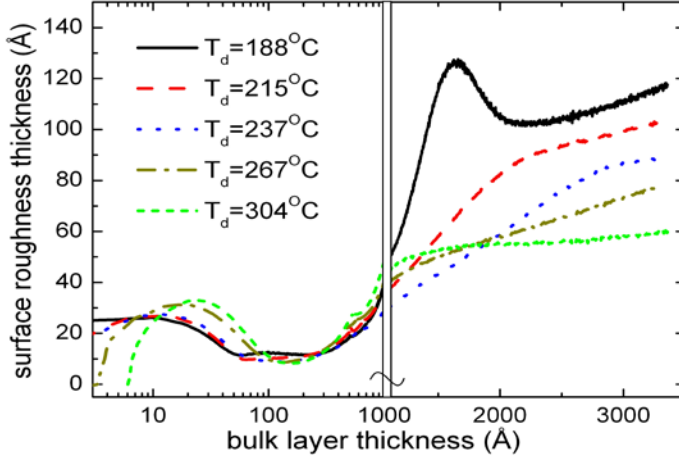


**Figure 3.2** Surface roughness thickness ( $d_s$ ) evolution with bulk film thickness ( $d_b$ ) for CdTe films magnetron sputtered on c-Si wafer substrates held at different temperatures ( $T_d$ ) but with otherwise identical deposition parameters (rf power of 60 W and Ar pressure of 18 mTorr).

- The nucleation stage (left) shows a monotonic change from the Volmer-Weber (V-W) growth mode, or island growth mode, at lower  $T_d$  to the Stranski-Krastanov (S-K) growth mode, or layer-island growth mode, at higher  $T_d$ .
- The longer term  $d_s$  evolution (right, when  $d_b > 2000$  Å) shows monotonic trend of surface smoothing at higher  $T_d$ .
- Both trends are consistent with enhanced surface diffusion at higher  $T_d$ .

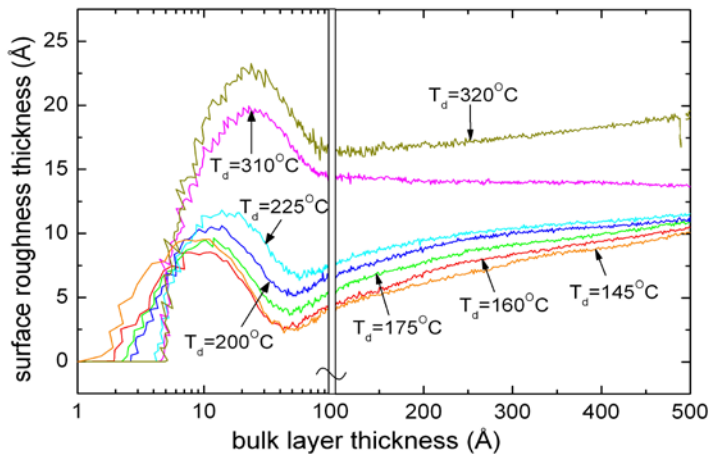


**Figure 3.3**  $d_s$  vs.  $d_b$  evolution for CdS films sputtered on c-Si wafer substrates held at different  $T_d$  but with identical deposition parameters of fig 3.2.

- A monotonic change is observed from V-W growth mode with small nuclei height at lower  $T_d$  to S-K growth mode with large nuclei height at higher  $T_d$ . The longer term  $d_s$  evolution (right) resembles that observed for CdTe over a similar range of  $d_b$ .



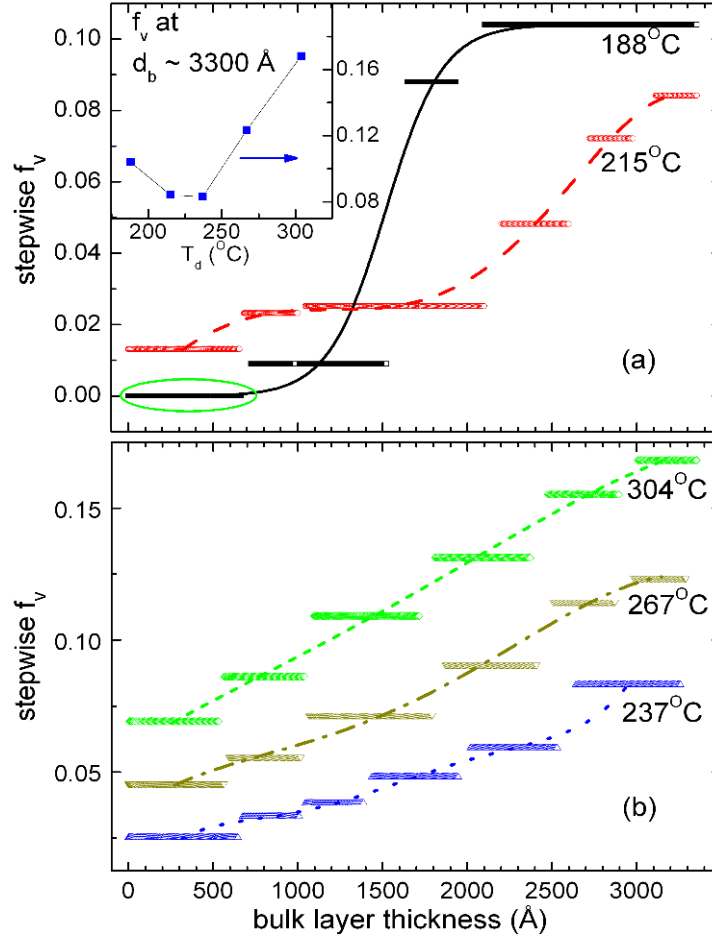


**Figure 3.4** Stepwise evolution of void volume fraction ( $f_v$ ) for the CdTe films of Fig. 3.2 magnetron sputtered on c-Si wafer substrates held at different  $T_d$ .

- For all  $T_d$ ,  $f_v$  increases monotonically with increasing bulk layer thickness.
- In the thin film regime ( $d_b < 500$  Å),  $f_v$  increases monotonically with increasing  $T_d$ .
- The lowest  $T_d$  film having the lowest  $f_v$  value in the initial stages, however, exhibits an abrupt structural transition at  $d_b \sim 1500$  Å where  $f_v$  increases by more than eight times within a narrow  $d_b$  range. This transition is attributed to strain relaxation and the effect is suppressed with increasing  $T_d$ , as the initial void fraction increases.
- $f_v$  in the top-most layer of the final film is shown as a function of  $T_d$  in the inset. The highest density in the near-surface region of the final film ( $\sim 3300$  Å) is obtained near  $T_d \sim 230^\circ\text{C}$ .
- It is reasonable that both surface roughness and voids provide means for strain relaxation in the films.

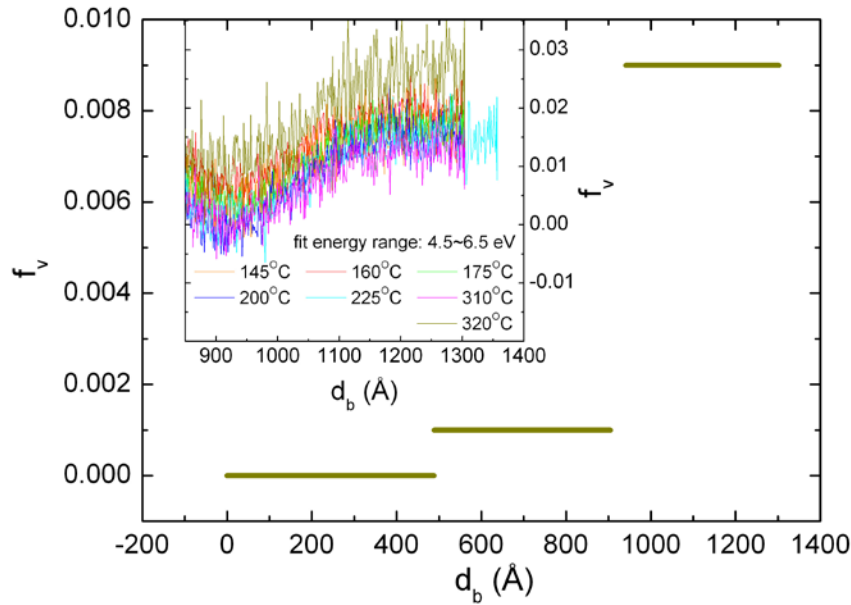


**Figure 3.5**  $f_v$  evolutions for the CdS films of Fig. 3.3 sputtered on c-Si wafer substrates held at different  $T_d$ .

- Void development for the deposited CdS films on crystalline Si is relatively weak compared to CdTe in the corresponding thickness range of interest for CdS ( $d_b < 1400$  Å).
- Stepwise void analysis of the CdS film grown at  $T_d=320^\circ\text{C}$  gives a final  $f_v$  of 0.01 (using RTSE data in full spectral range 0.75~6.5 eV, similar to that of Fig. 3.4). Other samples have similarly small results. No clear trend vs.  $T_d$  is observed.
- Continuous void analyses using RTSE data in the spectral range 4.5~6.5 eV, which is more sensitive to the surface of the sample, lead to a final near surface value  $f_v = 0.02 \pm 0.01$  for all the CdS films, again comparatively small.

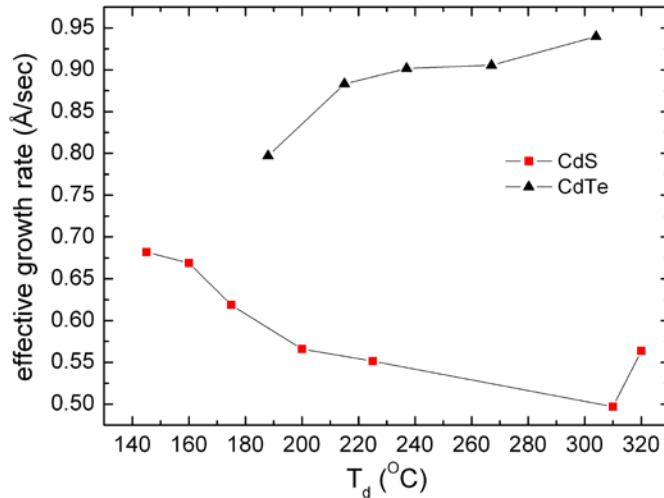


**Figure 3.6** Effective rate of material growth (excluding voids) as a function of  $T_d$  for the CdTe and CdS films of Fig. 3.2 and Fig. 3.3.

- The counterintuitive increase of rate with increasing  $T_d$  for CdTe films may be attributable to a reduction in Ar atom density with the increase in gas temperature at constant pressure and volume.
- The general trend of decrease of rate with increasing  $T_d$  for CdS films is consistent with a reduction in the sticking probability for the species at higher  $T_d$ .

### 3.2.2. Role of Ar pressure for CdTe

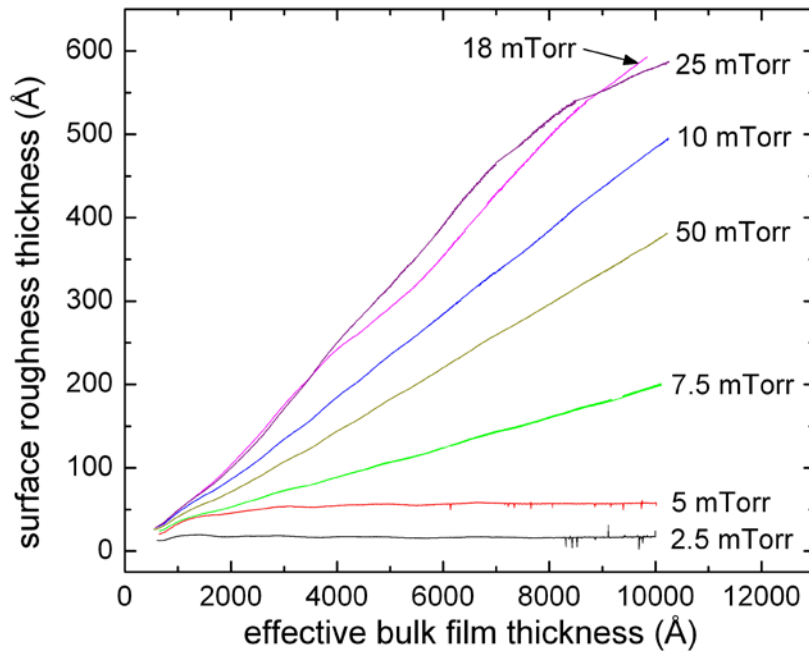


**Figure 3.7** Surface roughness evolution for magnetron sputtered CdTe with different Ar pressures and otherwise identical parameters, including a substrate temperature of 230°C and an rf power of 60 W.

- The surface roughness evolution strongly depends on the Ar pressure. Extremely low Ar pressure leads to a smooth surface throughout film growth; increasing Ar pressure leads to much faster roughness development, probably due to reduced surface diffusion which can smoothen the surface; but this effect reaches a maximum at ~18 mTorr; further increasing Ar pressure causes a reduction in surface roughness.

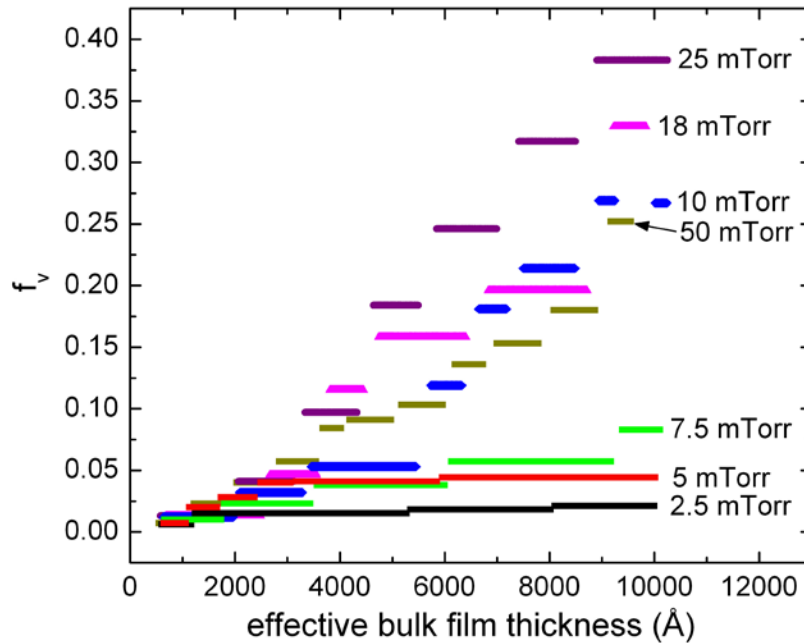


**Figure 3.8** Stepwise void evolution for the CdTe films of Fig. 3.7.

- A trend similar to that of surface roughness evolution is observed. Extremely low Ar pressure leads to a dense and uniform film through the deposition; increasing Ar pressure

leads to more rapid void development; but this effect reaches a maximum at ~25 mTorr; further increasing Ar pressure causes less voids in the film.

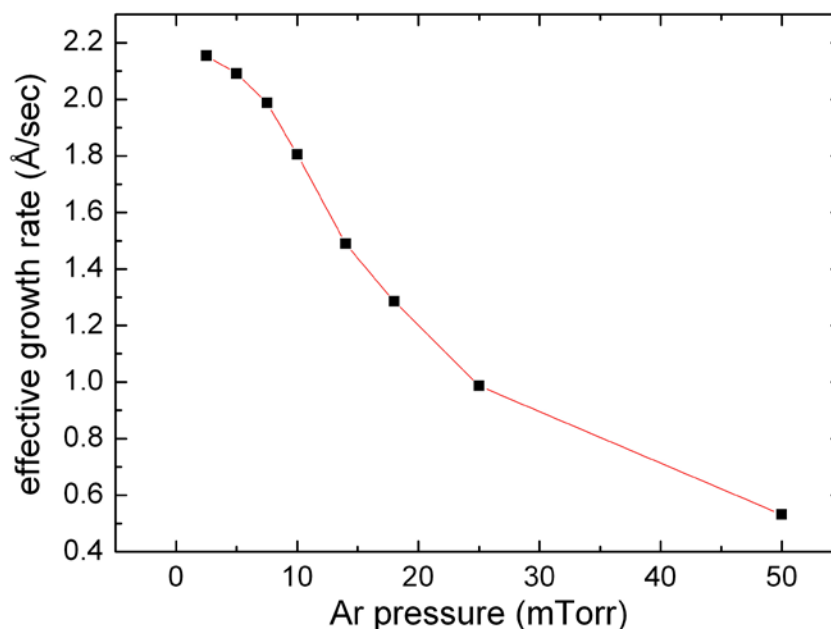


**Figure 3.9** Effective CdTe growth rate for the films of Fig. 3.7.

- A clear decrease of rate with increasing Ar pressure is observed, due to stronger scattering of species with higher Ar atom density in the gas phase.

### 3.3 Future Directions

The future directions for continuing real time SE studies of CdS and CdTe layers are quite clear. In future research, the analysis of the structural evolution in terms of bulk layer thickness, surface roughness layer thickness, and void volume fraction must be streamlined for depositions on crystalline Si wafer substrates. Then a wider range of deposition conditions can be explored expeditiously, including the roles of pressure for CdS growth, and sputtering power and substrate bias for CdS and CdTe growth. In addition, once streamlining has been achieved for more rapid turn-around in data analysis, then the ability to perform multistep processing becomes possible in order to control separately the interface, bulk, and surface structural properties, based on the understanding provided by real time SE.

In additional future studies, the focus will be on substrates that are relevant for solar cell fabrication. As a first step, 1300 Å thick CdS films will be deposited on Si wafers, as this leads to roughness layers no thicker than about 15 Å on the surfaces of the final films. Then CdTe films can be deposited in situ on the ultra-smooth CdS surfaces under different conditions. In this case -- in addition to the nucleation, growth, and structural characteristics of the CdTe film -- the alloying interaction of the depositing CdTe with the underlying CdS can be quantified. Initial studies in this area have been undertaken in the final phase of the subcontract, as will be highlighted in the next section; however, this work must be expanded to include variations in substrate temperature, Ar pressure, etc., for the overlying CdTe deposition.

The final step in such studies is to develop an understanding of how CdS grows on the transparent conducting oxide (TCO) surfaces used in the actual solar cells. The challenge in this case is to understand the chemical interactions that occur between the CdS and the TCO even in the presence of a rather thick roughness layer on the starting TCO surface. Because of such thick roughness layers, studies of the TCO/CdS interface are now proceeding in an ex situ mode since it is not clear how much additional useful information can be extracted in real time from such a difficult optical problem. As a result, initial attempts in studying TCO/CdS interface formation by real time SE may focus on TCO layers specially deposited for their smoothness, in order to better understand the chemical interactions, before proceeding to the more challenging case where roughness and chemical interactions must be handled simultaneously.

#### 4. In-Depth Analysis of the Dielectric Functions of CdTe and CdS

The previous section described how accurate dielectric functions have been extracted from in situ measurements performed after suspending the CdS or CdTe deposition at a thickness within the range of 500 - 1000 Å and cooling the resulting thin film to room temperature. These deduced dielectric functions have been analyzed assuming the standard parabolic band model in the neighborhood of the band structure critical points. An entire series of spectra collected at different measurement temperatures during cooling provide the critical point energies as a function of temperature. These results can then serve as a database for accurate substrate temperature calibration based on the critical point energy shifts that occur upon cooling the CdS or CdTe thin film sample from an unknown temperature to a known temperature.

The absolute critical point energies cannot be used for temperature calibration since these can shift significantly from sample to sample due to strain in the thin films. As a result, the critical point energies at a fixed temperature are found to provide information on strain. For CdTe deposited at different substrate temperatures, the strain shifts in the critical points energies obtained from room temperature dielectric functions are the largest for films deposited at low temperatures. The magnitude of this shift appears to correlate with the appearance of an abrupt structural transition in the subsequent evolution of the void volume fraction, which indicates that void development serves to relax strain in the network.

The critical point widths in the dielectric functions of CdS and CdTe are consistent with a model in which the lifetimes of the excitations are limited by scattering at defects, attributed to grain boundaries. We have associated a group velocity with each critical point of CdS and CdTe that relates the carrier mean free path and mean free time between grain boundary scattering events. The latter is inversely proportional to the broadening parameter of the critical point. With such a model, an optically-deduced grain size can be obtained, and particularly for CdS, the grain size is observed to increase systematically with substrate temperature.

These approaches that relate the dielectric function critical point energies and widths to strain and grain size, respectively, enable one to establish a database for the analysis of ex situ SE data. This database has been applied to CdCl<sub>2</sub> treated CdTe thin films in order to extract the strain and grain size as a function of depth in step-by-step etching procedures. In this way, it has been demonstrated that the CdCl<sub>2</sub> treatment significantly relaxes the strain in the network in addition to increasing the grain size since the critical point energies and widths approach those of the single crystal upon treatment.

The dielectric functions of alloys between CdTe and CdS have been determined using real time SE of thin films deposited by co-sputtering at low temperatures to avoid phase separation. This provides an additional database which has been demonstrated for depth profiling the composition when CdTe is deposited on CdS and vice versa.

## 4.1 Analysis Methodology

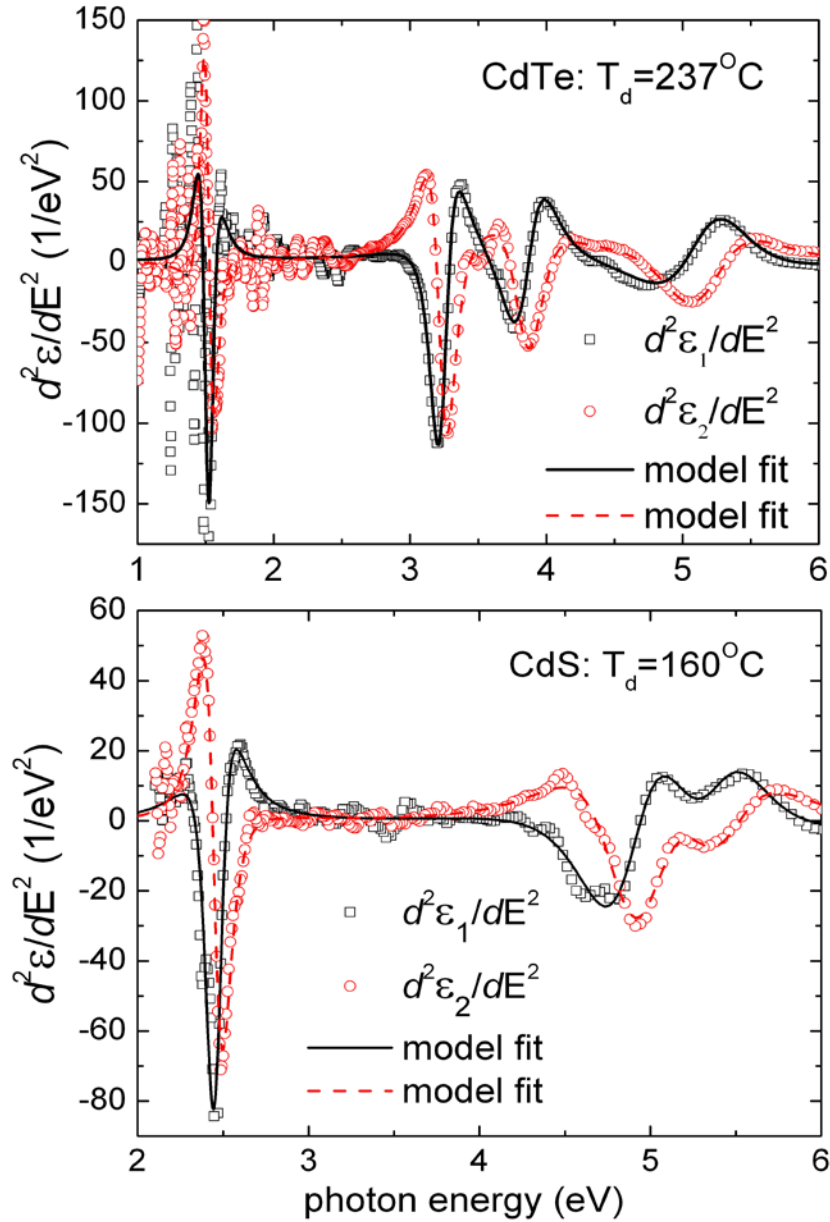


**Figure 4.1** The 2nd derivative spectra of typical 15°C dielectric functions  $\epsilon$  of polycrystalline thin films: (upper) the  $T_d=237^\circ\text{C}$  CdTe film of Fig. 3.2; and (lower) the  $T_d=160^\circ\text{C}$  CdS film of Fig. 3.3.

- The model fits are based on the critical point parabolic band approximation:

$$\epsilon = \sum A_n (E_n - E - i\Gamma_n)^{\mu_n} \exp(i\phi_n) \quad (1)$$

where  $A_n$ ,  $E_n$ ,  $\Gamma_n$ ,  $\mu_n$ , and  $\phi_n$  are the amplitude, band gap (resonance energy), broadening parameter (width), exponent, and phase of the  $n^{\text{th}}$  CP, respectively. These parameters are used to deduce physical information on the sample.

## 4.2 Critical Point Broadening Parameters and Grain Structure

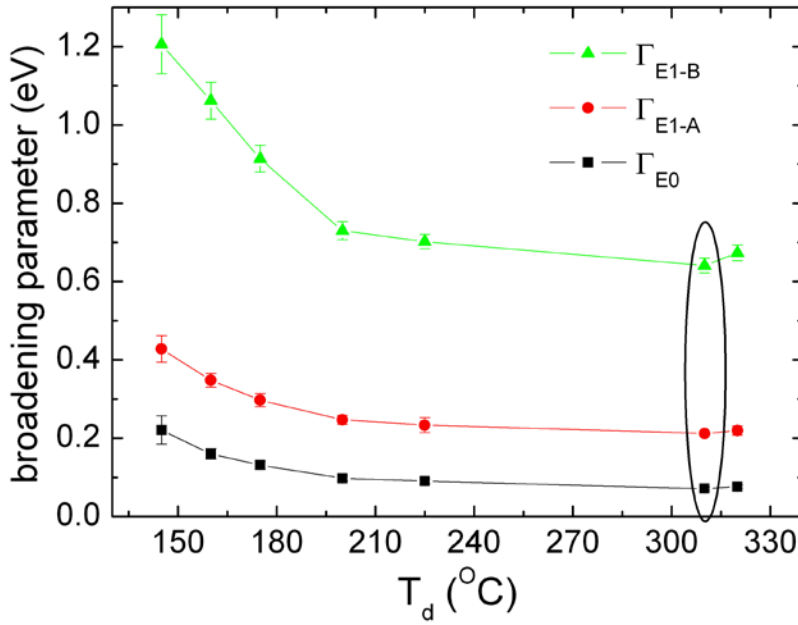


Figure 4.2 The broadening parameters at 15°C for the  $E_0$ ,  $E_1$ -A, and  $E_1$ -B CPs for the CdS films of Fig. 3.3; the lowest values are circled.

- The CP features of the  $T_d=310^\circ\text{C}$  film with the smallest  $\Gamma_n$  (circled) are even sharper than those of single crystal wurtzite CdS, as measured in this study and by S. Ninomiya *et al.* This is likely due to near-surface polishing damage on the single crystal. Thus,  $\Gamma_n$  for this sample can be taken as intrinsic to single crystal wurtzite CdS (denoted  $\Gamma_{bn}$ , b: "bulk"), and can be related to its band structure.

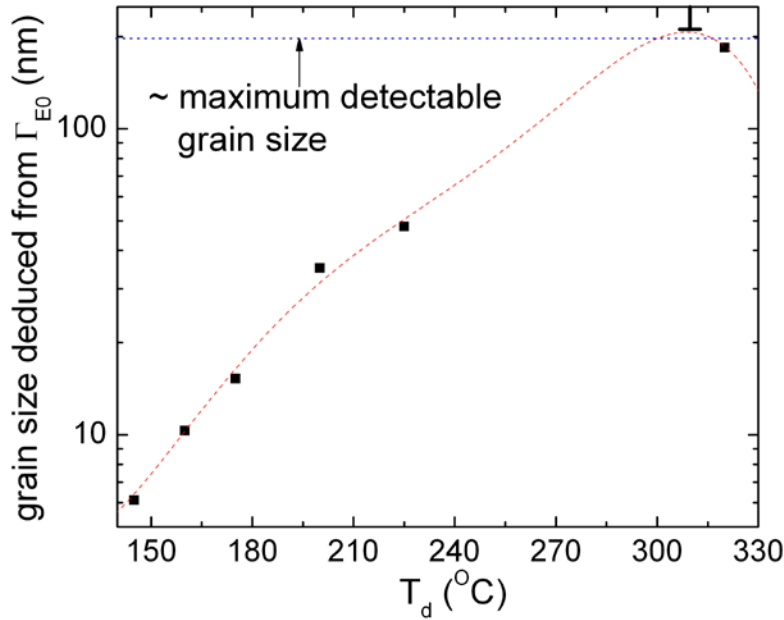


Figure 4.3 Grain size for the CdS films of Fig. 3.3, estimated from the near  $E_0$  band structure of wurtzite CdS, using the  $\Gamma_{E0}$  values in Fig. 4.2.



- According to the parabolic band approximation, the electron group velocity near  $E_0$  is  $v_{g,E0} = \{ \Gamma_{b,E0} m_h^* / [m_e^* (m_e^* + m_h^*)] \}^{1/2}$ , where  $m_e^*$  and  $m_h^*$  are electron and hole effective masses respectively. From the literature and from this work,  $v_{g,E0}$  of CdS was estimated to be  $\sim 2.2 \times 10^5$  m/s.
- If the dominant broadening effect in the films is taken to be the limited excitation lifetime due to grain boundary scattering, then the equation below can be applied:

$$\Gamma_n = \Gamma_{bn} + (h v_{gn} / R) \quad (1)$$

where  $v_{gn}$  is the group speed associated with the  $n^{\text{th}}$  CP,  $h$  is the Plank's constant, and  $R$  is the deduced grain size (radius).

- Using the values of  $v_{g,E0}$  and  $\Gamma_{b,E0}$  for single crystal wurtzite CdS,  $R$  of polycrystalline CdS films in Fig. 19 can be calculated versus  $T_d$ . The effect of  $T_d$  on  $R$  is strong: doubling  $T$  from  $\sim 150^\circ\text{C}$  to  $\sim 300^\circ\text{C}$  increases the grain size in as-deposited CdS films by  $\sim 30$  times.

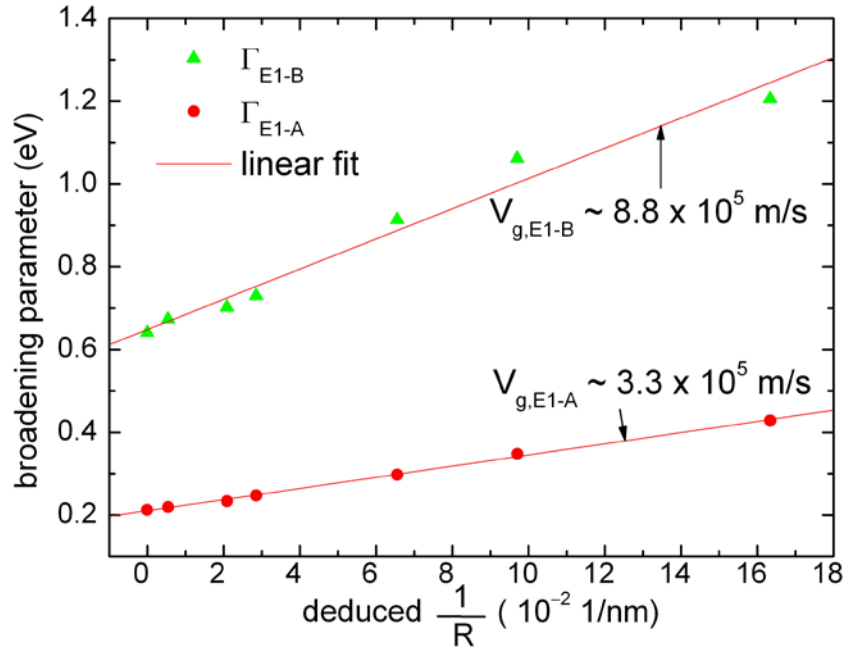


**Figure 4.4** The CdS  $E_1$ -A and  $E_1$ -B broadening parameters plotted vs. the reciprocal of the deduced grain radius Fig. 4.3. The group speeds of excited electrons associated with the  $E_1$ -A and  $E_1$ -B transitions are calculated from the linear fits and Equation (2).

- The linear relation between  $\Gamma_n$  and  $R^{-1}$  in Equation (2) should be applicable to all CPs, not only  $E_0$ , but with different slopes determined by  $v_{gn}$  and different intercepts determined by  $\Gamma_{bn}$ . As a check of the correctness of the concept, the broadening parameters  $\Gamma_{E1-A}$  and  $\Gamma_{E1-B}$  of the CdS samples are plotted versus  $R^{-1}$  (deduced from  $\Gamma_{E0}$ ) in Fig. 5.4. Equation (2) is closely followed. The group speeds associated with the  $E_1$ -A and  $E_1$ -B excitations are estimated from the slopes of the linear fits to be  $\sim 3.3 \times 10^5$  m/s and  $\sim 8.8 \times 10^5$  m/s, respectively.

### 4.3 Critical Point Energies and Strain

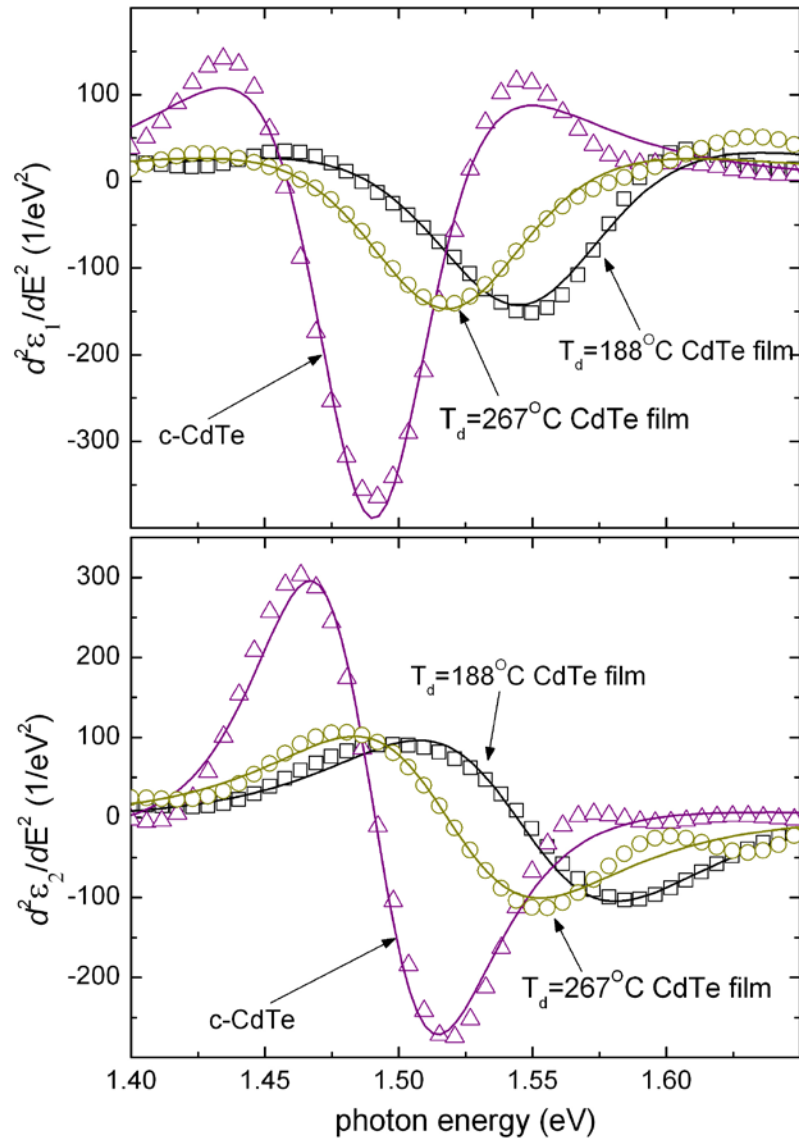


**Figure 4.5** The 2nd derivative spectra (symbols) of room temperature  $\epsilon$  for c-CdTe, and  $15^\circ\text{C}$   $\epsilon$  for the CdTe films with  $T_d=188^\circ\text{C}$  and  $T_d=267^\circ\text{C}$ . The model fits (solid lines) are based on a parabolic band critical point model.

- The blue shift of  $E_0$  resonance energy for CdTe films relative to that of c-CdTe is obvious, being as large as  $\sim 55$  meV. In general, the lower the deposition temperature, the larger the blue shift. This shift is considered to be caused by stress in the deposited films (see Fig. 4.6).

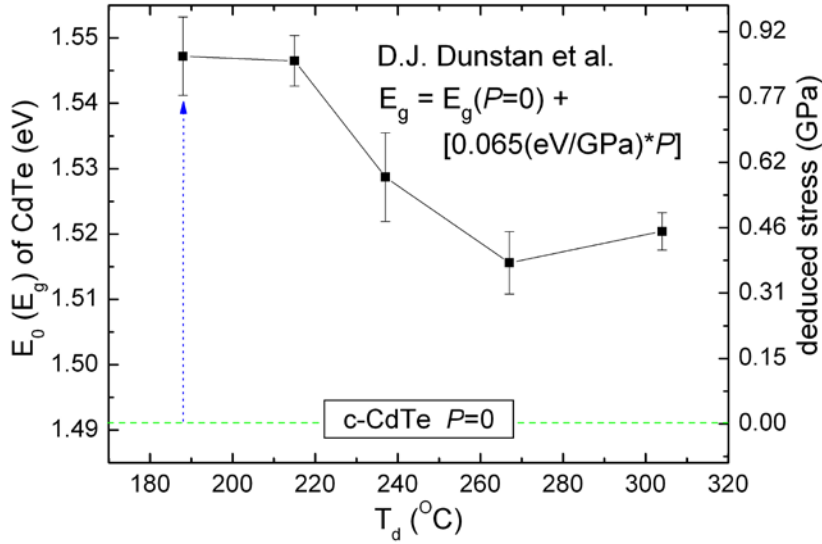


**Figure 4.6** 15°C  $E_0$  CP energies for CdTe films in Fig. 3.2. The stress (right scale) is calculated from the indicated equation. The horizontal dash represents the room temperature  $E_0$  for c-CdTe which is assumed to be stress free.

- Previous measurements that relate hydrostatic pressure to the fundamental band gap in single crystal CdTe by Dunstan et al. [3] have established a pressure coefficient  $C_P(E_0)$  of 0.065 eV/GPa. Although the stress in the CdTe films is uniaxial rather than hydrostatic, the estimate may be a reasonable one because the optical electric field is strongly refracted into the material and thus probes the high stress direction.
- For  $T_d$  above 220°C, these  $d_b \sim 1000$  Å CdTe films pass through a relaxation whereby the stress decreases by a factor of two over a  $\sim 50^\circ\text{C}$  range. The very high stress levels in the two lowest  $T_d$  films are consistent with the observed low  $f_v$  in this thickness range. For  $d_b > 1000$  Å, these low temperature films undergo abrupt structural transitions in which  $f_v$  increases significantly (see Fig. 3.4). For the two higher  $T_d$  films,  $f_v$  for  $d_b \sim 1000$  Å is higher and no structural transition is observed. Thus, a high initial stress is correlated with the appearance of a subsequent microstructural transition in the evolving film.

#### 4.4 Summary: Effects of Temperature, Grain Size, and Stress on the Critical Points of CdTe and CdS

**Table 4.1** Single crystal CP Energies and Widths, Temperature Coefficients of CP Energies and Widths, Electron Group Speeds, and Stress Coefficients of CP Energies for Major CPs for CdTe and CdS

CdS	$E_b(T_0)$ (eV)	$\Gamma_b(T_0)$ (eV)	$C_{T\Gamma}$ (eV/°C)	$C_{TE}$ (eV/°C)	$v_g$ (m/s)	$C_P$ (eV/GPa)
$E_0$	2.38	0.071	$2.0 \times 10^{-4}$	$-4.1 \times 10^{-4}$	$2.2 \times 10^5$	0.045
$E_1\text{-A}$	4.82	0.21	$4.8 \times 10^{-4}$	$-5.3 \times 10^{-4}$	$3.3 \times 10^5$	0.089
$E_1\text{-B}$	5.50	0.64	$16 \times 10^{-4}$	$-8.6 \times 10^{-4}$	$8.8 \times 10^5$	0.028
CdTe	$E_b(T_0)$ (eV)	$\Gamma_b(T_0)$ (eV)	$C_{T\Gamma}$ (eV/°C)	$C_{TE}$ (eV/°C)	$v_g$ (m/s)	$C_P$ (eV/GPa)
$E_0$	1.49	0.041	$1.2 \times 10^{-4}$	$-3.7 \times 10^{-4}$	$2.3 \times 10^5$	0.065
$E_1$	3.31	0.30	$2.2 \times 10^{-4}$	$-7.3 \times 10^{-4}$	$8.1 \times 10^5$	-0.20
$E_1 + \Delta_1$	3.89	0.29	$5.1 \times 10^{-4}$	$-2.5 \times 10^{-4}$	$6.9 \times 10^5$	0.23
$E_2$	5.16	0.92	$18 \times 10^{-4}$	$-2.7 \times 10^{-4}$	$4.2 \times 10^5$	0.16

- In the experimental range, parameterization can be applied to relate CP features to key film properties, including temperature, stress, and grain size:

$$\Gamma = \Gamma_b(T_0) + C_{IT} * (T_m - T_0) + (h\nu_g/R) \quad (3a)$$

$$E = E_b(T_0) + C_{TE} * (T_m - T_0) + C_P P \quad (3b)$$

where  $\Gamma_b$  and  $E_b$  are the width and CP energy of the single crystal;  $T_0$  is a reference measurement temperature, normally room temperature;  $C_{IT}$  and  $C_{TE}$  are the temperature coefficients of the CP width and CP energy, respectively;  $h$ ,  $\nu_g$  and  $R$  have the same interpretations as previously. This parameterization is potentially useful for spatially scanning and monitoring system for film properties on a solar cell production line.

- For a given layer, all the CPs share the same measurement temperature  $T_m$ , grain size  $R$  and stress  $P$ ; furthermore, for a given solar cell,  $T_m$  for CdTe and CdS are the same. In addition, for a series of cells of the same component materials (CdTe and CdS) but with different characteristics, the single crystal CP values,  $\Gamma_b$  and  $E_b$ , the CP coefficients,  $C_{IT}$  and  $C_{TE}$ , and the electron group speeds  $\nu_g$ , are all constants. As a result, this parameterization reflects not only interesting characteristics, but also provides a useful “interlocking” mechanism that can significantly reduce correlation and instrument-related drift.

## 4.5 Ternary Alloys Between CdS and CdTe

### 4.5.1 Dielectric functions of ternary alloys

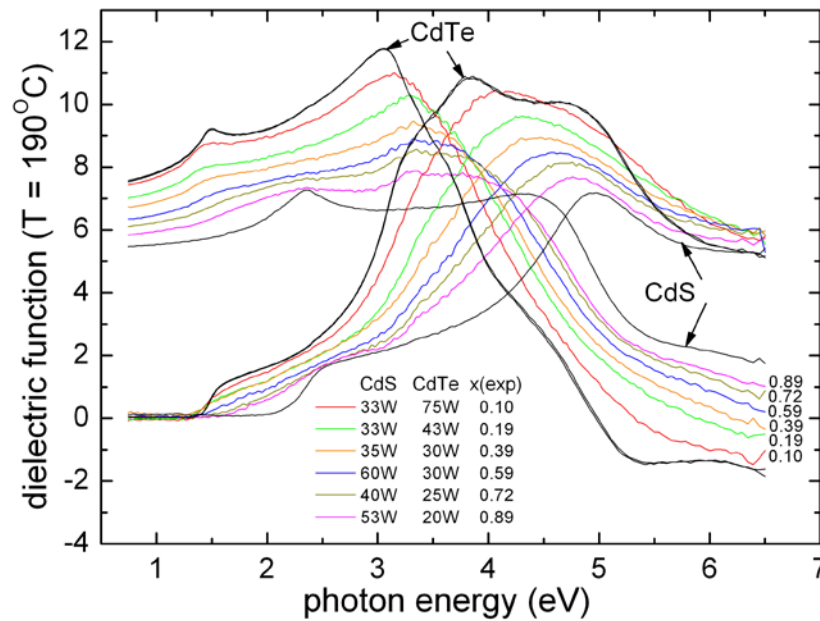


**Figure 4.7** Dielectric functions of co-sputtered  $\text{CdS}_x\text{Te}_{1-x}$  alloy films at 190°C.

- A rate vs. rf power calibration was performed for both CdTe and CdS. Different expected  $x$  values (as indicated) were achieved by applying different rf powers to the CdTe and CdS target (as indicated) during co-sputtering.
- Dielectric functions of co-sputtered  $\text{CdS}_x\text{Te}_{1-x}$  films vary consistently with expected  $x$ . This set of dielectric functions can serve as a database in the investigation of diffusion profile at the CdTe/CdS interface during junction formation.

#### 4.5.2 Analysis of alloy formation at CdS/CdTe and CdTe/CdS interfaces

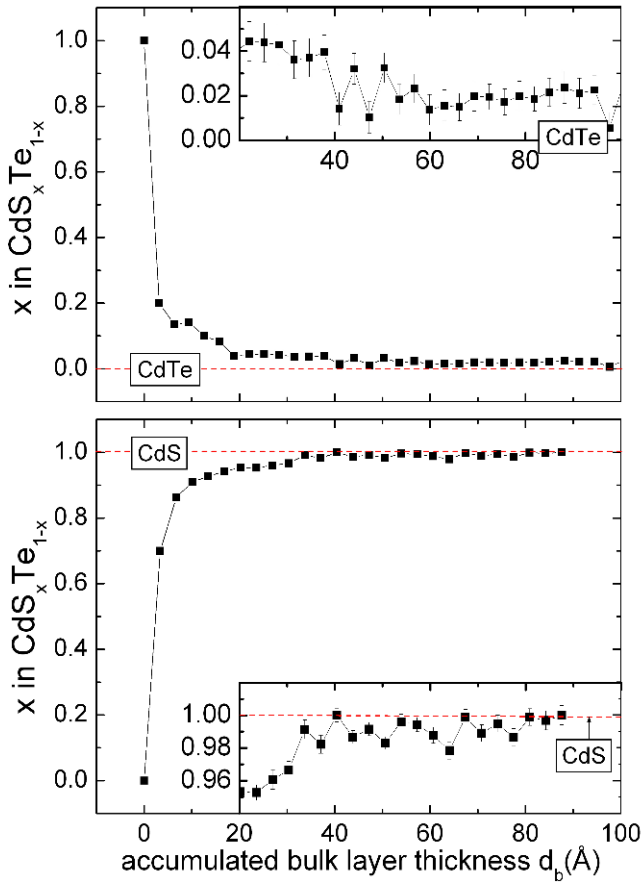


Figure 4.8 Composition profiles  $x(d_b)$  in  $\text{CdS}_x\text{Te}_{1-x}$  for depositions at  $190^\circ\text{C}$  for CdTe on CdS (upper) and CdS on CdTe (lower).

- A virtual interface approximation is applied to the RTSE data to find  $x$  for the topmost  $\sim 8 \text{ \AA}$  of deposited material during interface formation.
- In both deposition sequences, there is a  $\sim 40 \text{ \AA}$  layer with a strong gradient in  $x$ , possibly generated by ion impact in the sputtering process. Beyond this thickness, S diffusion into CdTe exhibits a tail with  $x \sim 0.02$ ; whereas for the inverted structure, Te diffusion into CdS exhibits a negligible tail.

#### 4.6 Future Directions

Although progress has been made in understanding the effects of temperature, strain, grain size, and Te and S alloying on the dielectric functions and critical points of CdS and CdTe, as exemplified in this section, many of the concepts and modeling approaches are oversimplified and need to be developed in greater depth.

- The temperature dependence of the critical points of the dielectric functions of CdTe and CdS have been well-established, and the observed temperature coefficients are independent of the film characteristics of strain and grain size within experimental confidence limits; however, the effect of alloying on these coefficients has yet to be established.
- In the case of strain, a simple model of hydrostatic pressure has been used to explain the shifts in the  $E_0$  fundamental gap of CdTe. Using these  $E_0$  shifts as a measure of the pressure, linear pressure coefficients can be derived that account for the observed shifts in

the other critical points. However, such a model may not be expected to work in all circumstances. Because the strain is greatest in the plane of the film, the simple model will not be applicable when the film is preferentially oriented. Thus, future efforts will focus on the determination of the full spectroscopic strain-optic tensor using the recently-developed Mueller matrix ellipsometry method designed for anisotropic optical responses. Under ideal circumstances, information on crystallite orientation may be accessible by determination and consideration of the energy shifts of the full set of critical points.

The model for grain size is similarly over-simplified, based on a model of spherical, randomly-oriented grains. To assess the robustness of the model, defects other than grain boundaries are being introduced into single crystal CdTe as scattering centers to determine if the same set of group velocities can explain the broadening that is observed. This effort will continue in future research.

## 5. HREM, EXAFS and XES Studies of CdTe cells

### 5.1 Introduction

We have performed a series of studies to identify the location and bonding of copper in our sputtered CdTe cells. These studies used EXAFS measurements at the Argonne Advanced Light Source, high resolution electron microscopy at the University of Michigan, and photoelectron spectroscopy at the University of Nevada Las Vegas.

Through the collaboration with the Electron Microbeam Analysis Laboratory (EMAL) at the University of Michigan, a subnanometer Cu-rich layer has been observed at the interface between the CdTe and the Au contact in High Resolution Transmission Electron Microscopy images (cross sectional) from our complete cell structure. The diffusion of Cu into the Au layer is also confirmed by cross-sectional, fine-probe EDS spectra and fine-probe EDS mapping. We used a JEOL 3011 ultra-high resolution microscope ( $\sim 0.17\text{nm}$ ) and a JEOL 2010F analytical electron microscope that can be operated either in TEM or STEM mode ( $\sim 0.17\text{ nm}$ ).

In order to study the local structural changes of copper in completed CdTe cells using EXAFS at the Advanced Photon Source at Argonne, we prepared sputter-deposited CdS and CdTe layers on fused silica substrates. With this structure similar to a complete solar cell, a built-in field at the p-n junction is established which is expected to affect the diffusion of copper atoms through CdTe into CdS, yet without x-ray fluorescence contamination from the soda-lime glass normally used. The probable existence of  $\text{Cu}_2\text{O}$  is confirmed by EXAFS collected at Materials Research Collaborative Access Team (MR-CAT) beamline at the Advanced Photon Source (Argonne, IL). A Cu/Au alloy structure is also found through the theoretical fitting and confirmed by our x-ray fluorescence study of peeled-off Au contact layer (Phase I Quarter 3 report).

In this final report we focus on the analysis of the High Resolution Electron Microscopy studies and of an interfacial copper-oxide layer between the CdTe and Au layers in our standard sputtered CdS/CdTe devices.

### 5.2 Sample Preparation

Our standard CdS/CdTe devices are fabricated by magnetron sputtering in a conventional structure on 3 mm TEC-7 glass. The  $0.13\text{ }\mu\text{m}$  CdS and  $2.2\text{ }\mu\text{m}$  CdTe films were deposited without vacuum break followed by a 30 minute  $\text{CdCl}_2$  vapor treatment with the temperature of sample at  $397^\circ\text{C}$  and  $\text{CdCl}_2$  source at  $392^\circ\text{C}$ . As the next step,  $40\text{ \AA}$  Cu and  $200\text{ \AA}$  Au layers were evaporated onto the chloride-treated films. The devices were then finished with a low temperature “diffusion” process at  $152^\circ\text{C}$  in ambient air for 52 minutes. The average performance of these cells is:

$$\text{Eff} = 11.9\%, \text{Voc} = 800\text{mV}, \text{Jsc} = 20.7\text{ mA/cm}^2 \text{ and FF} = 71.6\%.$$

In order to study the bonding and migration of copper in a structure as close as possible to our standard cells, we sputter-deposited at  $250^\circ\text{C}$   $0.13\text{ }\mu\text{m}$  CdS and  $2.3\text{ }\mu\text{m}$  CdTe layers on fused silica substrates without TCO coating, but otherwise the same as the deposition on regular TEC glass. A standard vapor  $\text{CdCl}_2$  treatment was carried out, followed with  $35\text{ \AA}$  Cu and  $200\text{ \AA}$  Au depositions by evaporation. The process was finished with the same 45 minute thermal activation at  $150^\circ\text{C}$  in ambient air. Cu K-edge EXAFS spectra and x-ray fluorescence (XRF) spectra were collected from these samples. Data were obtained at the MR-CAT beamline at the Advanced Photon Source with a 13-element high purity Ge detector as discussed in our publications.[4]

The above partial cell samples were prepared for EXAFS and XRF at the APS synchrotron source. Conventional cells were chosen for cross-sectional high resolution electron microscopy (HREM) studies in EMAL, including HRTEM, Fine Probe X-ray Energy Dispersive Spectroscopy (EDS), EDS mapping and High-Angle Annular Dark-Field (HAADF).

Since the typical scattering volume of 300 keV electrons in bulk CdTe is on the order of *microns*, in order to obtain high resolution EDS mapping, a thinning process to reduce the sample thickness down to electron transparency (typically 60-100nm) must be carried out. Sample preparation was done mostly at the University of Michigan. Details of the thinning process were discussed in our previous quarterly report (Phase III Quarter 2).

### 5.3 Voids in the CdTe and at the CdTe/CdS Interface

We collected both High-Angle Annular Dark-Field (HAADF) and scanning transmission electron microscopy bright field (STEM-BF) images on the same area of our sample as shown below in Fig. 5.1. Apparent voids show up in the 2.2  $\mu\text{m}$  thick CdTe layer as dark spots (lower average Z number for electron diffraction) in Fig. 5.1a and bright spots (lower mass density giving higher electron transmission) in Fig. 5.1b. These voids have a lateral dimension of  $\sim 0.15 \mu\text{m}$  and appear to increase slightly in density toward the back contact. This gradient is qualitatively similar to that indicated by ellipsometry but the average volume void fraction accounted for by these microscopic voids is estimated at  $\sim 3\%$  which is close to the volume void fraction,  $f_v$ , obtained from ellipsometry analysis of CdTe cells on TEC glass. (See Fig. 2.7.) Under most conditions, as-grown CdTe films on Si wafers (without  $\text{CdCl}_2$  treatment) show considerably higher void fractions by ellipsometry. (See Figs. 3.4 and 3.8.) Fig. 5.1 also shows the some voids are visible in STEM micrographs at the CdS/CdTe interface.

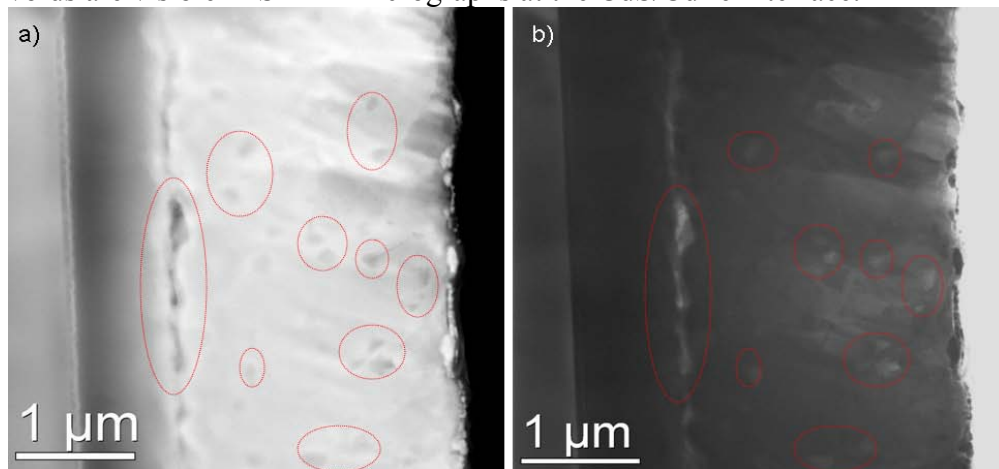


**Figure 5.1** Cross-sectional (a) HAADF and (b) STEM-BF images of standard CdTe device. Voids are circled for emphasis.

EDS elemental mappings were obtained by collecting x-ray signals from the same cross-sectional area as Fig. 5.1 to identify the distribution of the major elements in the sample from glass through TCO, CdS, CdTe to the back metal layer. The cell structure is labeled in the upper left image of Fig. 5.2 which is a tilted HAADF in low resolution. Other images are the x-ray distribution maps of Cd, Te, S, Cu and Au. EDS mapping was performed in the STEM mode with an electron beam probe size 5 Å. The dimension of the x-ray emission area is usually less than 10 times the probe size (normally 2~3 times) with this sample preparation.



The Cd and Te maps show relatively lower concentrations (dark spots as circled in Fig. 5.2) of both elements at the same locations as the dark spots in the HAADF image (Fig. 5.1a). This confirms the existence of voids in the CdTe layer. Low Cd density is also found at the CdS/CdTe interface which matches the locations of void segments in HAADF image.

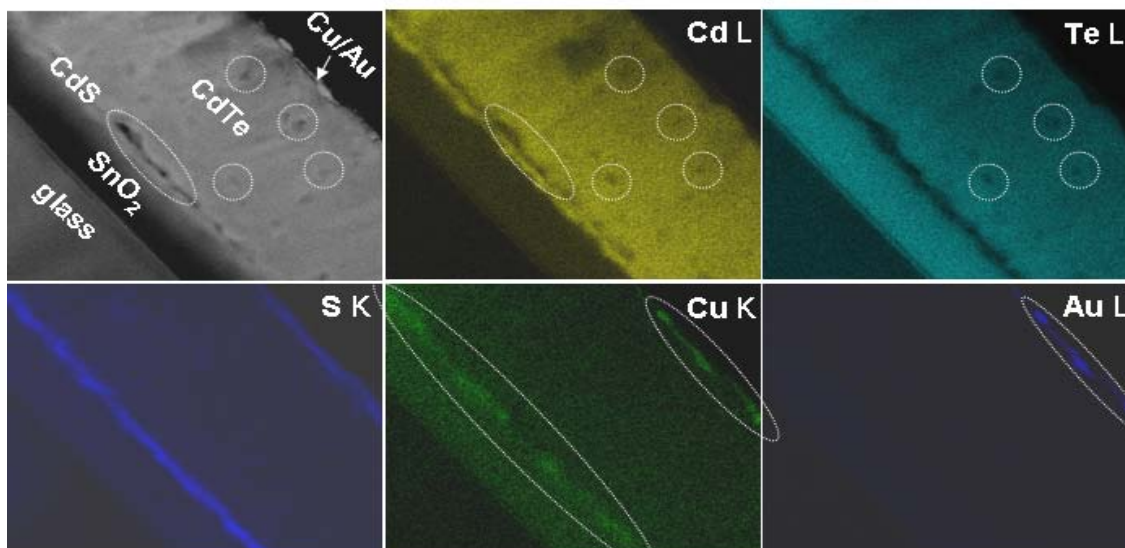


**Figure 5.2** HAADF image and EDS mapping of Cd, Te, S, Cu and Au on the same area. [The apparent Te distribution that appears in the SnO<sub>2</sub> layer is due to signal leakage of the Sn L<sub>β1</sub> (3662.8 eV) peak into the Te L<sub>α1</sub> (3769.3 eV)].

## 5.4 Cu Distribution and Cu Bonding in CdTe Cells

### 5.4.1 EDS mapping

A high concentration of Cu in the back metal contact layer (where 3.5 nm was deposited initially) is confirmed by this mapping (the two lower-right images in Fig. 5.2). Although we expected the Cu to diffuse primarily into the CdTe, Cu is found distributed throughout the Au back contact. EDS mapping in other areas from the same sample confirms similar diffusion of Cu into the Au. This indicates the possible formation of a Cu-Au alloy and is further suggested by our x-ray fluorescence and EXAFS theoretical fitting, as discussed in following sections.

Another feature clearly seen is the relatively higher concentration of Cu in the CdS layer than in CdTe. This result has been observed in SIMS studies of CdS/CdTe cells prepared by other methods.[5] We carefully compared the Cu mapping and HAADF image and found lower Cu concentration in the void segments at interface than in the CdS segments. This suggests some of the copper atoms diffuse from the back surface through the CdTe layer during back contact activation and accumulate in the CdS.

The Cu fluorescence signal from the SnO<sub>2</sub> (TCO) layer is also relatively stronger than from the CdTe layer but weaker than from CdS.

### 5.4.2 X-ray Fluorescence

The high concentration of Cu at the back contact was also observed in peeled-off metal back contact segments in x-ray fluorescence studies. In Phase I (Phase I Quarter 3 report), concurrent with our EXAFS studies at MR-CAT, we used x-ray fluorescence together with the peel-off

technique as a convenient method to determine the total amount of copper in different layers (metal or CdTe/CdS/SnO<sub>2</sub>) of the partial cell samples.

By taking advantage of the intense (*peak brilliance at 6.5keV:  $9.6 \times 10^{18}$  ph/sec/mrad<sup>2</sup>/mm<sup>2</sup> /0.1% bandwidth*) and stable x-ray beam of the APS and the high purity Ge multi-element detector of MR-CAT beamline, we were able to investigate low level Cu concentrations in our CdTe cells (typically ~0.3% averaged through the structure). Furthermore, by using an epoxy-based lift-off or peel-off process we could separate the Au layer from the CdTe (Fig. 5.3a) and independently measure the amount of Cu in the contact and in the residual structure of the partial cell.

We have measured the x-ray fluorescence excited at 10 keV, just above the Cu K-edge, to obtain maximum sensitivity to the Cu. We found the amount of Cu in the remaining structure of CdTe/CdS/glass to be much lower than in the peel-off metal/epoxy layers. As shown in Fig. 5.3a, the Cu K<sub>α</sub> intensity of the remaining structure (sample B) is ~10 % of the one of the complete partial cell (sample A), while the intensity of the peeled off metal layer (sample C) on epoxy is 90% of that of sample A. Thus, only a small portion of Cu actually diffuses into sputtered CdTe after the 45 minutes of heating at 150 °C. The ~90% of Cu peeled off with the Au/epoxy layer and our EDS mapping are evidence indicating that even after the thermal activation or diffusion process, most of the Cu actually stays at either the interface of the Au layer and CdTe film or diffuses into the Au layer. Furthermore, much of the Cu that does migrate toward the junction ends up in the CdS.

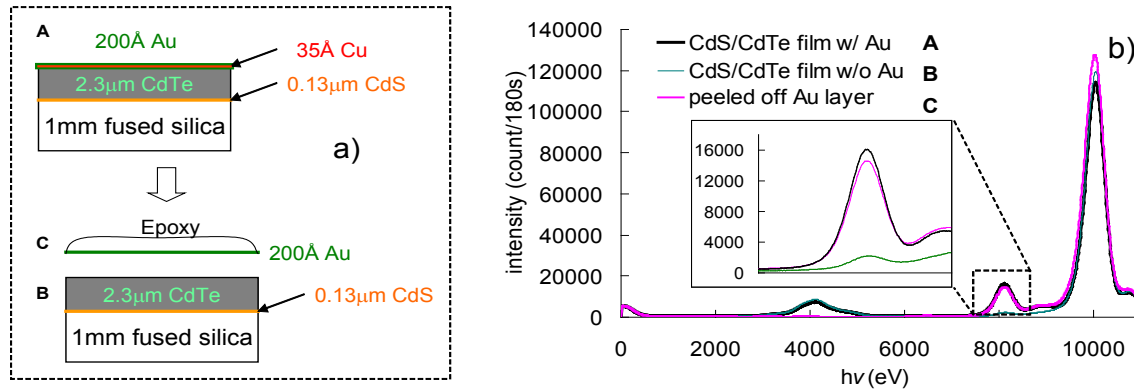


**Figure 5.3** a) the schematic structures of the samples; b) X-ray fluorescence of CdS/CdTe film with Cu/Au metal layer (A), film without metal layer (B) and the peeled off Au layer (C). Note: the peak at 8048 eV is Cu K<sub>α</sub> fluorescence generated under exposure to the 10 keV x-ray beam.

### 5.4.3 High Resolution TEM and Fine-probe EDS

A high resolution investigation into the Cu distribution in the region near the Au back contact was needed to provide better evidence of the Cu location. Such study requires nanometer scale resolution, since the evaporated Cu layer is only 3.5 nm. We have used High Resolution Transmission Microscopy (HRTEM) with point-to-point resolution of 1.7 Å together with x-ray energy dispersive spectroscopy (EDS).

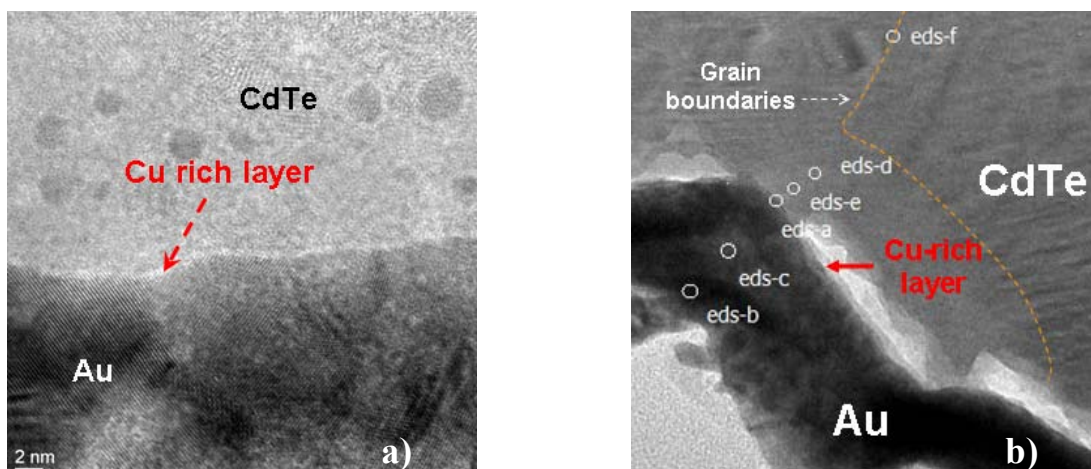


**Figure 5.4** a) High resolution TEM image at the CdTe/Au interface. b) Cross-section TEM image of CdTe and Au layer. Circles are the locations where the fine-probe EDS spectra were taken. Broken line indicates the grain boundary of CdTe.

**Table 5.1** Comparison of Cu  $K_{\alpha}$  and Mo  $K_{\alpha}$  intensities.

Position	Cu/Mo peak intensity ratio
eds-b	1.61
eds-c	1.73
<b>eds-a</b>	<b>2.24</b>
eds-e	0.32
eds-d	0.27
eds-f	0

As shown in Fig. 5.4a, cross-sectional HRTEM image demonstrates a continuous interfacial layer with thickness of approximately 4 Å (which is brighter than the CdTe and Au layers). Such interfacial layer between CdTe and Au can be observed everywhere along the interface between CdTe and Au.

Fine-probe EDS spectra from CdTe, Au and the interfacial layer confirm higher copper concentration around the CdTe/Au interface. EDS spectra (refer to Phase II Annual report for more details) across this interfacial layer were collected from positions as labelled in Fig. 5.4b. Intensity ratios of Cu and Mo  $K_{\alpha}$  peaks were compared to determine the relative Cu concentration as summarized in Table 5.1. (Mo  $K_{\alpha}$  arises from the mounting ring and is a convenient reference.)

As shown in Fig. 5.4, the spectra were collected on spots aligned along the direction of a grain boundary of CdTe. The highest Cu concentration occurs at the CdTe/Au interface (position eds-a), which confirms the interfacial layer at CdTe/Au interface (eds-a) in Fig. 5.4 is Cu-rich, with the Cu/Mo intensity ratio of 2.24. For the two positions in the Au layer (spots eds-b and eds-c), the Cu concentration is relatively lower than interface but comparable. Entering the CdTe layer, EDS indicates a sudden drop of Cu fluorescence signal to around one-tenth of that at interface for eds-e and eds-d. Increasing distance from the back contact yields weaker Cu signals. The Cu/Mo ratios of positions e and d are 0.32 and 0.27, respectively (Table 5.1). The Cu signal at position f, located at the grain boundary only 70 nm away from Au contact, is already undetectable. Thus, very little Cu appears to be located at grain boundaries.

These fine-probe EDS spectra together with the EDS mapping confirm the interdiffusion between Cu and Au layers justifying the hypothesis for our theoretical fitting of the EXAFS data, as discussed in the following section. The HRTEM and fine-probe EDS directly show the high concentration of copper at the CdTe/Au interface and in the Au layer. But any Cu above the detection limit of the fine-probe EDS mapping in the CdTe is within a region approximately 20 nm or less away from the contact/CdTe interface. There is no evidence indicating higher Cu concentrations at the CdTe grain boundary than in the grain interiors.

#### 5.4.4 EXAFS

Besides the high concentration of Cu as observed at the interface of CdTe and Au and inside the Au layer, investigation of local structure and chemical bonding of copper atoms in complete cell structures through EXAFS analysis is helpful to understand the role of copper at the back contact.

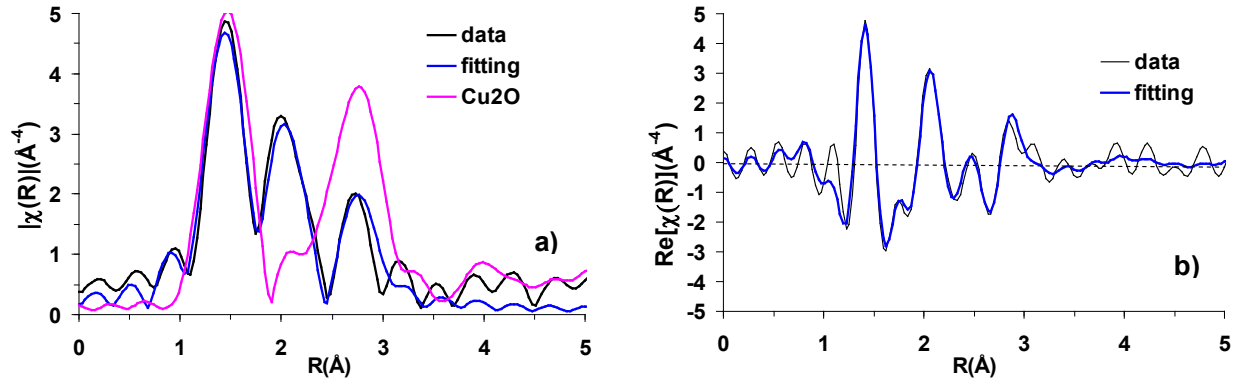


**Figure 5.5** a) Phase-uncorrected  $\chi(R)$  functions of semi-cell structure sample and theoretical fitting compared with  $\text{Cu}_2\text{O}$  reference; b) the real part of  $\chi(R)$  functions of experiment data and theoretical fitting. (Imaginary parts of the  $\chi(R)$  function are not)

**Table 5.2** Theoretical fitting parameters of EXAFS spectra of partial cell structure and  $\text{Cu}_2\text{O}$  reference.

bond Scattering	N	$\Delta N$ (+/-)	R(Å)	$\Delta R(\pm)$	$\sigma^2$ (10 <sup>-3</sup> Å)	$\Delta\sigma^2(\pm 10^{-3}\text{Å})$	$\Delta E_o$ (eV)
Semi cell structure without TCO (SiO2:Al/0.13 μm CdS/ 2.3 μm CdTe/35 Å Cu/ 200 Å Au)							
Cu-O(Cu2O)	1.4	0.3	1.84	0.02	1.6	fixed	-3.07 ± 4.09
Cu-Au(CuAu)	11.9	3.0	2.59	0.06	21.1	8.2	
Cu-Cu(CuAu)	0.9	0.22	2.63	0.11	11.7	12.6	
Cu2O							
Cu-O(Cu2O)	1.5	0.39	1.84	0.004	1.6	0.9	8.31± 0.32
Cu-Cu(Cu2O)	20.1	5.12	3.04	0.01	27.6	1.5	

Our EXAFS data on the partial cell structure samples indicates a strong peak arising from the first nearest neighbor - oxygen atom shell located at the same position  $-1.43 \text{\AA}$  in  $|\chi(R)|$  spectrum as the peak of the first nearest neighbor bond (Cu-O) in  $\text{Cu}_2\text{O}$  (Fig. 5a). The peak width is different from that of  $\text{Cu}_2\text{O}$ , but the real and imaginary parts of the  $\chi(R)$  function in the region

from 1.2 Å through 1.7 Å indicate this narrowing is due to scattering intensity leakage from the other two peaks at 2.0 Å and 2.73 Å. This suggests that most of the copper in the complete cell forms a copper oxide structure, which is consistent with our earlier work on Cu-diffused, CdCl<sub>2</sub>-treated CdTe film. [6]

These two peaks at 2.0 Å and 2.73 Å are also not generated from scattering by sulphur, tellurium (as in Cu<sub>2</sub>Te), chlorine (as in CuCl or CuCl<sub>2</sub>), or copper (as in metal Cu crystal) neighbors. But given the small amount of Cu in the sample and the finite sensitivity of the x-ray detector, we cannot conclude that Cu<sub>2</sub>S and Cu<sub>2</sub>Te do not exist in the cell at low levels. What appear in the EXAFS spectra in this case should be the dominant chemical phases of copper in the samples. These are Cu<sub>2</sub>O and Cu-Au as discussed below.

Model fitting to the two EXAFS peaks was informed by our EDS mapping, x-ray fluorescence study of peeled-off Au contact layers, HREM images and fine-probe EDS as discussed in previous sections. Scattering paths of Cu-Au and Cu-Cu from a model structure of the ordered 50:50 Cu-Au alloy are fitted to the spectrum together with the Cu-O path from a Cu<sub>2</sub>O reference; the result of which is shown in Fig. 5.5. Our fitting gives the Cu-Au and Cu-Cu path lengths of 2.59 Å and 2.63 Å, respectively (Table 5.2). The coordination number of the Au and Cu neighbor shell provided in the theoretical fitting is 11.9 and 0.9, respectively. The copper atoms may locate at the grain boundary of the Au grains or defects of Au crystal.

Given the theoretical fitting results of EXAFS data from the partial cell structures and the Z contrast of the HREM images at the CdTe/Au interface, we consider it most likely that the interfacial Cu-rich layer should be a copper-oxide layer with approximate thickness of 4Å. Since the Cu-O and Cu-Cu bond lengths in Cu<sub>2</sub>O are 1.84 Å and 3.04 Å (Table 5.2), respectively, such a presumed 4 Å Cu<sub>2</sub>O layer is so thin that not more than two Cu-O layers could be formed in this layer. This explains the absence of Cu-Cu bonds in our EXAFS spectra.

## 5.5 S at CdTe Back Contact (EDS and XES Studies)

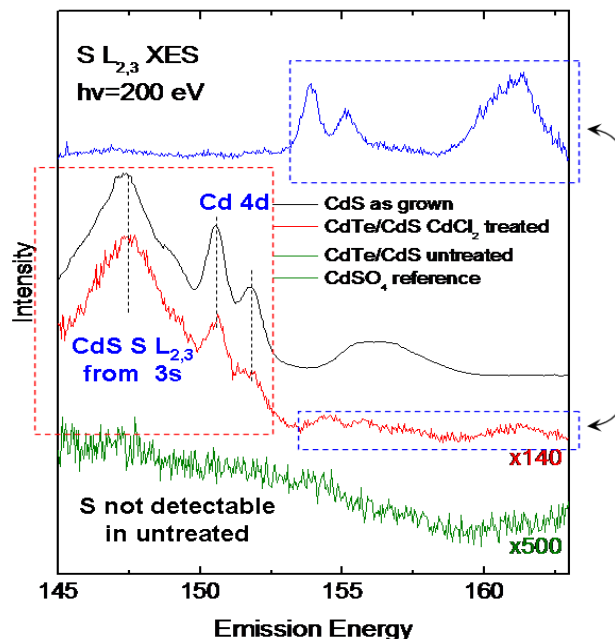
Another significant feature indicated by the EDS mapping is the presence of some sulfur at the back surface of the CdTe (See Fig. 5.2). The EDS map shows the S at the CdS layer, but there is also a significant increase in sulfur at the back of the cell at the interface between the CdTe and Cu/Au. The thickness of the high sulfur concentration layer at the back surface is approximately 100nm. The sulfur concentration in this layer is much lower than in CdS but higher than in CdTe and SnO<sub>2</sub> as indicated by the qualitative differences in brightness.

The chemical form of this interfacial sulfur at CdTe/back contact, was studied in collaboration with Lothar Weinhardt and Clemens Heske at the University of Nevada, Las Vegas using X-ray Emission Spectroscopy (XES) at the Advanced Light Source, Lawrence Berkeley National Lab. They used our standard sputtered CdS/CdTe films (0.13µm and 2.3µm, respectively) on TEC-7 together with an as-grown CdS film (1.8µm) on fused silica. CdTe/CdS films both with and without standard vapor CdCl<sub>2</sub> treatment were studied. Sulfur 2p core holes are generated by the x-ray beam with energy of 200 eV, which has an attenuation length in CdTe of 257nm (Model available at <http://www-cxro.lbl.gov/>).

Fig. 5.6 shows the S L<sub>2,3</sub> spectra for as-grown and chloride-treated CdTe/CdS films, an as-grown CdS film, and a CdSO<sub>4</sub> reference. While no S can be detected on the CdTe surface of the untreated CdTe/CdS/TEC-7 sample (probe depth ~250 nm), we find a clear S L<sub>2,3</sub> signal in the range from 145 eV through 153 eV for the CdCl<sub>2</sub> treated sample, namely a dominant peak from S 3s states at approximately 148 eV and two sharp peaks just above 150 eV corresponding

to the Cd 4d-derived bands. This signal is primarily comprised of CdS-like sulfur, as well as some sulfur in an oxidized (sulfate) environment. This can be seen by comparing the difference spectrum with a CdSO<sub>4</sub> reference in the energy range from 153 eV through 167 eV with 140 times intensification on the spectrum of the chloride-treated sample.

**Figure 5.6** Sulfur L<sub>2,3</sub> XES spectra of as-grown CdS reference, as-grown and CdCl<sub>2</sub> treated CdTe/CdS, and a CdSO<sub>4</sub> (sulfate) reference. The spectrum of CdCl<sub>2</sub> treated CdTe/CdS is primarily comprised of CdS-like sulfur below 153 eV and sulfate-like sulfur above 153 eV.



As a conclusion of our EDS mapping of sulfur and XES surface state study, the CdCl<sub>2</sub> treatment apparently leads to S diffusion and accumulation at the back surface of CdTe and some of the diffused sulfur is oxidized to form a sulfate. We suggest this CdSO<sub>4</sub> can stabilize the higher concentration of S at the back contact compared with the bulk of the CdTe film.

## 5.6 Conclusions

This work using EDS mapping, XRF, HRTEM together with fine-probe EDS provides direct evidence of Cu redistribution in conventional sputtered CdS/CdTe cell structures (that have received CdCl<sub>2</sub> activation treatments). Approximately 90% of the 35 Å of deposited Cu remains at the back contact after the standard fabrication process, including CdCl<sub>2</sub> treatment. Some of the Cu at the back contact forms a subnanometer copper-rich layer at the CdTe/Au interface. The rest of the Cu at the back contact diffuses into the Au layer. The remaining ~10% of the deposited Cu ends up mostly in the CdS.

Our EXAFS modeling suggests that the subnanometer copper-rich layer at the CdTe/Au interface has the bonding arrangement of Cu<sub>2</sub>O, at least for sputtered cells prepared with vapor CdCl<sub>2</sub> activation (with no post-chloride etching) before evaporation of Cu and Au. Such a cuprous-oxide layer may serve to limit some diffusion of copper into the CdTe layer, although it is clear that some Cu does migrate into the CdS.



## 6. Potential Distribution During Magnetron Sputtering Deposition

### 6.1 Introduction

In the progress report for the Second Quarter of Phase 3 we presented the results of the potential distribution during magnetron sputtering. The Langmuir probe, made of a 10 mm long, 70 micron diameter Pt wire, was placed in front of the center of the substrate 10 mm towards the CdTe target. 10 mm of wire protruded with the rest of the wire isolated from the plasma by the glass capillary tube and fed through the chamber wall for easy readout. We used a Keithley 2400 SourceMeter to collect the I-V data. Two other feedthroughs were used for the substrate bias wire and target self-bias wire. The substrate holder was isolated from the chamber walls with a dielectric piece and normally during the deposition the substrate potential was floating. The setup shown on the Fig. 6.1 allowed us to measure the self-bias potential of the substrate as well as to apply a desired bias over the range of -50 to 50 V in order to check on the corresponding changes in plasma potential.

In order to cover the most useful region in the phase space of deposition parameters we performed all the measurements for the Ar pressure range of 5 mTorr to 50 mTorr and RF power of 5 W to 60 W. In addition, data were taken in two different configurations: with a freshly cleaned ground shroud (bare metal) and a ground shroud with a thick CdTe coating, equivalent to the coating that is normally built up after about 200 hours of deposition.

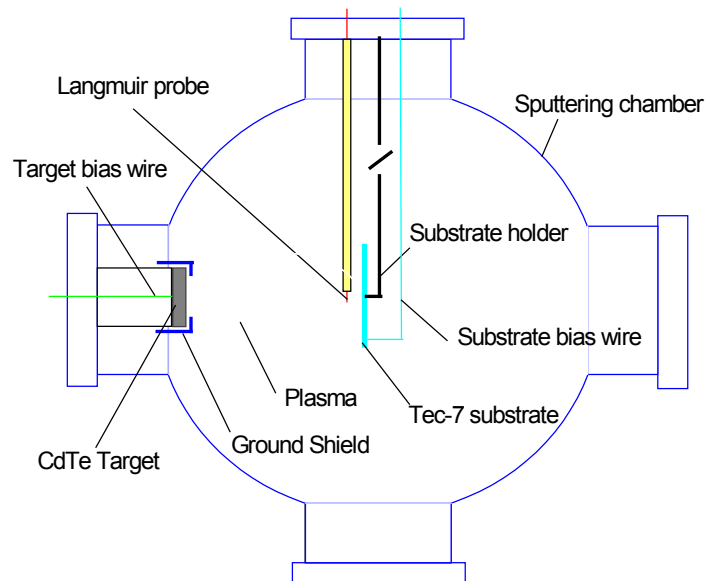


**Figure 6.1 Experimental setup for potential distribution and the Langmuir probe measurements.**

Below is a brief summary of the results with some important conclusions.

## 6.2 Cathode DC Bias

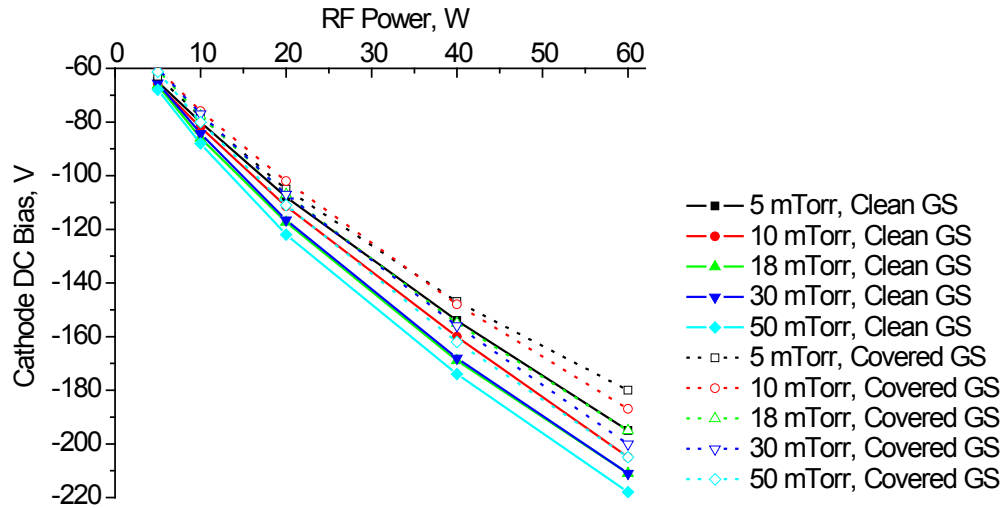


**Figure 6.2 Cathode DC bias as a function of pressure and RF power. Clean ground shroud (dotted lines) and coated ground shroud (solid lines).**

The dependence of target dc self-bias on pressure is rather weak while it steadily becomes more and more negative when the RF power increases (Fig. 6.2). Also there is a noticeable difference between clean and covered ground shroud conditions – the cathode DC bias is always less negative for the same pressure and power conditions when the ground shroud is covered with an insulating coating of CdTe.

## 6.3 Substrate Self-Bias

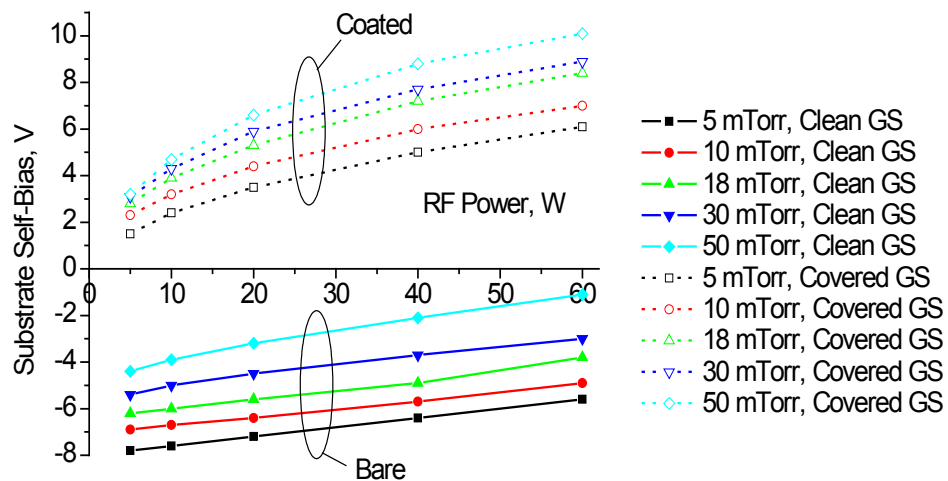


**Figure 6.3 Substrate self-bias bias as a function of pressure and RF power. Clean ground shroud (dotted lines) and coated ground shroud (solid lines)**

Our standard deposition configuration maintains the substrate at floating bias that changes with both pressure and RF power as shown on the Fig. 6.3. It becomes more positive (or less



negative in some cases) when both pressure and power increase. We found the largest differences between the cases of clean and coated ground shroud. For the case of a clean ground shroud the substrate is always found under negative self-bias while it eventually becomes positive when enough CdTe coating is developed on the shroud. We believe this behavior can explain the observed change in pinhole density – extremely high right after the cleaning of the ground shroud and diminishing as the total deposition hours increases. Higher pinhole production can be explained by the presence of positively charged dust particles inside the chamber that get attracted to the substrate when its substrate self bias potential is negative but otherwise do not cause a problem.

#### 6.4 Plasma Potential

We found a very weak dependence of plasma potential on the RF power with a tendency to increase with increasing power. The plasma potential is independent of pressure within the experimental error (Fig. 6.4). The largest change in plasma potential observed was between the cases of coated and clean ground shrouds. The plasma potential is about 5 V higher in the case of the of the coated ground shroud.

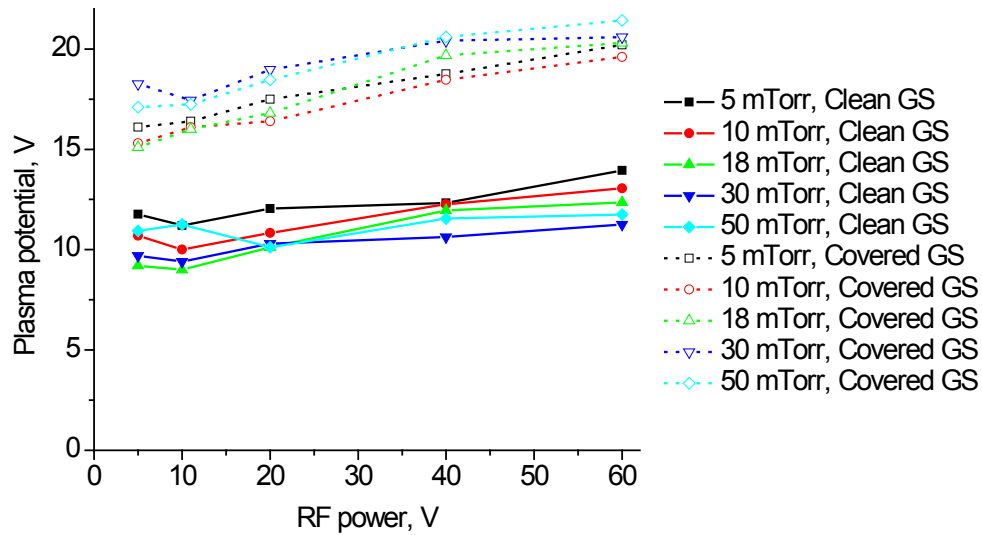


**Figure 6.4** Plasma potential as a function of pressure and RF power. Clean ground shroud (dotted lines) and coated ground shroud (solids).

#### 6.5 Conclusions

We measured the dc cathode bias, substrate self bias and plasma potential as functions of sputter gas pressure and applied RF power. We found a substantial difference between conditions resulting from using a freshly cleaned ground shroud vs. one that had been in the chamber for about 100 hours of deposition.

This explains the reduction of the deposition rate that is observed as the CdTe coating on the ground shroud builds up. A coated ground shroud results in a smaller potential difference between the plasma and the target DC bias that results in less integrated sputtering time over each RF cycle. This also relates to the higher pinhole density right after the cleaning of the

ground shroud, since the ground shroud cleaning procedure leads to the decrease of the substrate self bias by roughly 10 V which is enough to make it slightly negatively biased as opposed to the positive self bias which we believe is typical for the major part of the target maintenance cycle.

As a result of this study we extended our typical 100 deposition hour ground shroud cleaning cycle by 5 times and no negative effects were observed other than a decrease of the deposition rate that can be compensated by increasing the RF power or using lower pressure sputtering conditions. High quality films with very low pinhole density yielding above 13% efficiency cells have been deposited under these conditions on commercial soda-lime glass.

## 7. Ultra-Thin Devices

Earlier in this phase we reported our studies on ultra-thin (about 0.5 micron CdTe) cells. Even though an efficiency of 10% was achieved for these devices, the cells still suffered significantly from losses in all three important figures of merit (i.e.  $J_{SC}$ ,  $V_{OC}$  and FF). While a loss in  $J_{SC}$  with thin CdTe is fairly well understood as arising mainly from deep penetration loss in the IR part of the spectrum), losses in  $V_{OC}$  and FF are more complex. These two parameters can be affected in general by six variables. Three are briefly summarized: 1) the presence of an HRT layer, 2) the CdS thickness, and 3) the CdTe thickness. Four variables are independently discussed in subsequent sections: 4) the  $CdCl_2$  treatment parameters, 5) the amount of copper used in the back contact, and 6) the duration/temperature of the final back contact diffusion. Finally, in Section 7.7 performance statistics are presented for optimized cells.

### 7.1 Presence of an HRT Layer

It has been shown previously that adding an HRT layer between the CdS and the conventional high conductivity  $SnO_2:F$  coated glass is beneficial, especially for cells with thin (below 80 nm) CdS layers. Our study of the effect of an HRT layer was discussed in our Phase 3, Quarter 4 report. In general the HRT layer allows thinner CdS with higher current and less loss in  $V_{OC}$  which typically happens with CdS layers below 80 nm.

### 7.2 CdS Thickness

We reported on the optimum thicknesses of the CdS layer for cells deposited on both bare Tec-15 (about 80 nm) and HRT-coated Tec-15 (about 45 nm). In this study we kept the CdS layer thickness close to 60 nm for all of the samples independent of the CdTe thickness. This approach has likely decreased the maximum efficiency due to a slight loss in  $J_{SC}$  caused by the excessive absorption in CdS, but on the other hand gave us an extra assurance that the n-side of the photovoltaic junction is robust and not likely to influence the observed  $V_{OC}$  and FF changes.

### 7.3 CdTe Thickness

We prepared a set of samples with the following CdTe thicknesses: 0.38  $\mu m$ , 0.5  $\mu m$ , 0.65  $\mu m$ , 0.8  $\mu m$ , 1.1  $\mu m$ , 1.45  $\mu m$ , 1.85  $\mu m$ , 2.2  $\mu m$  and 2.6  $\mu m$ . Thickness was measured by a DEKTAK profilometer and represents a mean thickness of the sample averaged over 35 small area (0.062  $cm^2$ ) cells on each sample (a quarter piece of our typical 3"x3" substrate). We will specifically identify this gradient from center to edge where appropriate. All samples were deposited at 18 mTorr of Ar pressure with 20 W of applied RF power.

### 7.4 $CdCl_2$ Treatment

We have observed previously some dependence of cell parameters on all the variables associated with  $CdCl_2$  treatment such as the treatment type (vapor or wet), treatment temperature and treatment duration. In this study we used a wet treatment meaning that a room temperature saturated  $CdCl_2$ -methanol solution was applied directly to the CdTe surface and allowed to dry forming a relatively uniform coating on the sample. After the samples were dried, they were annealed in dry air for variable times with a temperature profile that reached 387 °C. A typical temperature profile for the treatment is shown in Fig. 7.1. The flat regions of the two curves

represent the nominal treatment time as it would be entered into the computer program that controls the system. In reality the cells undergo some treatment during the ramp-up and ramp-down time as well (Fig. 7.2). The total amount of treatment that the sample receives is an integral value of both and can be represented as the area below the curve if the Arrhenius-like behavior of the different process that form a core of  $\text{CdCl}_2$  treatment is also taken into account. Fig. 7.3 represents the temperature dependence of bulk diffusion coefficients for Cd and Cl –and the grain boundary diffusion coefficient for Cd. Cd (bulk and GB) self-diffusion coefficient are taken from [7] and  $D_{\text{CL(BULK)}}$  is taken from [8]. From data of Fig. 7.3 and Fig. 7.4 one can estimate a relative contribution of the treatment during the ramp-up and ramp-down time to the entire treatment and adjust to a nominal treatment time with a step function temperature-time profile. Fig. 7.5 shows the values for three different processes for a 30 minute treatment and Fig. 7.6 – for a three-minute one. This estimation should not be taken as a full quantitative analysis but we believe that it gives useful guidelines for choosing  $\text{CdCl}_2$  treatment times for the cells with different CdTe thicknesses.

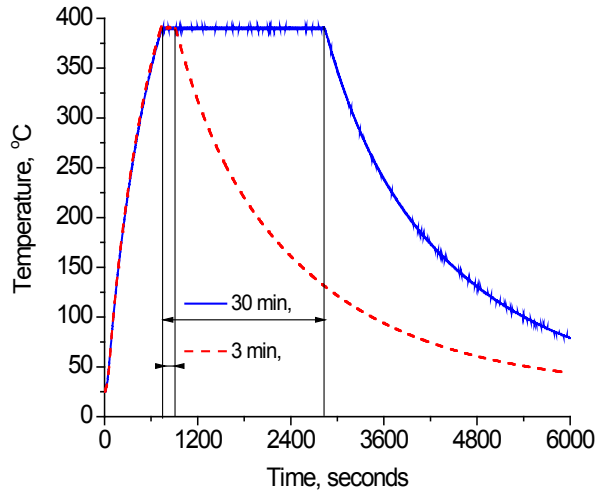


**Figure 7.1**  $\text{CdCl}_2$  treatment temperature profiles for nominal 3 minute and 30 minute treatment times.

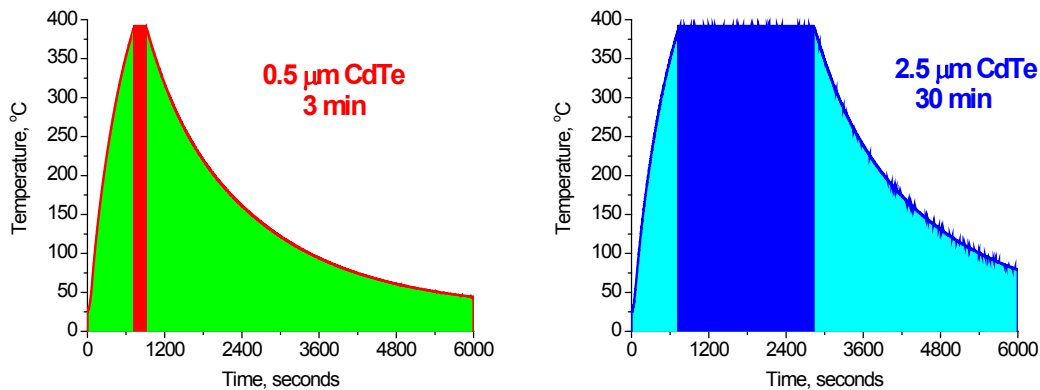


**Figure 7.2** A schematic representation of “nominal” (square areas on the graphs) vs. “actual” (the whole area under the curve) treatment time.

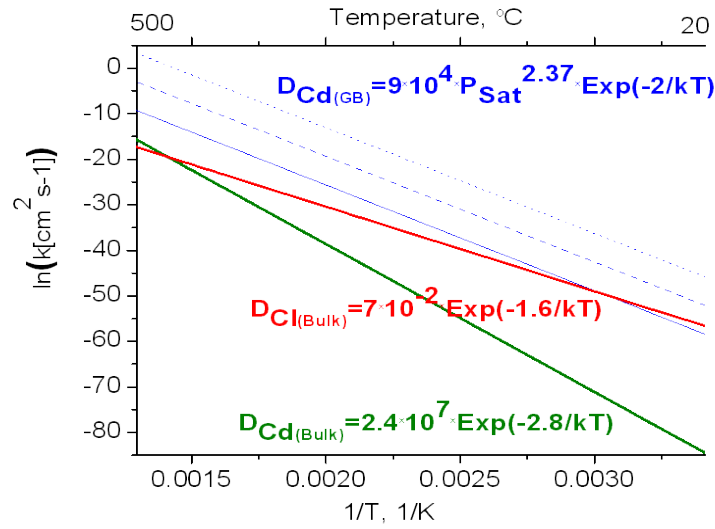


**Figure 7.3** Arrhenius plots of diffusion coefficients for Cl in bulk CdTe ( $D_{Cl(Bulk)}$  - red), Cd self-diffusion in bulk CdTe ( $D_{Cd(Bulk)}$  - green), and Cd diffusion along grain boundaries in CdTe ( $D_{Cd(GB)}$  - blue). The three different curves are for 1 mTorr (solid), 10 mTorr (dashed) and 100 mTorr (dotted) partial pressures of  $CdCl_2$

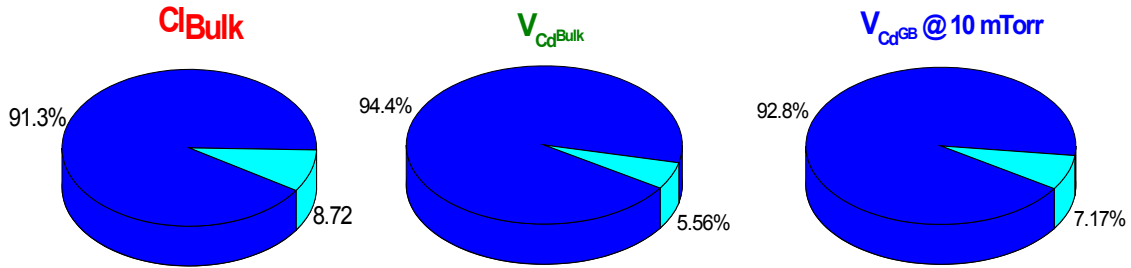


**Figure 7.4** Relative contribution of the ramp-up and ramp-down time (light blue segment) calculated for the three different processes from the Fig. 7.3 for the case of a 30-minute treatment at 387 °C

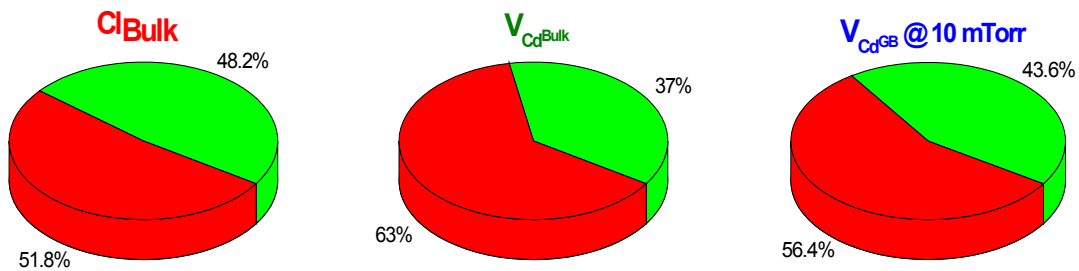


**Figure 7.5** Relative contribution of the ramp-up plus ramp-down time (green segment) calculated for the three different processes from the Fig. 7.3 for the case of a three-minute treatment at 387 °C

As an example of this correction for ramp-up and ramp-down, we can reanalyze our previously established benchmarks that are proven to give reasonably good results in terms of cell performance (Table 7.1 – “nominal” treatment time column). If treatment time is plotted against CdTe thickness (Fig. 7.6, open squares) it does not intercept the origin, while if you consider the ramp-up plus ramp-down contribution to be equivalent to approximately 3 minutes of treatment at constant temperature (387 °C) (see Fig. 7.6) and correct the time correspondingly (“actual” treatment time in the Table 7.1) then the results can be easily approximated by a straight line passing through the origin (Fig. 7.6).

**Table 7.1 Benchmarks for CdCl<sub>2</sub> treatment time of the samples with different CdTe thickness and corresponding best cell efficiency**

<b>CdTe Thickness</b>	<b>CdCl<sub>2</sub> treatment time (nominal)</b>	<b>CdCl<sub>2</sub> treatment time (actual)</b>	<b>Best cell efficiency</b>
2.5	30	33	14%
2.25	25	28	13.7%
1.32	15	18	11%
0.97	10	13	12%
0.75	5	8	8%
0.5	3	6	10%
0.3	1	4	6 %

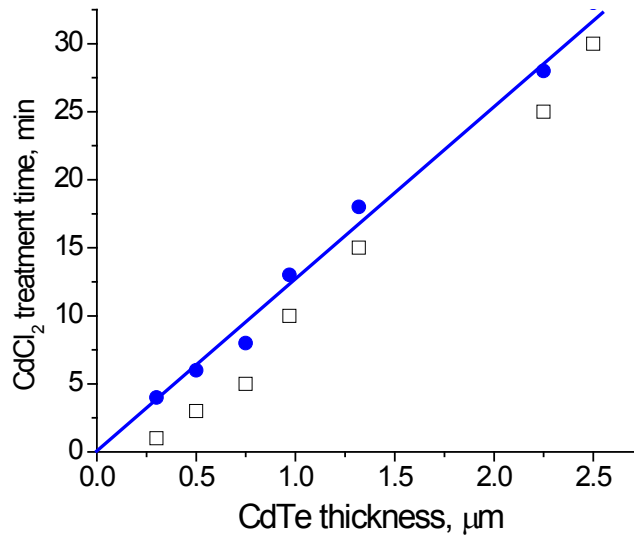


**Figure 7.6 CdCl<sub>2</sub> treatment time (“nominal” – open squares and “actual” - blue dots) vs. CdTe thickness and the linear fit for the “actual” time.**

In order to test this hypothesis we prepared a set of samples with different CdTe thicknesses as described above and treated them with times that would approximately follow the straight line from the Fig. 7.6 but with a small variation such that each sample of a certain thickness was treated for two different times closely spaced along the time axis. Fig. 7.7 illustrates this

approach. Two separate sets of values at the time axis correspond to “nominal” and “actual” treatment time.

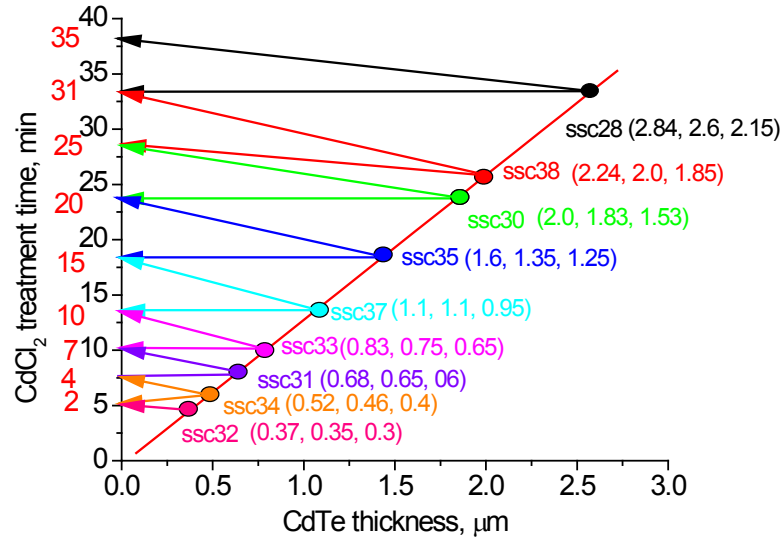


**Figure 7.7** Treatment time chosen for samples of different thickness. Arrows indicate the two different treatment time chosen. Values on the time axis are “actual (black) and “nominal” (red) treatment time.

## 7.5 Thickness of the As-Deposited Cu Layer

UT’s typical Cu/Au back contact deposited by thermal evaporation was used in this study. Since we have previously found some dependence of cell efficiency on the as-deposited Cu layer thickness as the CdTe thickness is changed, this parameter was included into the study in addition to the CdCl<sub>2</sub> treatment time variation. As described before, two sister quarter pieces from each sample of a certain thickness were treated for a longer time than the two others. After that, one sample with a longer treatment time was completed with a back contact having a Cu layer thinner than the other one. Samples with shorter CdCl<sub>2</sub> treatment time were processed similarly (Fig. 7.9). For the samples with CdTe layer thicker than 1.5 micron, 10 Å Cu / 200 Å Au and 30 Å Cu / 200 Å Au back contacts were used and for the thinner ones the 10 Å Cu / 200 Å Au and 20 Å Cu / 200 Å Au combination was chosen. See Table 7.2 for detailed information about each sample.

Shorter CdCl <sub>2</sub> Thicker Cu	Shorter CdCl <sub>2</sub> Thinner Cu
Longer CdCl <sub>2</sub> Thicker Cu	Longer CdCl <sub>2</sub> Thinner Cu

**Figure 7.8** A typical sample used in this study. Each quarter-piece receives a certain combination of CdCl<sub>2</sub> treatment and back contact.

## 7.6 Cu Diffusion Time

Again, our previous experience suggests that Cu diffusion time should progressively get shorter as the thickness of the CdTe layer decreases. We are yet to determine the optimum conditions for all the different thicknesses of CdTe, especially on the thinnest side of the series presented here, but we followed our previous benchmarks that were proven to be useful (see Table 7.2 for more information).

## 7.7 Cell Performance Statistics for Optimized Cells

Finally in this section, we present performance statistics ( $V_{OC}$ ,  $J_{SC}$ , and FF) for cells optimized over the various parameters discussed above.



**Table 7.2 Sample Fabrication Details**

Sample ID		Substrate	CdS, nm	CdTe, μm	CdCl <sub>2</sub> treatment, min		Cu, Å	Au, Å	Cu diff, min			
					minimal	actual						
SSC28	A	HRT Tec 15	60	2.84, 2.5, 2.15	35	38	10	200	45			
	B						30					
	C				31	34	10					
	D						30					
SSC38	A			2.24, 2.0, 1.85			25			28	10	30
	B										30	
	C				10							
	D				30							
SSC30	A			2.0, 1.83, 1.53	20	23	10			30		
	B						30					
	C						10					
	D						30					
SSC35	A			1.6, 1.35, 1.25	15	18	10		30			
	B						20					
	C						10					
	D						20					
SSC37	A			1.1, 1.1, 0,95	10	13	10			20		
	B						20					
	C						10					
	D						20					
SSC33	A			0.83. 0.75, 0.65	7	10	10		15			
	B						20					
	C						10					
	D						20					
SSC31	A			0.68, 0.65, 0.6	4	7	10			10		
	B						20					
	C						10					
	D						20					
SSC34	A			0.52, 0.46, 0.4	2	5	10		7			
	B						20					
	D						10					
	C						20					
SSC32	B			0.37, 0.35, 0.3			10			5		
	A						20					

The back contact area of  $0.062 \text{ cm}^2$  was defined by a mask with 35 dots per quarter piece sample as pictured in Fig. 7.10. Individual cells are indexed in such a way that cells with smaller numbers are closer to the middle of the sample and the larger number is closer to the outer regions. Since our cells normally have a thickness gradient from the center to the edge as reflected in the CdTe thickness column in the Table 7.2 (three values correspond to the thickness

measured close to the cells # 1, # 9 and # 25 correspondingly) this sometimes provides valuable information about fine structure in the variance of the cell performance vs. CdTe thickness.

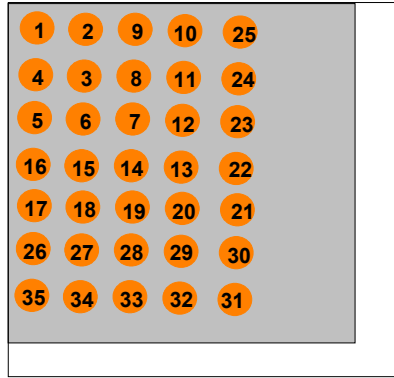


**Figure 7.9** A sketch of a sample with individual dot cells. Numeration starts from the center of the piece and dot cells with lower numbers typically have slightly thicker CdS and CdTe layers.

Typically we report statistical results for the whole ensemble of 35 cells for each sample, but in this particular case we had to take a different approach. This is a consequence of an unusually large pinhole density in all the samples regardless of CdTe thickness. (We recently found the high pinhole density was a result of a particular step in our sample handling procedure that has now been changed. Although normally we keep our samples in plastic boxes without anything being in contact with the film, in this case they were stored in polyethylene bags that proved to be detrimental for the cells. We have observed pinholes appearance after the sample has been stored in the bag even for a short period of time. Electrostatic interactions between the plastic and the sample surface is the plausible cause, but further investigation is needed.

As a result of film damage presumably caused by the plastic bags, the statistics for 35 cells ended up being greatly affected and not representative of a proper fabrication process. Therefore we had to restrict our analysis to the best 10 out of 35 cells on the each sample. We believe that this approach is more appropriate in this particular case and the results presented below nicely represent the CdTe thickness dependence that was actually sought.

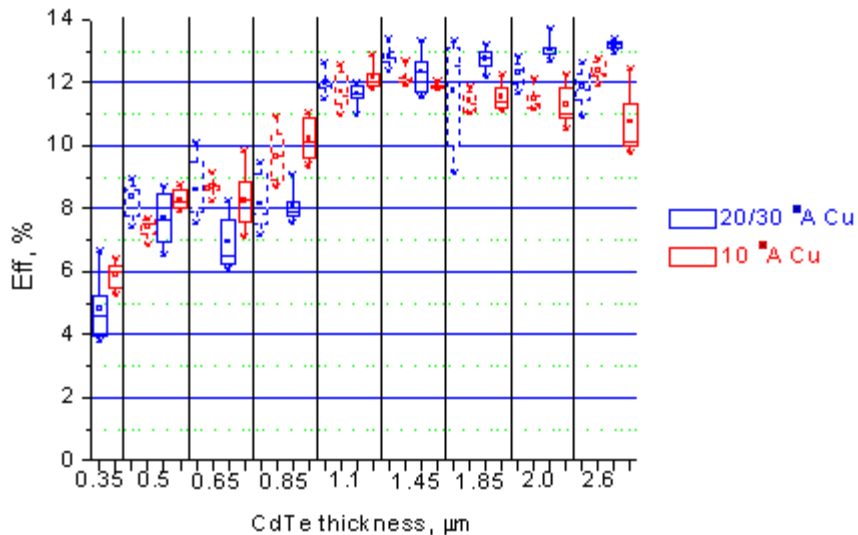


**Figure 7.10** Box-and-whiskers plot of the efficiency of the 10 best cells from each sample

Fig. 7.10 represents the efficiency dependence on CdTe thickness. Following the recipes presented in the Table 7.2 we have been able to fabricate cells with an average efficiency greater than 12 % for all the thicknesses above 1  $\mu\text{m}$ . It looks from our data that this thickness represents the first tipping point below which a significant efficiency drop is observed. The second critical value appears to be around 0.5  $\mu\text{m}$  below which a more rapid efficiency drop begins. It also can be seen from the figure that variations in as-deposited Cu (red vs. blue symbols) have a stronger effect on efficiency than variations in  $\text{CdCl}_2$  treatment time (solid vs. dashed).

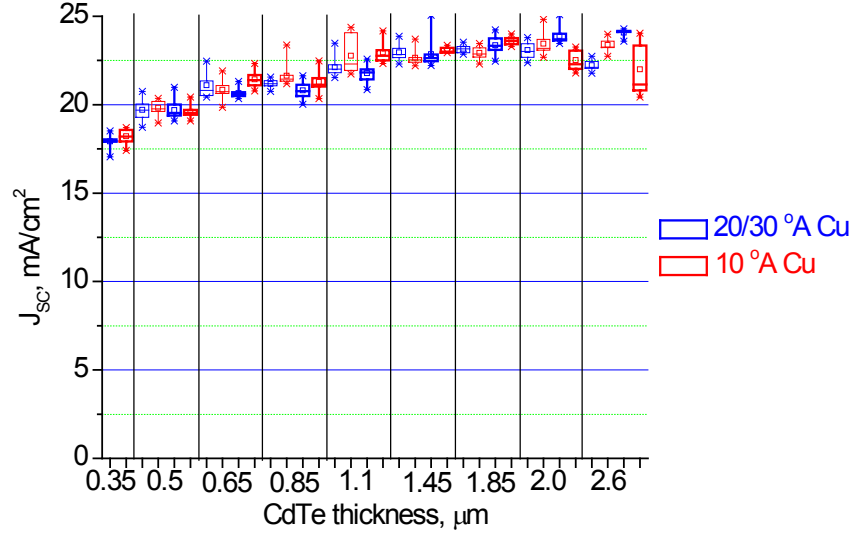


**Figure 7.11 Short-circuit current of the 10 best cells from each sample**

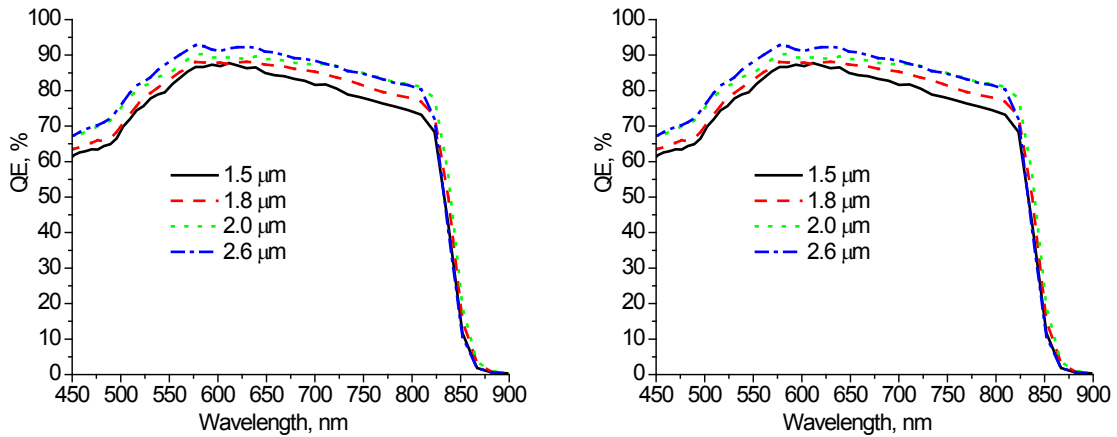


**Figure 7.12 Quantum efficiency at zero bias conditions**

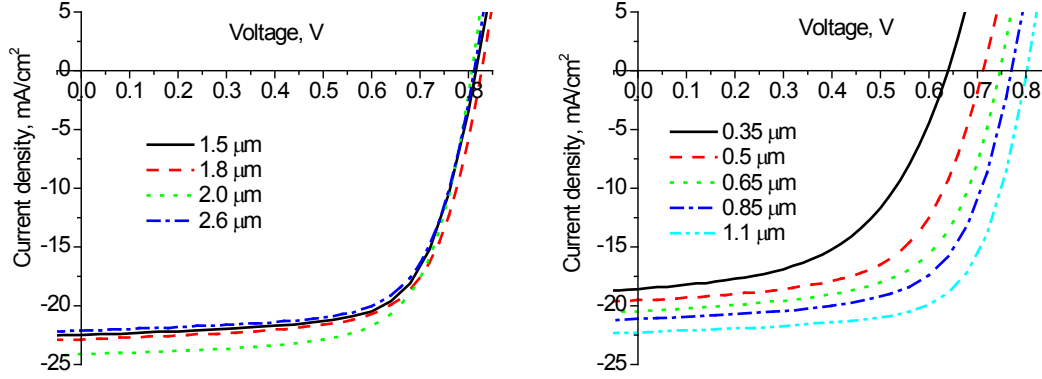


**Figure 7.13 J-V characteristics of the cells from the Figure 7.11.**

Fig. 7.11, Fig. 7.13 and Fig. 7.14 represent the second order metric for the same sets of cells. Short-circuit current (Fig. 7.11) starts to decrease slightly when the thickness of CdTe layer is less than one micron due to deep penetration loss first and the more dramatically due to weaker collection which appears to be wavelength independent as can be seen from the QE graphs in Fig. 7.12. On top of that there are slight variations in transmission of the CdS layer that can be attributed either to the position of the cell on the sample (CdS thickness gradient, similar to that of CdTe), or nominal as-deposited CdS thickness fluctuations from sample to sample, or amount of CdTe consumed by interdiffusion during the CdCl<sub>2</sub> treatment process.

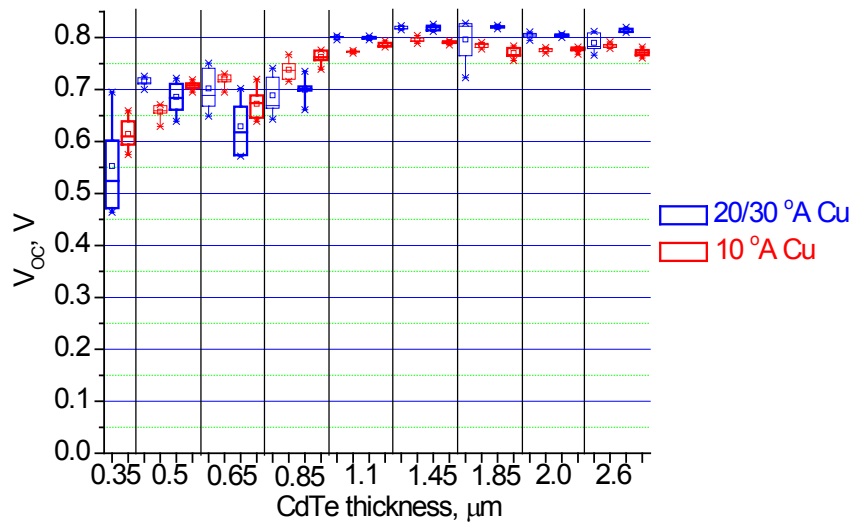


**Figure 7.14 Open-circuit voltage of the 10 best cells from each sample.**

Open-circuit voltage (Fig. 7.14) follows approximately the same dependence on CdTe thickness as does  $J_{SC}$  – remaining virtually the same for all the samples thicker than one micron and gradually decreasing for the thinner ones. This is consistent with the collection problems of

the thin samples observed in  $J_{SC}$  graphs before. One interesting observation is the prominent effect of Cu on the cells with thicker CdTe layers (one micron and above) - an additional 20 Å of as-deposited Cu can increase the average  $V_{OC}$  by as much as 50 mV in some cases (1.85 micron sample on the Fig. 7.14). A similar dependence was observed in the fill factor as well (Fig. 7.15).

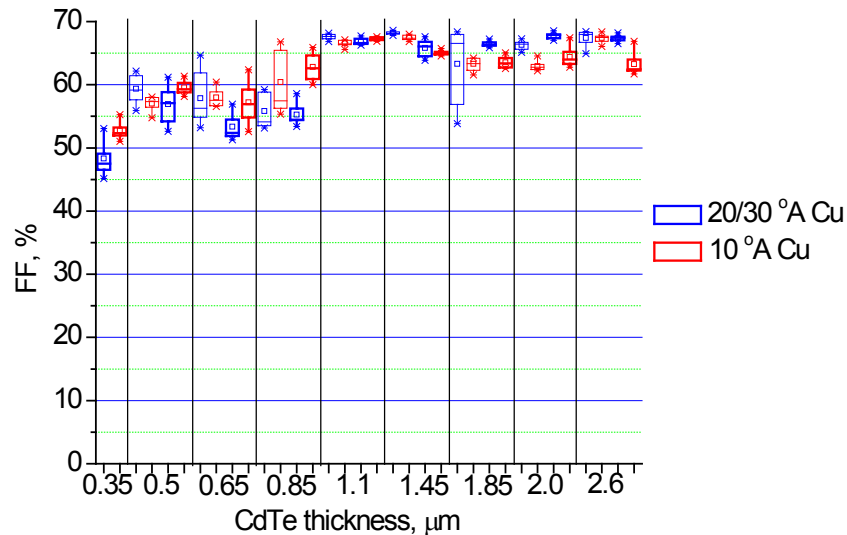


**Figure 7.15** Fill factor of the 10 best cells from each sample.

We obtained bias-dependent QE measurements on one of the best samples from each thickness point to investigate further the issue of carrier collection. It is remarkable that there is virtually no difference between the QE curve taken at zero bias and at reverse bias (-0.5 V and -1 V) for all the samples with CdTe layer thicker than 1 micron. There is also a very little change in the overall QE shape except for a slight hint of deep penetration loss (Fig. 7.16 and the top left graph on the Fig. 7.17).

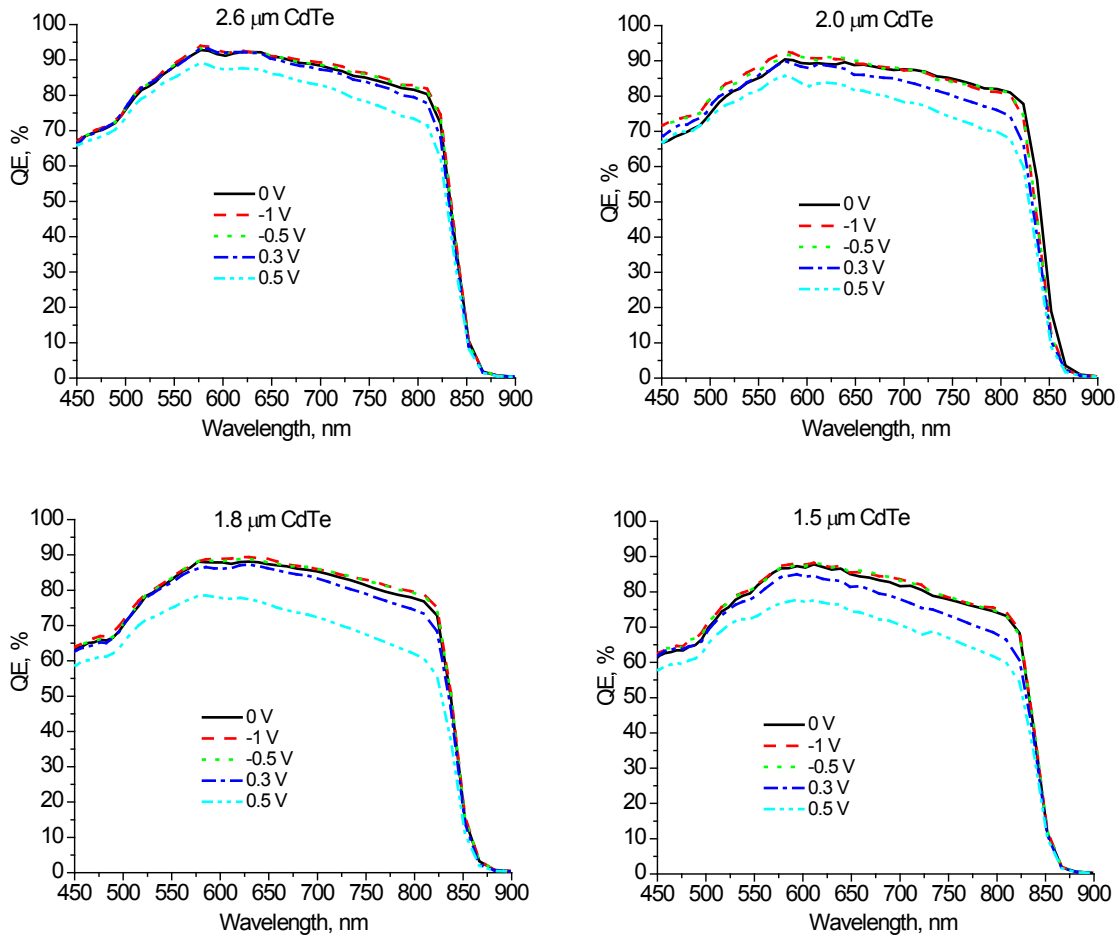


**Figure 7.16 Quantum efficiency at variable bias. Thicker cells.**

The results change significantly when the CdTe layer thickness decreases below one micron. The difference between zero-bias QE and reverse-bias QE becomes more apparent and shows no wavelength dependence below the CdS absorption edge. QE also shows an overall decrease that is not compensated even by application of a strong negative bias and therefore cannot be attributed solely to a weaker electric field at the junction. We believe that it indicates some unidentified recombination mechanisms within the space charge region that are not present in the thicker cells. Plausible explanations can range from imperfections at the CdS/CdTe interface that are not fully cured because of the shorter CdCl<sub>2</sub> treatment of the thinner cells, higher grain boundary surface to the volume ratio in the thinner cells due to smaller average grain size, or proximity of the CdTe/back contact junction with a high surface recombination velocity.

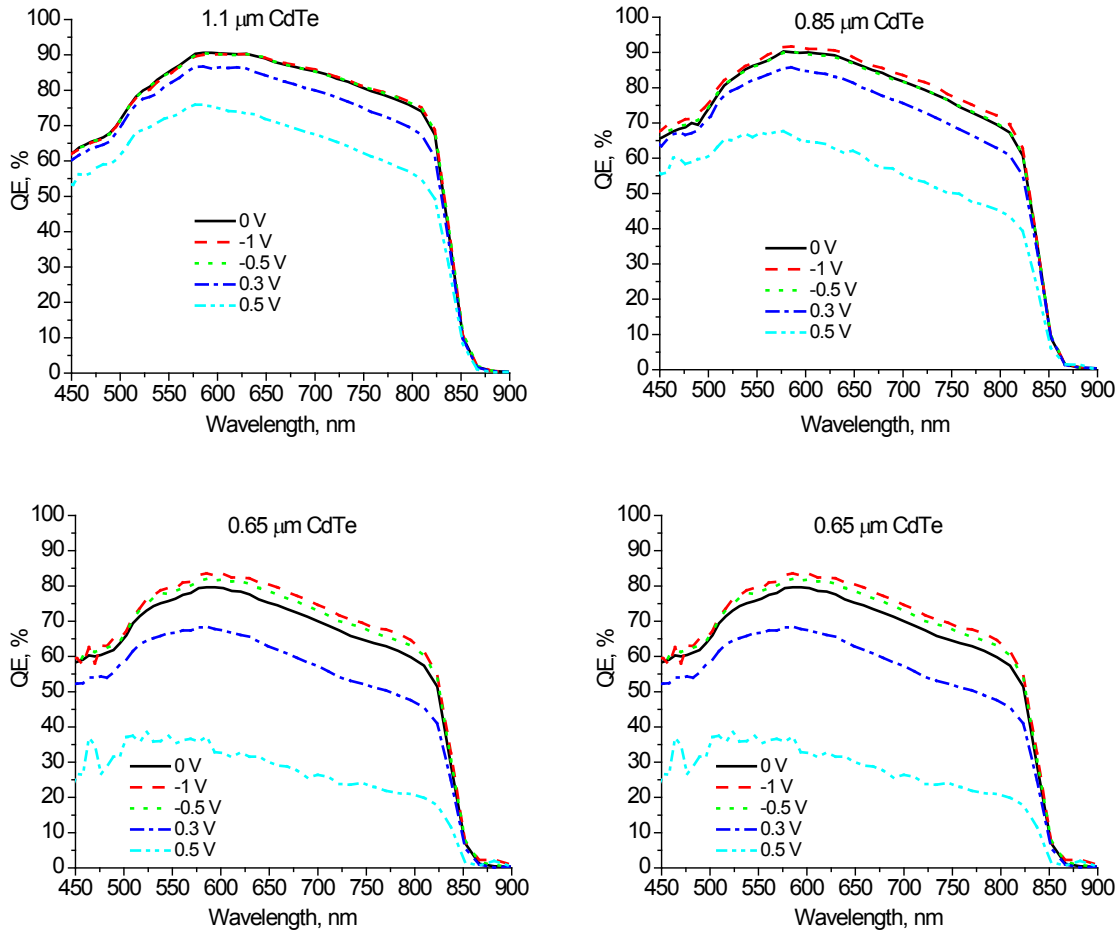


**Figure 7.17 Quantum efficiency at variable bias. Thinner cells.**

## 7.8 Conclusions

We investigated the dependence of the cell performance over a wide range of CdTe thicknesses (0.35 μm...2.6 μm). We find that that an average efficiency of greater than 12% can be achieved for cells as thin as 1 micron with the appropriate post-deposition treatment and optimized back contact scheme. Over CdTe thicknesses of one micron and above, we find the effect of the back contact scheme (as-deposited Cu thickness) to be more dramatic than variation in CdCl<sub>2</sub> treatment time. Insufficient Cu caused average  $V_{OC}$  reduction of as much as 50 mV in some cases, while the use of adequate amounts of Cu yielded  $V_{OC}$  greater than 800 mV consistently for all samples within this thickness range.

We also found that further reduction of CdTe thickness leads to a gradual decrease in performance although 10% efficiency can be obtained with 0.5 micron CdTe. We established some benchmarks for CdCl<sub>2</sub> treatment and back contact processing for these samples with CdTe thickness less than one micron that yield reasonably good results although more comprehensive studies need to be done to resolve the issue of  $V_{OC}$  and FF losses and collection probability less than unity from the space charge region in the thin cells.

## 8. Shunt Passivation - Electrochemical Polymerization Treatment of CdTe Solar Cells

### 8.1 Introduction

Conducting polymers are of significant interest given their possible application in numerous research areas including electronics, energy storage, and medicine [9]. Among such polymers, polyaniline has been studied extensively and is finding increasing uses in various fields of technology such as in gas sensors, electronics and anticorrosion coatings [10]. This polymer is readily prepared electrochemically from aqueous solution (anodic polymerization onto the electrode surface), is insoluble in water and has high chemical stability [11,12]. As shown in Fig. 8.1 below, the value of Y in each individual unit X may be Y = 1, the fully reduced form (leucoemeraldine base), Y = 0.5, the form that is half oxidized (emeraldine base, most stable form), and Y = 0, the fully oxidized form (pernigraniline base) [9].

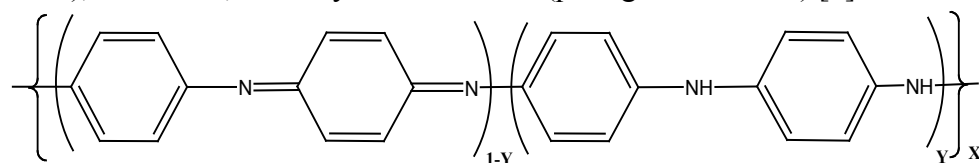


**Figure 8.1** The base (i.e., neutral) polyaniline, which is half reduced/oxidized, is thought to be of this general structure.

The electrochemical polymerization technique is an interfacial reaction, performed by applying a voltage across a conductive substrate and an inert electrode, both placed inside an electrolyte rich solution containing a selected monomer, which for this study was aniline. The aniline monomer reacted with the exposed surface of the conductive substrate (the transparent conducting oxide (TCO) coated glass) to form a poorly conducting polymer (polyaniline) on the surface. In this study we anticipated growing polyaniline in the pinhole areas that have the TCO layer or CdS layer of the CdTe solar cell exposed. The CdTe solar cell is built on a glass substrate which is coated with a TCO, then sputter deposited with CdS (n-type) and CdTe (p-type) semiconductors before finally depositing the metal back contact (Cu-Au). Occasionally, pinhole defects are created during the fabrication process. In such cases, our goal was to selectively coat any portions of the TCO and/or CdS layer that are exposed through the semiconductor layers, without affecting the surface of the CdTe layer. After the electrochemical polymerization treatment, an insulating material (polyaniline) is expected to fill the pinholes and prevent the formation of an electrical contact (shunt) between TCO /CdS and the Cu-Au back contact. We have succeeded in this goal and we were able to obtain promising results that indicates both the deposition of the polymer on the solar cell device and reduction of shunting of the CdTe solar cell.

### 8.2 Characterizing the New Insulating Thin Film (Conducting Polymer) – using X-ray Photoelectron Spectroscopy (XPS) and Electron Spray Ionization – Mass Spectroscopy (ESI-MS) Techniques

The monomer solution (standard): A freshly prepared solution containing 0.2 M Aniline, 0.1 M p-toluenesulfonic acid (p-TSA), 2.0 M sodium chloride in water was stirred for half an hour,



providing a solution with a pH ~6.2. Since aniline is photo-sensitive, the entire process was done inside a hood with the lights off. Aniline, and its solution, oxidizes on exposure to air (oxygen) and light, as seen by a change in color (from colorless to dark brown).

Electrochemical treatment technique (standard): A potentiostat (D.C. power supply), containing two wires terminating with an alligator clip, were used to apply a potential between a TEC-15 glass substrate and a platinum electrode used as an auxiliary electrode. TEC-15 is a 3 mm thick glass substrate coated with a transparent conductive oxide ( $\text{SnO}_2\text{:F}$ ). The  $\text{SnO}_2\text{:F}$  layer acts as the anode/positive electrode and the platinum electrode as the cathode/negative. The electrodes were placed in a beaker filled with one inch height of the monomer (aniline) solution. The TEC-15 glass substrate is submerged half way into the solution. A voltage of 2.0 Volt was applied for 20 minute to polymerize the aniline. After the polymer treatment the device was rinsed with de-ionized water and dried with a stream of compressed air. The new film coating has a thickness of  $2500 \pm 50 \text{ \AA}$ , measured using a DEKTAK depth profiler and  $1.305 \text{ k}\Omega/\square$  sheet resistance (poor conductor).

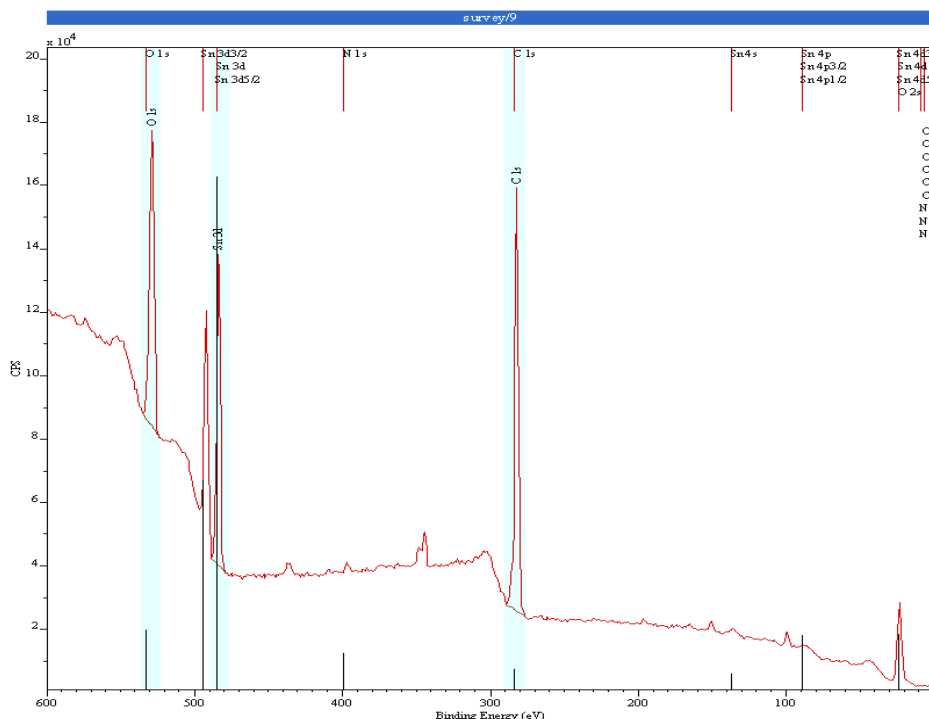


**Figure 8.2** XPS spectrum of a TEC-15 glass substrate used as a control - not coated with the conducting polymer.

The sample that is now half coated with the new insulating polymer thin film is cut into half. Both the coated and the uncoated side of the TEC-15 were examined by X-ray photoelectron spectroscopy (XPS) analysis with  $\text{Cu K}\alpha$  photons –  $h\nu = 8048\text{eV}$ . The kinetic energy (KE) distribution of the emitted photoelectrons is measured with an electron energy analyzer and the binding energy (BE) is obtained from

$$\text{BE} = h\nu - \text{KE}.$$

The samples were measured using a Kraos Axis Ultra XPS, at the University of Michigan – EMAL, with sample chamber base pressure of  $\sim 5.6 \times 10^{-9}$  mTorr. The survey scans of the uncoated/control and the coated thin film are shown in Figures 8.2 and 8.3 below:

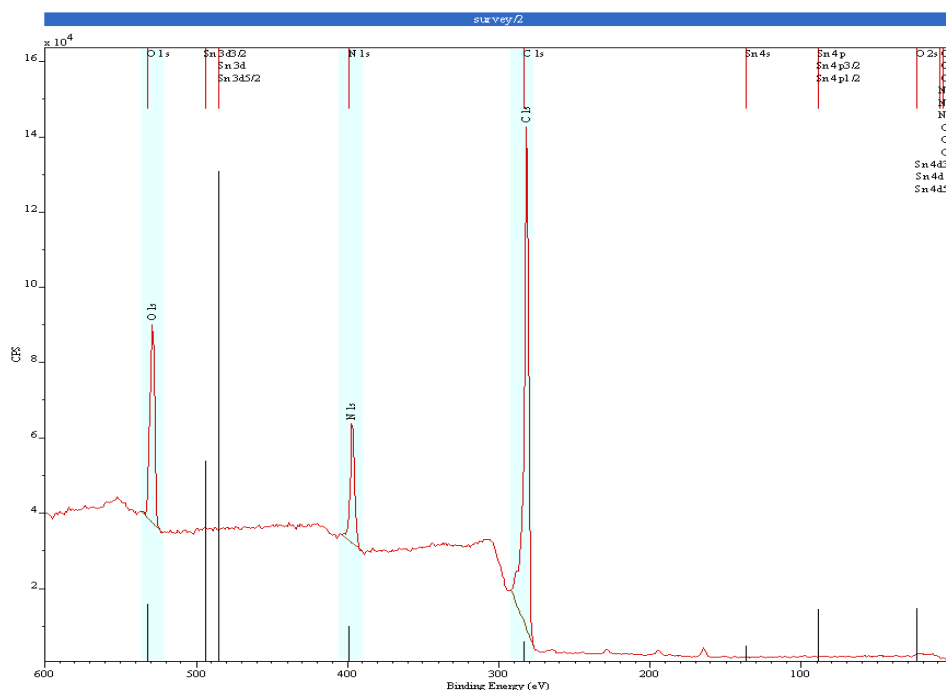


**Figure 8.3 XPS spectrum of a TEC-15 glass substrate coated with the conducting polymer.**

In these XPS spectra, we anticipated seeing the presence of oxygen and carbon in both cases, due to contamination/dust particles on the sample surface. However, the key elements to look for are ‘Sn’ and ‘N’. For the uncoated sample used as a control (with no polymer film coating), we anticipated seeing the presence of  $\text{SnO}_2$  (Sn and O elements). As shown in Fig. 8.1, we can clearly see ‘O’ and ‘Sn’ peaks, with binding energies of 532 eV and 487 eV respectively. On the other hand, for the sample with the new thin-film coating, Fig. 8.2, we do not see any ‘Sn’ peaks, but rather we see a new ‘N’ peak with a binding energy of 398 eV. This information provides two insights:

1. an indication that the sample surface is covered with a new material, and
2. that the new thin film might be a polymer – polyaniline.

Among all the chemicals used in this experiment, ‘N’ is present only in the aniline monomer (solution). At this point, we know that the aniline monomer is part of the new thin-film coating, but we cannot confirm that it is polyaniline. We used Electron Spray Ionization – Mass Spectroscopy (ESI-MS) to determine the molecular weight of the new thin film coating to answer this question. The ESI-MS instrument used for this experiment is located at The University of Toledo – Instrumentation Center.

A standard aniline solution was prepared and the standard electro-chemical polymerization treatment was applied to a TEC-15 glass substrate with a voltage of 2.0 V for 20 minutes. After the polymerization treatment, the device was rinsed with deionized water and dried with a stream of compressed air. The new film coating that is formed on the TEC-15 glass substrate is then rinsed from the substrate using ethanol and collected in a beaker. The rinsed solution was then diluted further with ethanol in a test tube before running the ESI-MS.

As shown in Fig. 8.4 (a and b) below: we can see the major peaks of polyaniline oligomers [9]; 183 m/z, 278 m/z, 365 m/z, 454 m/z, 545 m/z, 634 m/z, 725 m/z, 816 m/z, 907 m/z and 996 m/z. These results match the data reported by Haiteng Deng and Gary J. Van Berkel at Oak Ridge National Laboratory, on a similar experiment [9]. As indicated in both spectra our newly grown film is a mixture of aniline oligomers, ranging from a dimer to hendecamer (11-mer).

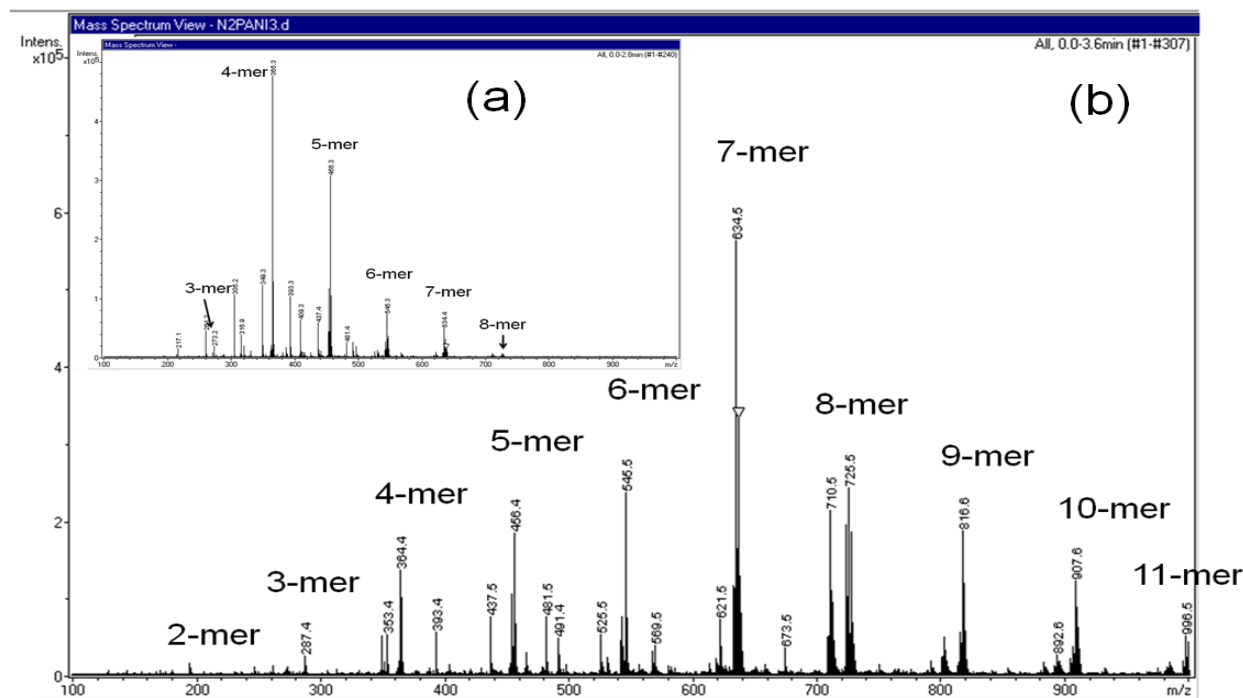


**Figure 8.4** ESI-MS spectra of the newly formed thin film after rinsing, showing a mixture of oligomers ( $n$ -mers). (a) ESI-MS spectra reading of the rinsed solution with the instrument - target mass sensitivity set to 250  $m/z$ . (b) ESI-MS spectra reading of the rinsed solution with the instrument – target mass sensitivity set to 750  $m/z$ .

In the spectra of Fig. 8.4 a and b, the ESI-MS mass target sensitivity was set to 250  $m/z$  and 750  $m/z$  respectively. For this reason, in Fig. 8.4a, the tetramer (4-mer) appears to have a higher concentration, than the other oligomers. Similarly, in Fig. 8.4b, the heptamer (7-mer) appears to have a higher concentration, than the other oligomers.

In conclusion, we have obtained convincing information from both XPS and ESI-MS characterization techniques, indicating the growth of a new film on the substrate and the formation/presence of polyaniline.

### 8.3 Effect of Electrochemical Treatment on Copper Diffusion

A CdTe solar cell sample was prepared on an HRT-coated TEC-15 glass substrate. Both the CdS and CdTe layers were sputtered in the AJA-system. After the deposition on the CdTe layer, a  $\sim 28$  minute, 385  $^{\circ}\text{C}$   $\text{CdCl}_2$  treatment was done. The samples had noticeable pinholes and were therefore ideal tests for the electrochemical polymerization treatment. Using the standard aniline solution, the standard electrochemical treatment was performed. Similar to the previous

experiment, as shown in Fig. 8.5 below, half of the sample was electrochemically treated and the other half was left untreated as a control.

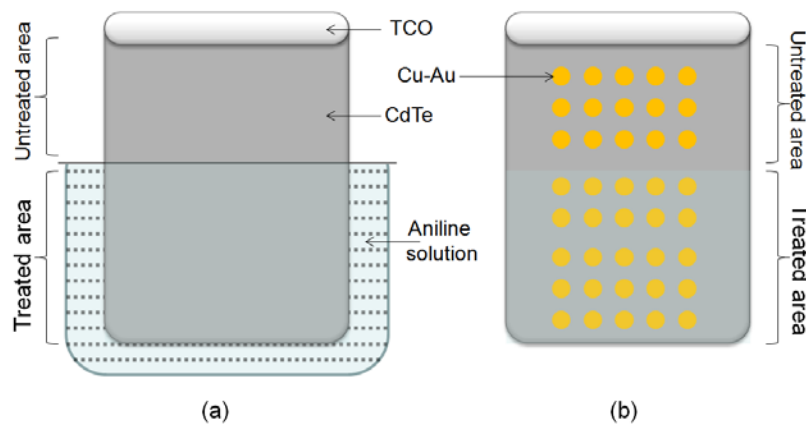


**Figure 8.5** Top surface view of the CdTe solar cell sample. (a) Sample placement inside the aniline solution - half of the sample immersed in the aniline solution. (b) Sample after Cu-Au deposition – 15 dot cells and 25 dot cells in the untreated and treated areas respectively.

After electro-polymerization the sample was metalized through a mask to form dot cells with Cu/Au, 35Å / 200 Å, respectively, by evaporation and then unintentionally diffused for 2 hours instead of the standard 45 minutes at 150 °C. I-V characteristics were measured using the Oriel solar simulator.

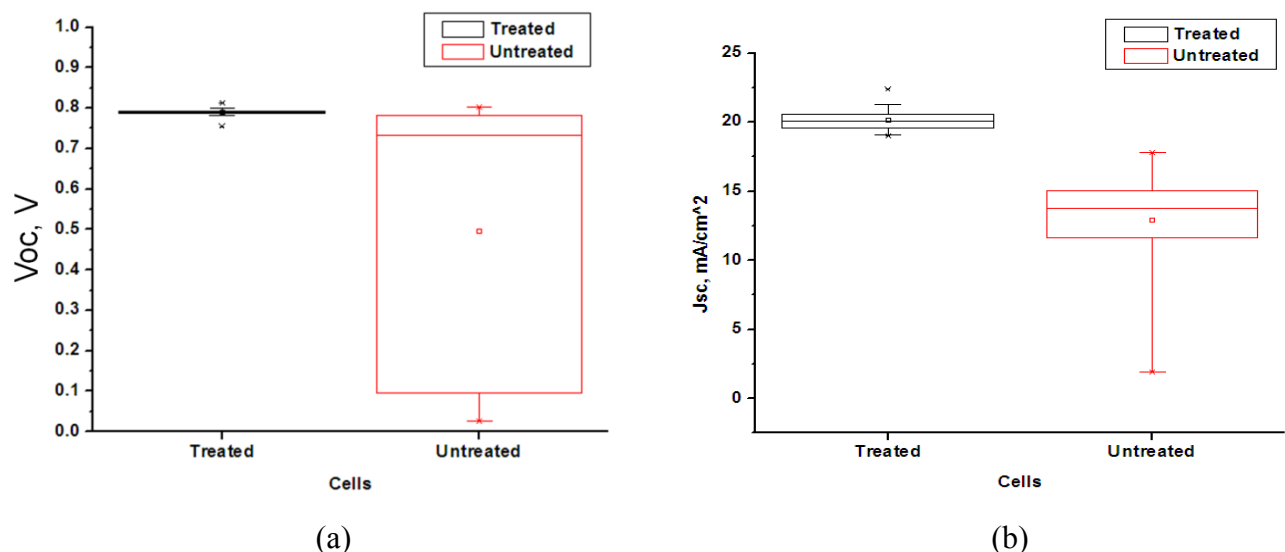


**Figure 8.6** A 2 hour copper diffusion of an electrochemically treated and untreated CdTe solar cell device. (a) Open-circuit voltage (b) Short-circuit current.

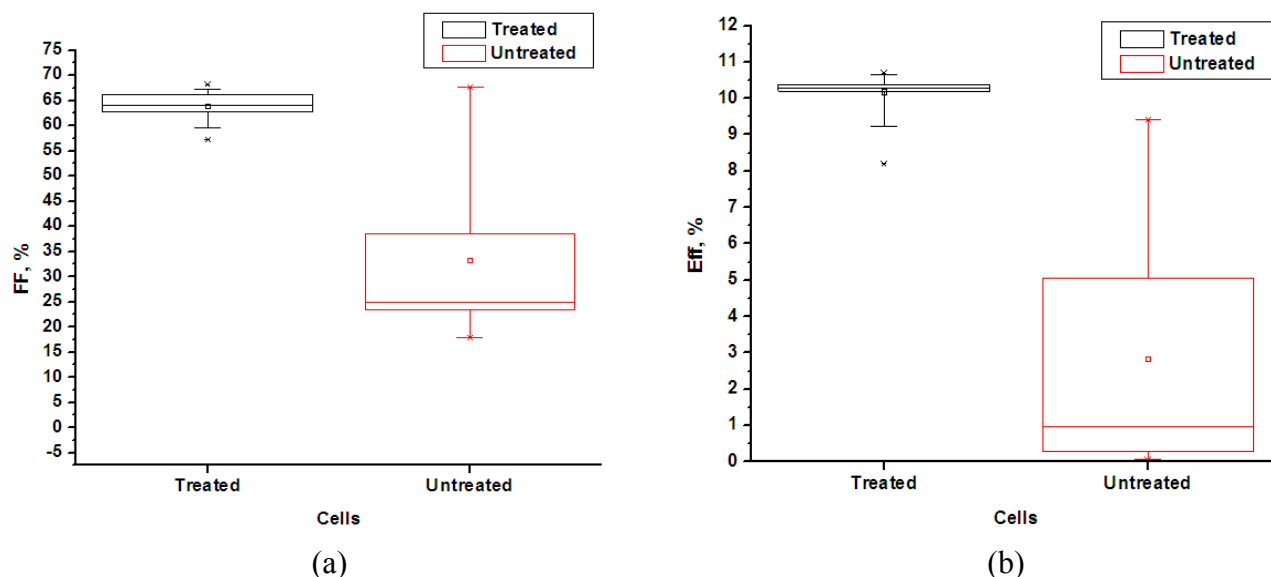


**Figure 8.7 A 2 hr copper diffusion of an electrochemically treated and untreated CdTe solar cell device. (a) Fill factor and (b) Efficiency measurements.**

After 2 hours of copper diffusion treatment, our expectation was to see very poor solar cell performance. However, as shown in Fig. 8.7b, the cells from the treated area have an average cell parameters of:  $V_{OC}=0.79$  V,  $J_{SC}=20.2$  mA/cm<sup>2</sup>, FF=64 % and efficiency =10.2 %. The cells from the untreated area have averages of:  $V_{OC}=0.50$  V,  $J_{SC}=12.9$  mA/cm<sup>2</sup>, FF=33.3 % and Eff=2.85 %. Additionally, the data scatter in all categories was very narrow for the treated as compared to the untreated area cells. This indicates that pinholes are filled with an insulating material (polyaniline) and good shunt passivation appears to have been obtained.

However, conclusive results will await further tests on devices with our standard 45 minutes of copper diffusion rather than 2 hours of copper diffusion and using devices with a variety of pinhole densities. However, there is some indication that the electro-polymerization is providing is creating an ultra thin layer of polyaniline (conductive) on the CdTe surface that acts not only as a shunt Passivation but also as a diffusion barrier for the copper metal. Based on this result, this experiment opens a new door to the electrochemical treatment and further experiments are in progress.

## 9. A Theory of Admittance Spectroscopy for Thin Film Photovoltaics

### 9.1 Introduction

Admittance spectroscopy has long been a routine characterization technique in semiconductor science and technology.[13] It provides information about the space charge distribution (capacitance-voltage, C-V) and the density of states distribution (capacitance-frequency, C-F) in crystalline, amorphous, and polycrystalline semiconductor materials and devices.[14] The standard understanding of admittance characterization is based on the model of a leaky flat plate capacitor. The admittance measurements conducted at different frequencies ( $\omega$ ), biases ( $V$ ), and temperatures ( $T$ ) are interpreted assuming a model where all the physical quantities (such as defect states and doping profiles) vary along one spatial coordinate perpendicular to the system electrodes. This assumption implies that the electrodes are equipotentials, so that there is no lateral current in the system. However, many practically important device structures, such as photovoltaics, have sufficiently resistive electrodes that are not equipotentials and exhibit significant currents in the lateral directions.

The purpose of this work is to introduce a theory of admittance characterization for a broad range of systems with resistive electrodes. The theory provides a practical method to effectively determine specific device parameters, such as shunt resistance, lateral resistance, non-uniformities, capacitance, and others. More specifically, we consider a distributed system exhibiting leaky photo-diode and capacitive properties, whose discrete equivalent circuit is shown in Fig. 9.1. The fundamental element of the system includes: 1) a photodiode characteristic of the semiconductor material; 2) a capacitance related to the material response to an ac voltage; and 3) a shunt resistance, all in parallel with each other. This model and the theoretical development make no reference to specific material combinations. Also, we consider both one-dimensional (1D) and two-dimensional (2D) systems.

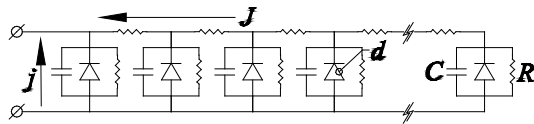


**Figure 9.1** Equivalent circuit of a device with a resistive electrode in the lateral direction and distributed diode, capacitance, and shunt resistance in the transverse direction.

A similar but simpler model, without distributed capacitance and shunt resistance, was analyzed earlier to describe dc operations of photovoltaics.[15] The previous work introduced a characteristic decay length,  $L_0$ , of a small electric perturbation in the lateral direction. It was shown that the decay length delineates the region in which current is collected (the active area) and, therefore, influences the  $I/V$  characteristics of the device. In the present work, the concept of decay length is extended to include systems with distributed shunt resistance and capacitance, resulting in two new characteristic lengths,  $L_R$  and  $L_C$ , that describe the decay of an ac perturbation in the system and determine the frequency-dependent admittance. Simultaneously, various regimes of applied dc voltage are considered. We show that an understanding of these decay lengths plays a vital role in effective device characterization.

## 9.2 Theory

Our methodology consists of a qualitative analysis to provide a general overview of the phenomena and to calculate estimates of the frequency-dependent admittance. Then, starting from first principles, we present a rigorous derivation of the exact results for various testing biases and device structures. Using these results, we provide a detailed description of integrity and uniformity diagnostic techniques for thin-film photovoltaic devices with examples of practical applications.

A complete description of the decay length approach requires that we clearly define all conceivable scenarios. First of all we note the division into the regimes of geometrically large ( $l \gg L$ ) and small ( $l \ll L$ ) cells, each of which can be either 1D or 2D systems. In addition, one has to discriminate between two types of electrode configurations, namely, substrate (*e.g.* CuIn(Ga)Se<sub>2</sub> or a-Si:H) and superstrate (*e.g.* CdTe) devices. Therefore, there are a total of eight conceivable nominally different scenarios, with the four 1D scenarios presented in Fig. 9.2. A small electric perturbation at the input of the circuit in Fig. 9.1 will decay in the lateral direction over the characteristic length,  $L$ , determined by the electrode resistance and current leakage through the transverse resistors, diodes, and capacitors. The decay length  $L$ , together with the linear dimension of the electrode  $l$ , determines the active region of the system as shown for the various scenarios in Fig. 9.2.

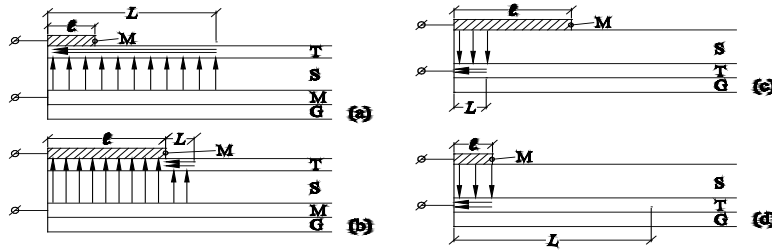


**Figure 9.2** Examples of four possible 1D device scenarios: (a) small, substrate; (b) large, substrate; (c) large, superstrate; and (d) small, superstrate. The device components are labeled as M, T, S, and G for metal, TCO, semiconductor, and glass, respectively.

In the framework of the qualitative analysis, the characteristic decay length is estimated as the minimum of the three partial lengths,  $L_R$ ,  $L_C$ , and  $L_d$  (decay length of an ac voltage due to diodes). Straightforward calculations show that  $L_R = \sqrt{R/\rho}$ ,  $L_C = \sqrt{1/(\omega c \rho)}$  and  $L_d$  depends on the applied dc bias and is related to the previously defined dc decay length,  $L_0$ . In these equations,  $\omega$  is the testing frequency,  $R$  is the specific shunt resistance,  $\rho$  is the sheet resistance of the resistive electrode, and  $c$  is the specific capacitance. By applying qualitative arguments it is shown that the measured capacitance splits into high and low frequency regimes. In the low frequency regime, the capacitance is constant and depends on device parameters, while in the high frequency regime the measured capacitance is frequency dependent with  $C \sim \sqrt{c/(\omega \rho)}$  for a large superstrate device.

In the rigorous derivation we provide a general formalism for calculating the frequency-dependent admittance for a broad range of devices and testing scenarios. We show that the rigorous results are similar to the qualitative results with the two frequency regimes of the measured capacitance and conductance defined by a characteristic frequency,  $\omega_0$ , given as  $\omega_0 = 1/(c\rho)(1/L_o^2 + 1/L_R^2)$ . Using our general formalism, we are able to provide exact results for

the eight different scenarios discussed above. We show that for the cases of small superstrate cells our results reduce to the typical analysis of admittance results applied in the current standard practice, while for other types of cells there are important differences that must be considered for proper device characterization.

### 9.3 Practical Implications

We believe that our work introduces a diagnostic technique applicable to practically any semiconductor junction. Here we discuss in more detail the case of thin-film photovoltaics to provide examples of device parameter evaluation. For definiteness, we focus on the substrate type of photovoltaics, particularly CuIn(Ga)Se<sub>2</sub> with the typical structure (glass / metal / CuIn(Ga)Se<sub>2</sub> / CdS / buffer) and the following parameters: buffer (TCO) layer sheet resistance of  $\rho \sim 10 \Omega/\square$ ; current density  $j_o \sim 0.03 \text{ A/cm}^2$  (for 1 sun light intensity); shunt resistance  $R \sim 10^4 \Omega\cdot\text{cm}^2$ ; and capacitance  $c \sim 1 \text{ nF/cm}^2$ . Corresponding to these parameters are the decay lengths  $L_o \sim 0.3 \text{ cm}$  and  $L_R \sim 30 \text{ cm}$ , and the characteristic frequency  $\omega_o \sim 10^9 \text{ rad/s}$ . Note, however, that the current  $j_o$  can be decreased and the length  $L_o$  increased by, respectively, four and two orders of magnitude by decreasing the light intensity from 1 sun to the typical ambient room light. In addition, we assume a testing frequency range of  $\omega \sim 1$  to  $10 \text{ rad/s}$ , corresponding to the capacitive decay length  $L_C \sim 10 - 10^4 \text{ cm}$ .

Consider as an example a small cell of radius  $a$  deposited as a current collection terminal on the buffer layer; the other terminal is connected to the metal electrode buried under the semiconductor. The inequalities and correspond to the low frequency regime of a 2D small cell with the conductance and capacitance given by,

$$G = \frac{2\pi}{\rho} \frac{1}{\ln(L/a)} \quad \text{and} \quad C = \frac{\pi}{\rho\omega} \frac{1}{[\ln(L/a)]^2} \arctan\left[\frac{L_o^2 L_R^2}{L_C^2 (L_o^2 + L_R^2)}\right]$$

Measuring  $G$  and  $C$  under these conditions will give information about  $\rho$  and  $j_o$ . The capacitance as a function of frequency is presented in Fig. 9.3.

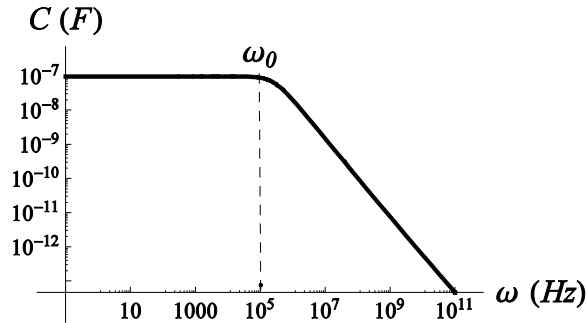


**Figure 9.3** Prediction of capacitance as a function of frequency for a small 2D substrate cell under the conditions discussed in the running text. The measured capacitance is constant in the region  $\omega \ll \omega_o$  and goes as  $1/\omega$  in the region  $\omega \gg \omega_o$ , where  $\omega_o \sim 10^5 \text{ rad/s}$ .

Also, in the low frequency regime the measured frequency-dependent capacitance will have to be attributed to the intrinsic  $c(\omega)$ , if any, which was considered constant our formulation, thus giving the standard admittance spectroscopy information about the material related to space charge density and defect energy spectra. We note that the typical frequency dependence for  $c(\omega)$  is logarithmically weak and can hardly be mistaken for the above predicted  $C \propto 1/\omega$  in the high frequency region.

Under the same conditions, decreasing the light intensity will eventually put the system into the regime where  $L_R \ll L_o$  and  $L_R$  becomes the predominant (smaller) decay length. This crossover, after which  $C$  and  $G$  become independent of light intensity, will determine the shunt



resistance  $R$ . One conceivable outcome of such experimenting is that the crossover will take place at a light intensity which is above the expected value *due to the presence of a shunt* at distance  $L_O$  from the cell. Therefore, our proposed capacitance diagnostics have the potential of detecting shunts and their distribution in the system. Another effect of low light intensity is that the characteristic frequency will change from  $\omega_o \sim 10^9$  to  $10^5$  rad/s, well into the testing frequency range (as shown in Fig. 9.3), which makes it possible to observe the crossover between the high and low frequency regimes, thus determining  $\omega_o$  and related parameters.

Our work also provides additional examples related to the effects of different test biases as well as methods to measure other system parameters, such as  $V_{oc}$  and ideality factor. We also detail how these diagnostic techniques can be applied to thin-film photovoltaics before the device is finished so that information related to system leakage can be determined prior to metallization.

## 9.4 Conclusions

In conclusion, we have developed a theory of ac response by systems of distributed diodes in parallel with resistors and capacitors connected through resistive electrodes that can represent many practical devices including photovoltaics and Schottky junctions. In particular, we have shown that:

1. There exist three lateral decay lengths related to the system diodes, shunt resistors, and capacitances respectively that determine the effective frequency-dependent lateral decay length  $L$  and describe the physics of ac response in such distributed systems;
2. The response is frequency-independent below a certain characteristic frequency, above which it strongly depends on testing frequency;
3. The 1D and 2D systems behave similarly in the large device regime,  $l \gg L$ , where  $l$  is the device lateral dimension, while in the small device regime,  $l \ll L$ , 2D systems exhibit certain unique behavior;
4. Both the capacitance and conductance are described by closed form analytical expressions as functions of frequency and dc bias and are parametrically dependent on system material characteristics;
5. Our theoretical results establish a basis for a type of admittance characterization applicable to a wide variety of semiconductor structures including photovoltaics and Schottky junctions.

## 10. References (from Sections 1 through 9)

---

- [1] B. Johs, C. Herzinger, J. Dinan, A. Cornfeld, J. Benson, *Thin Solid Films* 313, 137 (1998).
- [2] J. Chen, J. Li, D. Sainju, K. D. Wells, N. J. Podraza, and R. W. Collins, *Proc. 4th World Conference on Photovoltaic Energy Conversion*, (IEEE, Piscataway NJ, 2006), p. 475.
- [3] D. Dunstan, B. Gil, C. Priester, K. Homewood, *Semicond. Sci. Technol.* **4**, 241 (1989).
- [4] X. Liu, A. Compaan and J. Terry, "X-ray absorption fine structure study of aging behavior of oxidized copper in CdTe films", *31<sup>th</sup> IEEE Photovoltaic Spec. Conf.*, pp 267-270 (0-7803-8707-4/05/.2005 IEEE.).
- [5] Visoly-Fisher, I., K. D. Dobson, J. Nair, E. Bezael, G. Hodes and D. Cahen, *Adv. Funct. Mater.*, **13**(4), 289 - 299 (2003).
- [6] X. Liu, A. Compaan and J. Terry, "Cu K-edge X-ray fine structure changes in CdTe with CdCl<sub>2</sub> processing", *Thin Solid Films*, **480-481** (2005), pp. 95-98.
- [7] B. E. McCandless, "Diffusion in CdS/CdTe thin film couples," *Proc. 16th European PVSEC*, 2000, 349.
- [8] D. Shaw and E. Watson. The diffusion of chlorine in CdTe. *J. Phys. C: Solid State Phys.*: **17** (1984) 4945-4950.
- [9] Deng, Haiteng, Van Berkel, Gary J.; *Anal. Chem.* **1999**, 71, 4284-4293.
- [10] Liao, Chuanping, Gu, Mingyuan, *Thin Solid Films*, **2002**, 408, 37-42.
- [11] E.T. Kang, K.G. Neoh, K.L. Tan, *Prog. Polym. Sci.* **1998**, 23, 277.
- [12] G. Min, *Synth. Met.* **1999**, 102, 1163.
- [13] K. Schroder, *Semiconductor Material and Device Characterization*, John Wiley, 1998.
- [14] P. Blood and J. W. Orton, *The electrical characterization of semiconductors: majority carriers and electron states*, Academic Press, NY 1992.
- [15] V. G. Karpov, G. Rich, A. V. Subashiev, G. Dorer, *J. Appl. Phys.* **89**, 4975 (2001).

## 11. Publications

### 11.1 Refereed Papers Published or in Press

1. "Piezo-effect and physics of CdS based thin-film photovoltaics", Diana Shvydka, J. Drayton, A. D. Compaan, and V. G. Karpov, *Appl. Phys. Lett.* 87, pp. 123505-1-3 (2005).
2. "Physical model of CdS based thin-film photovoltaic junctions", M. L. C. Cooray and V. G. Karpov, *Appl. Phys. Lett.*, 88 , p. 093508 (2005).
3. "Cu K-edge EXAFS Studies Of CdCl<sub>2</sub> Effect On CdTe Solar Cell", Xiangxin Liu, A. D. Compaan, and Jeff Terry, *MRS Symp. Proc.* 865, edited by W. Shafarman, T. Gessert, S. Niki, S. Siebentritt, F4.2 (2005).
4. "Photoluminescence from Ion Implanted CdTe Crystals", Xiangxin Liu and Alvin D. Compaan, *MRS Symp. Proc.* 865, edited by W. Shafarman, T. Gessert, S. Niki, S. Siebentritt, F5.25 (2005).
5. "Photoluminescence and Extended X-ray Absorption Fine Structure Studies on CdTe Material", Xiangxin Liu, Ph.D. Thesis: The University of Toledo, 2006 (unpublished, available at OhioLINK- Electronic Theses and Dissertations Center, <http://www.ohiolink.edu/etd/>).
6. "Spatial and Temporal Variations in Electronic Transport Through a CdTe-Based Schottky Barrier", Diana Shvydka, V. Parikh, V.G. Karpov and A.D. Compaan, *MRS Symp. Proc.* 865, edited by W. Shafarman, T. Gessert, S. Niki, S. Siebentritt, p. F12.2, (2005).
7. "Physics of CdTe Photovoltaics: From Front to Back", V.G. Karpov, Diana Shvydka, and Yann Roussillon, *MRS Symposium Proceedings* 865, edited by W. Shafarman, T. Gessert, S. Niki, S. Siebentritt, p. F10.1, San Francisco, March 28-April 1 2005.
8. "Lateral Nonuniformity and Mesoscale Effects in Giant Area Electronics, V. G. Karpov, Diana Shvydka, and Yann Roussillon", *MRS Symposium Proceedings* 870E, edited by M. S. Shur, P. Wilson, M. Stutzmann, p. H2.2, San Francisco, March 28-April 1 2005.
9. "Power generation in random diode arrays", Diana Shvydka and V. G. Karpov, *Phys. Rev. B* 71, pp. 115314-1-5 (2005).
10. "Real Time Analysis of Magnetron-Sputtered Thin-Film CdTe by Multichannel Spectroscopic Ellipsometry", Jian Li, Jie Chen, J. A. Zapien, N. J. Podraza, Chi Chen, J. Drayton, A. Vasko, A. Gupta, S. L. Wang, R. W. Collins, and A. D. Compaan, *Mater. Res. Soc. Symp. Proc.* **865**, 9-14 (2005).
11. "Propagating Electric Impulses in Thin Film PV", T. K. Wilson, Diana Shvydka and V. G. Karpov, *Proceedings of IEEE 4th World Conference on Photovoltaic Energy Conversion 2006* (IEEE, Piscataway NJ ), p. 471-474.
12. "Phenomenological model of CdS based thin film photovoltaics", M. L. C. Cooray and V. G. Karpov, *Proceedings of IEEE 4th World Conference on Photovoltaic Energy Conversion 2006* (IEEE, Piscataway NJ), p. 542 - 545.
13. "Piezo-photovoltaic coupling in thin-film CdS/CdTe solar cells", Jennifer Drayton, M. Mitra, and Diana Shvydka, *Proceedings of IEEE 4th World Conference on Photovoltaic Energy Conversion 2006* (IEEE, Piscataway NJ), p. 491 – 494.
14. "Pressure dependence of photovoltaic parameters in thin film Cu(In,Ga)Se<sub>2</sub> solar cells", Diana Shvydka, J. Drayton<sup>1</sup>, M. Mitra, S.X. Marsillac, F. Jacob, , *Proceedings of IEEE*

- 4th World Conference on Photovoltaic Energy Conversion 2006* (IEEE, Piscataway NJ), p. 465 – 467.
15. R.W. Collins, C. Chen, M.W. Horn, S. Pursel, and C. Ross, "The ultimate in real-time ellipsometry: multichannel Mueller matrix spectroscopy", *Applied Surface Science* **253**, 38-46 (2006).
  16. J. Li, J. Chen, N.J. Podraza, and R.W. Collins, "Real time spectroscopic ellipsometry of sputtered CdTe: effect of growth temperature on structural and optical properties", *Conference Record of the 2006 IEEE 4th World Conference on Photovoltaic Energy Conversion 2006*, (IEEE, Piscataway NJ) p. 392-395.
  17. J. Chen, J. Li, D. Sainju, K.D. Wells, N.J. Podraza, and R.W. Collins, "Multilayer analysis of the CdTe solar cell structure by spectroscopic ellipsometry", *Conference Record of the 2006 IEEE 4th World Conference on Photovoltaic Energy Conversion 2006*, (IEEE, Piscataway NJ, 2006) p. 475-478.
  18. R.W. Collins, A.D. Compaan, S. Marsillac, A. Parikh, J. Chen, and J. Li, "Optical analysis of II-VI alloys and structures for tandem PV", *FY07 DOE Review* (presented April 17-19, 2007).
  19. R. W. Collins, A.D. Compaan, J. Li, and J. Chen, "RTSE studies of the fabrication of high efficiency CdTe PV", *FY07 DOE Review* (presented April 17-19, 2007).
  20. J. Li, J.A. Stoke, N.J. Podraza, D. Sainju, A. Parikh, X. Cao, H. Khatri, N. Barreau, S. Marsillac, X. Deng, and R.W. Collins, "Analysis and optimization of thin film photovoltaic materials and device fabrication by real time spectroscopic ellipsometry", *Photovoltaic Cell and Module Technologies*, edited by B. von Roedern and A.E. Delahoy, (SPIE, Bellingham, 2007) vol. 6651, Art. No. 6651-07, p. 1-14.
  21. Victor Plotnikov and Alvin Compaan, "CdS/CdTe Solar Cells Made by High-rate Magnetron Sputtering," *Mater. Res. Soc. Symp. Proc.* 1012, Y12.28 (2007).
  22. L. Weinhardt, S. Liu, J. Zhou, M. Baer, T. Hofmann, O. Fuchs, A. Compaan, X. Wu, and C. Heske, "X-ray and Electron Spectroscopy Investigation of Interfaces and Surfaces in CdTe Thin Film Solar Cells," *Mater. Res. Soc. Symp. Proc.* 1012, Y7.6 (2007).
  23. V. Parikh, A. Vasko, A.D. Compaan, and S.X. Marsillac, "Transparent Back Contacts in CdTe/CdS: Evaluation for Tandem Cells," *Mater. Res. Soc. Symp. Proc.* 1012, Y2.8 (2007).
  24. V.G. Karpov, M.L.C. Cooray, and Diana Shvydka, "Physics of ultrathin photovoltaics," *Appl. Phys. Lett.* 89, 163518 (2006).
  25. T. K. Wilson, Diana Shvydka and V. G. Karpov, "Propagating Electric Impulses in Thin Film PV", *Proc. 32nd IEEE Photovoltaic Specialists Conference-2006*, Waikoloa, Hawaii May 7-12, 2006 (IEEE Piscataway, N.J.) p. 471.
  26. M. L. C. Cooray and V. G. Karpov, "Phenomenological model of CdS based thin film photovoltaics", *Proc. 32nd IEEE Photovoltaic Specialists Conference-2006*, Waikoloa, Hawaii May 7-12, 2006 (IEEE Piscataway, N.J.) p. 542.
  27. Jennifer Drayton, M. Mitra, and Diana Shvydka "Piezo-photovoltaic coupling in thin-film CdS/CdTe solar cells", *Proc. 32nd IEEE Photovoltaic Specialists Conference-2006*, Waikoloa, Hawaii May 7-12, 2006 (IEEE Piscataway, N.J.), p. 491.
  28. Diana Shvydka, J. Drayton, M. Mitra, S.X. Marsillac, F. Jacob, "Pressure dependence of photovoltaic parameters in thin film Cu(In,Ga)Se<sub>2</sub> solar cells", *Proc. 32nd IEEE Photovoltaic Specialists Conference-2006*, Waikoloa, Hawaii May 7-12, 2006 (IEEE Piscataway, N.J.), p.465.

29. M.L.C. Cooray and B.G. Karpov, "Long-range random potential in thin-film structures," *Phys. Rev. B.* 75, 1 (2007).
30. Xiangxin Liu, A. D. Compaan, Kai Sun and Jeff Terry, "EXAFS and High Resolution TEM Studies of Cu at the Back Contact in Sputtered CdS/CdTe Solar Cells", 33<sup>rd</sup> IEEE Photovoltaic Specialists Conference, 2008.
31. Victor Plotnikov, Xiangxin Liu and Alvin D. Compaan, "Studies of Cu location near the back contact of CdS/CdTe solar cells", 33<sup>rd</sup> IEEE Photovoltaic Specialists Conference, 2008.
32. J. Li, N. J. Podraza, R. W. Collins, "Real time spectroscopic ellipsometry of sputtered CdTe, CdS, and CdTe<sub>1-x</sub>S<sub>x</sub> thin films for photovoltaic applications", *Physica Status Solidi (a)*, **205**(4), 901-904 (2008).
33. P. Petrik, N. Q. Khanh, J. Li, J. Chen, R. W. Collins, M. Fried, G. Z. Radnóczy, T. Lohner, J. Gyulai, "Ion implantation induced disorder in single-crystal and sputter-deposited polycrystalline CdTe characterized by ellipsometry and backscattering spectrometry", *Physica Status Solidi (c)*, **5**(5), 1358-1361 (2008).
34. J. Li, J. Chen, R. W. Collins, "Analysis of the dielectric functions of CdS and CdTe for grain size, stress, and temperature: potentialities for on-line monitoring", *Conference Record of the 33rd IEEE Photovoltaic Specialists Conference*, (IEEE, Piscataway NJ, 2008).
35. *Amorphous and Nanocrystalline Semiconductors: Science and Technology*, edited by P. C. Taylor, H.M. Branz, R.W. Collins, and E.A. Schiff (Elsevier, Amsterdam, 2008) 850 page book.

## 11.2 Poster or Oral Presentations

1. "Understanding the Physics of CdS-based PV: Band Diagram, Interfaces, and Nonuniformities", V. G. Karpov, D. Shvydka, J. Drayton, M. L. C. Cooray, and A. D. Compaan, DOE Solar Energy Technologies Program Review Meeting, November 7-10, Denver, Colorado, DOE/GO-1020006-2245, March (2006).
2. "Piezo-effect in CdS-based solar cells", Diana Shvydka, Jennifer Drayton, Mukut Mitra, Proceedings of the 19th National CdTe R&D Meeting, Editors: H. S. Ullal. P. V. Meyers, and C. Ferekides, Golden, Colorado, March 9-10 (2006).
3. "Indicative facts and device model", V. G. Karpov, D. Shvydka, J. Drayton, L. Cooray, and A. D. Compaan, Proceedings of the 19th National CdTe R&D Meeting, Editors: H. S. Ullal. P. V. Meyers, and C. Ferekides, Golden, Colorado, March 9-10 (2006).
4. "Back contact and nonuniformity", V. G. Karpov, D. Shvydka, J. Drayton, Y. Roussillon, and A. D. Compaan, Proceedings of the 19th National CdTe R&D Meeting, Editors: H. S. Ullal. P. V. Meyers, and C. Ferekides, Golden, Colorado, March 9-10 (2006).
5. "Piezo-effect in CdS/CdTe solar cells", Diana Shvydka, J. Drayton, V. G. Karpov and A.D. Compaan, National CdTe R&D Team Meeting; Golden, CO; May 5-6, 2005.
6. J. Li, A. Parikh, J. Chen, D. Sainju, L.R. Dahal, J.A. Stoke, N.J. Podraza, and R.W. Collins, "Accurate determination of dielectric functions of thin films and interfaces in photovoltaic devices: critical issues in optical modeling", 2008 Materials Research Society spring meeting.
7. J. Li, J. Chen, R. W. Collins, "Analysis of the dielectric functions of CdS and CdTe for grain size, stress, and temperature: potentialities for on-line monitoring", the 33rd IEEE Photovoltaic Specialists Conference (2008).

### 11.3 Publications and Presentations at DOE Program Reviews

1. Alvin D. Compaan, Robert W. Collins, Victor Karpov, Dean Giolando “Fabrication and Physics of CdTe Devices by Sputtering,” DOE Solar Energy Technologies Program Review/Peer Review Meeting, Denver, Apr 17-19, 2007.
2. R. W. Collins, A.D. Compaan, Jian Li, and Jie Chen, “RTSE Studies of the Fabrication of High Efficiency CdTe PV,” DOE Solar Energy Technologies Program Review/Peer Review Meeting, Denver, Apr 17-19, 2007. (Manuscript available on-line at: [http://www1.eere.energy.gov/solar/review\\_meeting/pdfs/p\\_15\\_collins\\_univ\\_toledo.pdf](http://www1.eere.energy.gov/solar/review_meeting/pdfs/p_15_collins_univ_toledo.pdf))
3. A.D. Compaan, oral invited review presentation at the Solar Program Review, “Fabrication and Physics of CdTe Devices by Sputtering” Denver, CO, April 18, 2007. (Presentation available on-line at: [http://www1.eere.energy.gov/solar/review\\_meeting/pdfs/tf\\_4\\_compaan\\_univ\\_toledo.pdf](http://www1.eere.energy.gov/solar/review_meeting/pdfs/tf_4_compaan_univ_toledo.pdf))

## **12. Project Personnel**

### **12.1 Postdoctoral Associates / Research Assistant Professors**

1. Xiangxin Liu (Ph.D., University of Toledo, 5/2006)(5/06–)
2. Diana Shvydka (Ph.D. University of Toledo, 5/2002)(3/1/05 - 10/31/2006)

### **12.2 Graduate Students (with Principal Advisor)**

1. Victor Plotnikov (Compaan)
2. Naba Raj Paudel (Compaan)
3. Jian Li (Collins)
4. Anuja Parikh (Collins)
5. Jie Chen (Collins)
6. Lilani Cooray (Karpov)
7. Misle Tessema (Giolando)

### **12.3 Undergraduate Students**

*NSF Research Experience for Undergraduates (REU)*, Summer 2006, 2007, 2008;  
(Supported by NSF with some matching from this contract.)

1. Nathan Reaver (advisor, Compaan)
2. Ryan Zeller (advisor, Compaan)
3. Craig McClellan (advisor, Compaan)
4. Casey Bennett (advisor, Compaan)
5. Mary Lin (advisor, Compaan)
6. Jason Owens (advisor, Compaan)
7. Sheriff Ceesay (advisor, Compaan)

### **12.4 Technical Assistants**

Terry Kahle (3/03–)

**REPORT DOCUMENTATION PAGE**Form Approved  
OMB No. 0704-0188

The public reporting burden for this collection of information is estimated to average 1 hour per response, including the time for reviewing instructions, searching existing data sources, gathering and maintaining the data needed, and completing and reviewing the collection of information. Send comments regarding this burden estimate or any other aspect of this collection of information, including suggestions for reducing the burden, to Department of Defense, Executive Services and Communications Directorate (0704-0188). Respondents should be aware that notwithstanding any other provision of law, no person shall be subject to any penalty for failing to comply with a collection of information if it does not display a currently valid OMB control number.

**PLEASE DO NOT RETURN YOUR FORM TO THE ABOVE ORGANIZATION.**

<b>1. REPORT DATE (DD-MM-YYYY)</b> April 2009		<b>2. REPORT TYPE</b> Subcontract Report		<b>3. DATES COVERED (From - To)</b> 3/1/2005 - 11/30/2008	
<b>4. TITLE AND SUBTITLE</b> Fabrication and Physics of CdTe Devices by Sputtering: Final Report, 1 March 2005 - 30 November 2008				<b>5a. CONTRACT NUMBER</b> DE-AC36-08-GO28308	
				<b>5b. GRANT NUMBER</b>	
				<b>5c. PROGRAM ELEMENT NUMBER</b>	
<b>6. AUTHOR(S)</b> A. Compaan, R. Collins, V. Karpov, and D. Giolando				<b>5d. PROJECT NUMBER</b> NREL/SR-520-45398	
				<b>5e. TASK NUMBER</b> PVB91210	
				<b>5f. WORK UNIT NUMBER</b>	
<b>7. PERFORMING ORGANIZATION NAME(S) AND ADDRESS(ES)</b> University of Toledo Dept. of Physics and Astronomy Toledo, Ohio 43808				<b>8. PERFORMING ORGANIZATION REPORT NUMBER</b> ZXL-5-44205-01	
<b>9. SPONSORING/MONITORING AGENCY NAME(S) AND ADDRESS(ES)</b> National Renewable Energy Laboratory 1617 Cole Blvd. Golden, CO 80401-3393				<b>10. SPONSOR/MONITOR'S ACRONYM(S)</b> NREL	
				<b>11. SPONSORING/MONITORING AGENCY REPORT NUMBER</b> NREL/SR-520-45398	
<b>12. DISTRIBUTION AVAILABILITY STATEMENT</b> National Technical Information Service U.S. Department of Commerce 5285 Port Royal Road Springfield, VA 22161					
<b>13. SUPPLEMENTARY NOTES</b> NREL Technical Monitor: Bolko von Roedern					
<b>14. ABSTRACT (Maximum 200 Words)</b> The three overall emphases of this subcontract were the following: 1) improving our understanding of key aspects of CdS/CdTe solar cell device physics, 2) improving our understanding of magnetron sputtering and increasing the sputter deposition rate while maintaining high device quality, and 3) reducing the thickness of CdTe layers in the CdS/CdTe cell below 0.5 µm while maintaining voltage and fill factor.					
<b>15. SUBJECT TERMS</b> PV; device physics; solar cells; magnetron sputtering; spectroscopic ellipsometry; CdTe; CdS; deposition rate; device quality; admittance spectroscopy;					
<b>16. SECURITY CLASSIFICATION OF:</b>			<b>17. LIMITATION OF ABSTRACT</b> UL	<b>18. NUMBER OF PAGES</b>	<b>19a. NAME OF RESPONSIBLE PERSON</b>
<b>a. REPORT</b> Unclassified	<b>b. ABSTRACT</b> Unclassified	<b>c. THIS PAGE</b> Unclassified			<b>19b. TELEPHONE NUMBER (Include area code)</b>

Standard Form 298 (Rev. 8/98)  
Prescribed by ANSI Std. Z39.18